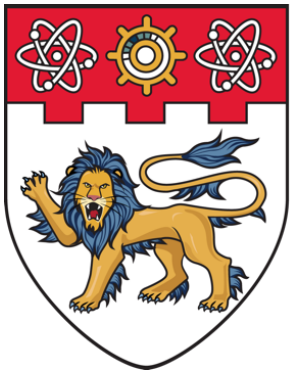

NANYANG TECHNOLOGICAL UNIVERSITY
SINGAPORE

SURFACE-ENHANCED RAMAN SCATTERING (SERS) SPECTROSCOPY IN SMALL MOLECULE DETECTION AND APPLICATION

KAO YA-CHUAN

SCHOOL OF PHYSICAL AND MATHEMATICAL SCIENCES

2021

SURFACE-ENHANCED RAMAN SCATTERING (SERS) SPECTROSCOPY IN SMALL MOLECULE DETECTION AND APPLICATION

KAO YA-CHUAN

SCHOOL OF PHYSICAL AND MATHEMATICAL SCIENCES

A thesis submitted to the Nanyang Technological University in partial fulfilment of the requirement for the degree of Doctor of Philosophy

2021

Statement of Originality

I hereby certify that the work embodied in this thesis is the result of original research done by me except where otherwise stated in this thesis. The thesis work has not been submitted for a degree or professional qualification to any other university or institution. I declare that this thesis is written by myself and is free of plagiarism and of sufficient grammatical clarity to be examined. I confirm that the investigations were conducted in accord with the ethics policies and integrity standards of Nanyang Technological University and that the research data are presented honestly and without prejudice.

18/03/2022

. . . . . .
Date

. . . . . .
Kao Ya-Chuan

Supervisor Declaration Statement

I have reviewed the content and presentation style of this thesis and declare it of sufficient grammatical clarity to be examined. To the best of my knowledge, the thesis is free of plagiarism and the research and writing are those of the candidate's except as acknowledged in the Author Attribution Statement. I confirm that the investigations were conducted in accord with the ethics policies and integrity standards of Nanyang Technological University and that the research data are presented honestly and without prejudice.

18/03/2022

. . . . . .
Date

. . . . . .
Ling Xing Yi

Authorship Attribution Statement

Please select one of the following; *delete as appropriate:

*(B) This thesis contains material from [x number] paper(s) published in the following peer-reviewed journal(s) / from papers accepted at conferences in which I am listed as an author.

Chapter 2 is published as Yih Hong Lee, Wenxiong Shi, Yijie Yang, Ya-Chuan Kao, Hiang Kwee Lee, Rongrong Chu, Yee Ling Pang, Chee Leng Lay, Shuzhou Li, Xing Yi Ling. Modulating Orientational Order to Organize Polyhedral Nanoparticles into Plastic Crystals and Uniform Metacrystals. *Angew. Chem. Int. Ed.* **59**, 21183-21189 (2020) DOI: 10.1002/anie.202009941.

The contributions of the co-authors are as follows:

- A/Prof Ling Xing Yi and Prof Li Shuzhou came up the project direction.
- A/Prof Ling Xing Yi, Dr Lee Hiang Kwee and Dr Lee Yih Hong prepared the manuscript drafts.
- A/Prof Ling Xing Yi, Prof Li Shuzhou Dr Lee Hiang Kwee, revised the manuscript drafts.
- A/Prof Ling Xing Yi, Dr Lee Yih Hong, and Dr Shi Wenxiong designed the research.
- I and Dr. Yang Yijie performed the experiment and data analyzed at the School of Physical and Mathematical.
- Dr. Lay Chee Leng, Chu Rongrong, Pang Yee Ling, conducted the sample preparation and collected the SEM image at the School of Physical and Mathematical Sciences.

Chapter 3 and **chapter 4** are published as Ya-Chuan Kao, Xuemei Han, Yih Hong Lee, Hiang Kwee Lee, Gia Chuong Phan-Quang, Chee Leng Lay, Howard Yi Fan Sim, Vanessa Jing Xin Phua, Li Shiuan Ng, Chee Wai Ku, Thiam Chye Tan, In Yee Phang, Nguan Soon Tan, Xing Yi Ling. Multiplex Surface-Enhanced Raman

Scattering Identification and Quantification of Urine Metabolites in Patient Samples within 30 min. *ACS Nano* ***14****, 2542−2552* (*2020*). DOI: /10.1021/acsnano.0c00515.

The contributions of the co-authors are as follows:

- Prof Ling Xing Yi, Prof Tan Nguan Soon, and Dr Ku Chee Wai suggested the materials area and edited the manuscript drafts.
- I wrote the drafts of the manuscript. The manuscript was revised together with Dr Han Xuemei, Dr Lee Yih Hong, and Dr Lee Hiang Kwee.
- I, Dr. Lay Chee Leng, Sim Howard Yi Fan Sim, and Dr Phan-Quang Gia Chuong performed all the materials synthesis, collect and analyzed SERS data, and conducted data evaluation.
- All authors read and commented on the manuscript.

18/03/2022

. . . . . .

Date

. . . . . .

Kao Ya-Chuan

Abstract

Surface-enhanced Raman scattering (SERS) spectroscopy is an advanced analytical technique for bioanalysis. However, one of the key challenges that impedes SERS for actual biomolecule detection is due to two reasons: 1) the intrinsically low Raman activities of biomolecules and 2) the lack of interactions between the analyte and plasmonic nanoparticles. The objectives of my thesis is to address these limitations to achieve the practical applications using SERS spectroscopy via platform design and modification of the plasmonic nanoparticles surface chemistry. In chapter 2, we demonstrate a two-part strategy at the oil/water interface to control the single building block morphology over the orientational ordering of supercrystals by tuning surface ligands. In chapter 3 we utilize two types of Ag nanoparticle to form a superhydrophobic SERS detection platform for two urinary metabolites via capture-and confine strategy at the molecule-level. In chapter 4, we follow up the detection strategy from chapter 3 as a proof-of-concept diagnostic kit for spontaneous miscarriage by evaluating the ratio between 5β-pregnane-3α,20α-diol-3α-glucuronide (pregnane) and tetrahydrocortisone (THC). In chapter 5, we further exploit the confine-and-capture strategy for different structural variants analysis. The different binding sites and molecular states of the multiple analytes and probes enable the formation of diversified molecular complexes with different configurations, thus intensifying the specific differences in SERS fingerprints obtained by the various analytes. Lastly, I conclude my thesis with a summary for the different research work and provide an outlook for continuous study in the biomolecule detection and further applications.

Acknowledgements

During the past four years of my graduate studies, I have received tremendous support from many people and I would like to express my appreciation to them.

First and foremost, I am extremely grateful to my supervisor, Assoc. Prof. Ling Xing Yi, for providing me this opportunity to pursue my PhD degree in Singapore. Thank you for your guidance and advice in helping me grow in terms of research skills and personal development. I am also grateful to my thesis advisory committee, Prof. Xing Bengang and Prof. Li Shuzhou for providing invaluable advice and feedback during my time in NTU. Special thanks to Dr. Lee Yih Hong for being a great mentor and friend; thank you for always sharing your experiences and knowledge. Without your help and constructive criticism, I would not have able to complete my degree in time. I am also extremely grateful to my other senior mentors, Dr. Han Xuemei for her counsel in many aspects of my research works. In addition, I would like to my thanks to my brother, Howard Sim Yi Fan, for the help and for concern for my well-being during these four years. I will never forget the journey that we took in our PhD journey, and the challenges we have overcome together.

I would like to express my deepest appreciation to my PhD groupmates, Dr. Lee Hiang Kwee, Dr. Yang Zhe, Dr. Lay Chee Leng and Dr. Phan-Quang Gia Chuong, Dr. Koh Sher Lin Charlynn Leong Shi Xuan, Leong Yong Xiang, and Ng Lishiuan. I have learnt a lot from them, and I really enjoyed the lunch gatherings we had every day. Most importantly, I am deeply grateful to all my groupmates for the great friendship, and I hope we can keep in touch in the future. I am also thankful to all the FYP students, summer undergraduates for their help in the lab. Moreover, I am also grateful to my fellow PhD batchmates, for sharing both chemicals/instrument and the ups and downs of doing research. Last but not least, I would like to express my sincere gratitude to my family for their selfless support and endless care.

Table of Contents

List of Abbreviations

2D	Two-dimensional
3D	Three-dimensional
LSPR	local surface plasmonic resonances
EM	electromagnetic
CE	chemical enhancements
AEF	Analytical enhancement factor
EF	Enhancement factor
Ag	Silver
Au	Gold
R6G	Rhodamine 6G
PVP	Thiol-terminated poly(vinylpyrrolidone)
PEG	Thiol-terminated poly(ethylene glycol)
PDMS	poly(dimethylsiloxane)
FFT	Fast Fourier Transform
AFM	atomic force microscopy
RDF	radial distribution function
MD	molecular dynamics
APTES	3-aminopropyltriethoxysilane
HCl	hydrochloric acid
SPHB substrate	Superhydrophobic substrate
Pregnane	5β-pregnane-3α,20α-diol-3α-glucuronide
THC	tetrahydrocortisone
DFT	Density functional theory
PCA	principal component analysis

PLS	partial least square regression
SVM	Support vector machines
11-MUA	11-mercaptoundecanoic acid
MPBA	4-mercaptophenylboronic acid
MPY	4-mercaptopyridine
CS	chondroitin sulfate
CSA	mono-sulfated
CSC	mono-sulfated
CSD	di-sulfated
CSE	di-sulfated
CST	tri-sulfated CS

Chapter 1: Introduction

Abstract. Surface-enhanced Raman scattering (SERS) is an emerging advanced detection technique which provides molecular structure information by integrating plasmonic nanostructures with Raman spectroscopy. Owing to its fast, molecular specific and ultratrace detection capabilities, SERS has gained much attention in recent biological field involving complex biological matrix. In this chapter, we first introduce the SERS enhancement mechanisms and enhancement factors. Next, we discuss the design and fabrication strategies of highly sensitive SERS platforms. Thirdly, we review on the applications of SERS technique in the biological and biomedical field for target biomarker analysis and disease diagnosis. Finally, we identify the current research gap in the translation of SERS research into real-life application and establish the objectives of this thesis.

1.1 Principles of SERS enhancement

As compared to normal Raman signal, SERS signals from target molecules close to plasmonic nanostructures can be enhanced >10^9-fold.[1-4] These surface-sensitive phenomenon is mainly attributed to two mechanisms: 1) electromagnetic (EM) and 2) chemical enhancements (CE).[3, 10-12] The EM mechanism arises from the surface plasmon of plasmonic nanoparticles upon laser irradiation, which contribute dominantly to the total SERS enhancement with enhancement factor up to 10^8 as compared to the CE which only provides 10^3 enhancement. Notably, the EM enhancement is mainly determined by the optical properties of plasmonic nanoparticles, and it will not be affected any type of molecules.[10, 13] The EM enhancement is induced by the coupling of incoming light with the nanoparticles' electrons to result in localized surface plasmon resonances (LSPR) which generates a localized intense EM field. The LSPR and hence EM field can be tuned by controlling the shape of the nanostructure, dielectric functions, and/or via plasmonic coupling with neighboring particles to create regions of intense and concentrated EM field known as hotspots.[14] Conventionally, silver (Ag), gold (Au) and copper (Cu) are commonly utilized as plasmonic materials owing to its ability to conduct surface plasmon resonance in the visible light to near-infrared region.[15, 16] More importantly, Ag possesses the most effective plasmonic behavior and greatest SERS activity.[17]

On the other hand, CE arises from a charge-transfer mechanism, which enhances the analytes' polarizability through the interactions between plasmonic surface and analyte. Notably, the contribution from CE enhancement only encompasses up to ~10^3 which limits its applications involving chemical species such as thiolated molecules.[18] Nevertheless, both EM and CE are crucial factors that aid to improve the SERS detection performance to achieve ultra-trace detection level with high sensitivity when the analytes are close to plasmonic surfaces.

1.2 Strategies for enhancing SERS platforms performance

Owing to the significant signal enhancements from EM mechanism, most strategies are focused on manipulating the plasmonic nanoparticle arrangement through bottom-up self-assembly approaches.[19] Organizing nanoparticles into an array can result in strong plasmonic hotspots via plasmonic coupling between neighboring nanoparticles, which can create intense and consistent EM field enhancements across centimeter scale.[20] However, due to the surface-sensitive phenomenon, the field enhancements caused by these hotspot engineering strategies are only effective when the analyte is close enough to the plasmonic surface to be able to access these hotspots (Figure 1-1).[19, 21, 22,] To overcome this challenge, 2D/3D platforms are emerging solutions to enhance SERS signals and/or manipulate analyte close to the plasmonic surface.[23, 24] In this section, We discuss the contemporary strategies used for 2D substrate to boost SERS performance.

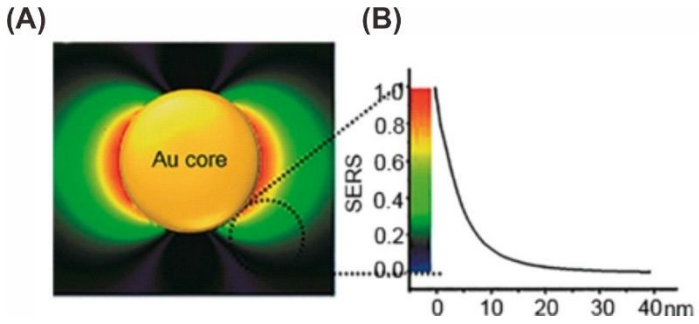

Figure 1-1. (A) Schematic shows the finite difference time domain (FDTD) simulation of the

electric field distribution of an Au NP. (B) The plot shows the intensity of SERS enhancement on the distance from Au surfaces. Reproduced with permission ref 24. Copyright 2013 American Chemical Society.

1.2.1 Two dimensional (2D) assembly of nanoparticles

2D plasmonic nanoparticles/nanostructures array assembly is most commonly employed due to the presence of strong and consistent SERS-active area resulting from the

plasmonic coupling between neighboring nanoparticles.[25-27] The 2D assemble nanoparticles can be made/used directly without any substrate or transferred onto supporting substrate.[28] In this sub-section, we will only focus on commonly used bottom-up approaches which are controlled by various interactions such as electrostatic interactions, hydrogen bonding and van der Walls interactions within the nanoparticles. [20. 27-29]

Bottom-up preparation of 2D SERS platforms is typically achieved by utilizing nanoparticle self-assembly, and the liquid-air and liquid-liquid approaches are the most common method for the fabrication of 2D assembly.[25] For liquid-air or liquid-liquid techniques, nanoparticles are spontaneously adsorbed to the interface to minimize interfacial free energy.[30-32] This allows the particles to form a close-packed metacrystals and this assembly method have been demonstrated using various type of nanoparticles.[20] Such stable adsorption phenomena at the interfaces provide a versatile method to control nanoparticle organization and by extension, the strength of electromagnetic field enhancement in the resulting metacrystal.

Langmuir-Blodgett method (Figure 1-2) is generally used to form 2D metacrystal at the liquid-air interface by adding a non-polar, immiscible nanoparticle solution over the aqueous layer.[33] Then, the compactness is modulated by systematically altering the surface pressure. For example, the particle density of Ag nanoparticles is increased while increasing the surface pressure. The increase in particle density causes the color of particle assembly to change from yellow to metallic silver which indicates that the plasmon coupling is increased between the particles.[29]

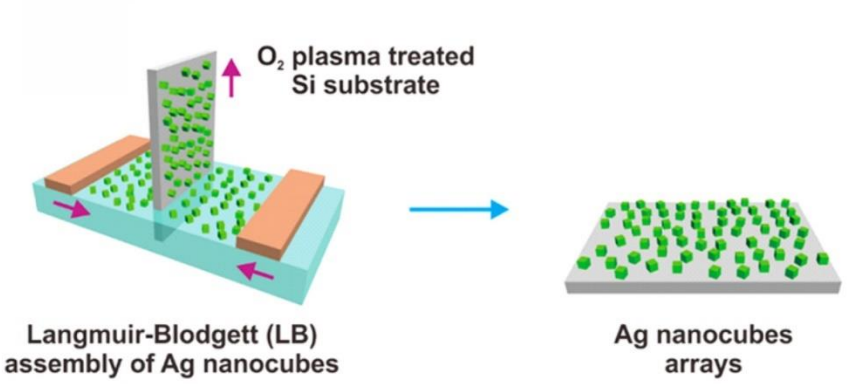

Figure 1-2. Schematic of Langmuir-Blodgett assembly method at liquid-liquid interfacial. Reproduced with permission ref 29. Copyright 2013 American Chemical Society.

For liquid-liquid interface, the assembly is typically formed at two different densities of solvent, such as water and low polarity organic solvents. This method presents two liquid phases to provide additional hydrophobic/hydrophilic interaction between the nanoparticles.[30] Such interaction enables the modulation of the particle orientation and particle interfacial position to create different metacrystals.[27, 34, 35] A notable example here is the concept to use a shape-controlled Ag nanoparticle to create multiple superlattices (Figure 1-3). The concept of this work is to program shape-controlled Ag nanoparticle as a building block and manipulate the hydrophilicity/hydrophobicity of particle surface to create different interactions between the particle surfaces and two liquid phases. This creates several types of metacrystals assembly using shape-controlled nanoparticle as building block, including close-packed and several type of open structures.[27] Notably, the standing hydrophobic Ag nanocubes exhibit a hexagonal array with a packing density of 24 % (Figure 1-4). Although the Ag nanocubes packing density is relatively low, the field enhancement is about 26-fold stronger than that exhibited by the square close-packed array (100 % packing density) while using 532 nm laser. Most importantly, the SERS enhancement factor is 350-fold higher than the square close-packed array. These results show that “more is not always better” for 2D metalcrystal assembly, which completely

changes the belief that maximizing the number of nanoparticles into a same space is necessary to create high SERS performance. The bottom-up approaches thus show the potential for metacrystal assembly and optimal 2D hotspot engineering to control electromagnetic field enhancements.

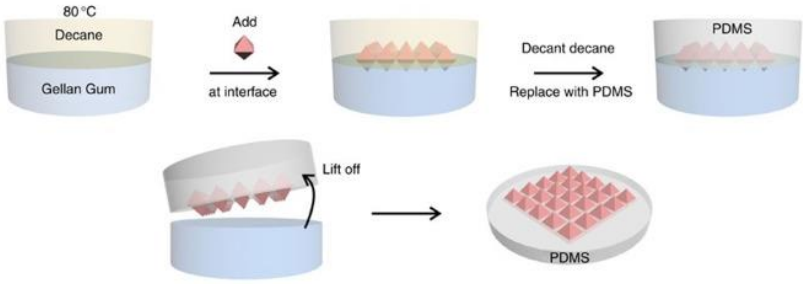

Figure 1-3. Schematic of gel-trapping technique to create multiple superlattices of nanoparticles at liquid-liquid interfacial. Reproduced with permission ref 27. Copyright 2015 Nature publication group.

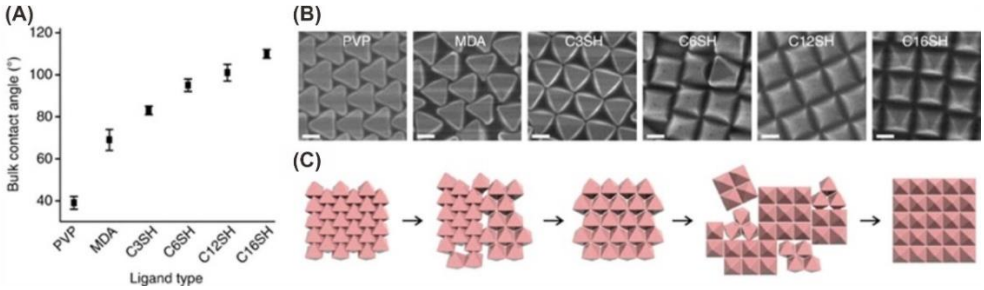

Figure 1-4. (A) The contact angle changes when Ag film functionalized with different thiol group. (B) Ag octahedra packing packing patterns transit from hexagonal close-packed superlattice to the open hexagonal metacrystal and into the square packing while increasing hydrophobicity. All scale bars, 200nm. (C) Schematic shows the transition process between three types of superlattices. Reproduced with permission ref 27. Copyright 2015 Nature publication group.

Although the 2D assembled substrate is able to provide strong electromagnetic field enhancement, the lack of any specific surface functionalization on SERS substrate generally results in hydrophilic surface and the analytes typically spread across the substrate during their drying.[29] Such analyte spreading dilutes the molecular surface concentration on SERS substrate effectively, which becomes a significant challenge in obtaining reproducible and strong SERS signals for trace detection.

1.2.2 Molecule enrichment by Superhydrophobic SERS platforms

Physical strategy is a promising approach to enrich target molecules directly in the SERS-active region because they are not restricted to the chemical nature of analyte and are crucial for molecular detection at ultratrace concentration. As compared to hydrophilic substrates, superhydrophobic (SPHB) SERS platforms are capable of confining liquid samples into a small contact area, emerging as a new method to detection highly dilute aqueous samples. A surface is considered superhydrophobic if its effective contact angle droplet is equals to or bigger than 150^{o}. Notably, the contact angle is measured through the liquid whereby the liquid-vapor interface meets the solid surface. [36] By creating microscale or nanoscale surface roughness and modifying the surface with hydrophobic chemical functionality, water-repellent test shows that the water contact angle can achieve more than 150^{o} on SPHB substrates.[37] SPHB substrates exhibiting Cassie-Baxter wetting states are more efficient in achieving superior concentrating effect. The analytes thus will be confined within a localized area on the SERS substrate during drying, enabling detection limits down to attomolar range.

SPHB surfaces are common in nature, and in fact some of them have been used to make as green SERS platforms. For example, the taro leaf exhibit hierarchical micro-/nanostructures, comprising micro-papilla on its surfaces. Thus, this unique tiny structure

makes the leaf exhibit superhydrophobicity and exhibit contact angle of 154°.[38] By coating 20 nm of Ag nanoparticles onto the leaf surface to impart SERS activity, and it allows 4 μL of rhodamine 6G droplet to concentrate on taro-leaf@Ag platform to form an area of 0.3 mm^2. Thus, the corresponding analyte concentrating factor is about 43-fold higher than the normal hydrophilic surface.

The taro-leaf@Ag exhibits high signal reproducibility (R.S.D = 9.7 %) and the detection limit can reach 10^{-8} M with an enhancement factor of around 10^6 on this platform. The taro-leaf@Ag substrate has also been used for the detection of furazolidone, a prohibited aquaculture drug. However, structural variations in the naturally-occurring hierarchical micro-/nanostructures can induce the differences in surface wettabilities during processing, which affects the sensitivities of such SERS platforms.

The bottom-up approaches are the most straightforward method to create SPHB 2D substrates, since its can achieved by large-area assemblies of plasmonic particles, followed by surface chemical functionalization to induce superhydrophobicity on the surface. Additionally, the crystalline nanoparticles can boost the SERS enhancement effectively as compared to polycrystalline Ag film. The first bottom-up fabricated SPHB SERS platform is prepared by the assembly of Ag nanocubes at the air-liquid interface then followed by coating with an additional Ag layer via thermal evaporation and chemical surface modification with perfluorodecanethiol.[39] By studying the impacts of the nanocubes density and surface roughness on the different substrate, the advancing contact angle can reach 169°. To determine the contact angle hysteresis, advancing and receding contact angles are measured from dynamic experiments. The advancing contact angle can be described as a measure of the liquid-solid cohesion. Advancing contact angles can be measured directly at the advancing edge of a liquid drop.[40] By comparing SPHB with normal hydrophilic surface, the SPHB platform performs 14-fold smaller contact area upon droplet drying. The R6G

analytical enhancement factor is 10^{11} and the detection limit can reach 10^{-16} M with only 1 µL analyte solution. This detection method is able to create great opportunities for high-efficiency and cost-/time-effective sensing of biomolecules, drug, and food additives.

1.3 SERS in bio-applications

To date, SERS is increasingly utilized as a detection technique in the biological field, due to its high sensitivity that can reach the single molecule level, non-invasive nature and ability to perform multiplex detection, such as SERS in cellular imaging,[41, 42] DNA detection,[43, 44] drug detection is blood plasma.[24, 45] Because the fluctuation of pH, and temperature changes can easily affect the stability of bioanalytes, SERS can be a promising technique which is able to obtain spectra from solution mixture directly without causing analytes decomposition (Figure 1-5).[46, 47] For instance, core shell Ag@Au nanoparticles have demonstrated its ability to detect histone acetyltransferase p300 which is an important transcriptional coactivator protein.[48] Furthermore, by integrating SERS with microfluidic devices, it enables the detection of nine types of E. coli strains within a microfluidic device.[49] Notably, the resulting SERS spectra provides clear fingerprint of each molecule hence allow successful classification by chemometric analysis. Moreover, owing to the tunability of SERS excitation wavelength to enable near-IR range operations, this prevents the sample from exhibiting fluorescence and photodegradation of biomolecules.

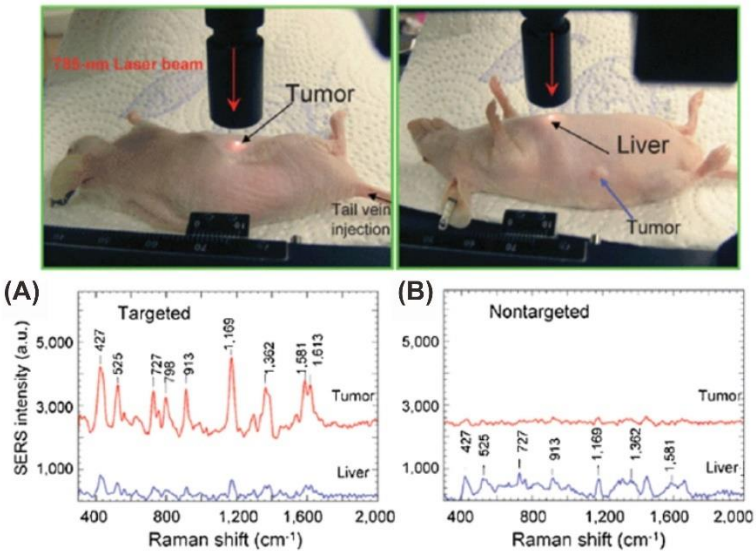

Figure 1-5 In vivo cancer targeting and surface-enhanced Raman detection. Top: Photographs showing a laser beam focusing to the tumor site or to the anatomical location of liver. Lower: SERS spectra obtained from the tumor and the liver locations by using (A) targeted and (B) nontargeted nanoparticles. Two nude mice bearing human head and neck squamous cell carcinoma (Tu686) xenograft tumor (3 mm diameter) received 90 uL of ScFv EGFR-conjugated SERS tags or pegylated SERS tags (460 pM). In vivo SERS spectra were obtained from the tumor site (red) and the liver site (blue) with 2s signal integration and at 785 nm excitation. Reproduced with permission ref 46. Copyright 2010 Wiley.

Owing to the advantages of SERS, one area in which SERS has high potential to be employed is in metabolomic studies. Metabolomics combines analytical technologies with statistical and multi-variant methods for identification and quantification of cellular metabolites, and is a rapidly emerging field for functional genomics research.[50, 51] Metabolomics is considered as broadcasting signals from metabolites which are able to reveal the physiological state of organism. The metabolites are downstream products from the organisms, which are linked to the phenotype closely.[52-54] Recently, many types of metabolites from our body have been studied by using different types of analytical

technologies for qualification and quantification, such as organisms,[51] tissues or fluids, either identified or unknow compounds. Mass spectrometry is the main detection technique to analyze many metabolites at a same time, since it can be coupled to different types of machines, such as high-performance liquid chromatography (HPLC-MS), and gas chromatography mass spectroscopy (GC-MS). For example, the Parkinson's disease has been studied by using liquid chromatography coupled with electrochemical coulometric array detection (LCECA) method to discover the biomarker in plasma.[55] Although current results hold promises in this detection strategy, there are several bottlenecks in metabolomic analysis which remains unresolved. For instance, current detection strategy is unable to analyze the whole metabolome profile due to the huge variety of chemical structures and abundance difference. Furthermore, for chromatography, large amount of sample is needed. Ion suppression will affect the sample recovery and sample loss will occur during the concentrating and detection process. Moreover, biological sample often requires complicated sample preparation such as solid phase extraction and liquid-liquid extraction to reduce interferences caused by the matrices which will result in poor separation efficiency and inaccurate retention times. Most importantly, chromatography and mass spectroscopy are expensive, cumbersome, and have long detection times, which are not viable for routine point-of-care diagnostics.[56] Thus, there is a need to go beyond conventional analytical techniques to overcome the current bottlenecks in biomolecular detection which provide opportunities in drug development and identify novel biomarker for medical diagnosis.

Given the vast advantages of SERS in bio-applications, SERS is highly suitable for metabolomic studies because it has the ability to provide a multiplex detection with short detection period and high accuracy. Furthermore, SERS has the capability to discriminate many classes of biologically relevant molecules that is not possible via MS. For example,

SERS can identify and quantify nicotine and two of its major metabolites which have similar chemical structures (Figure 1-6).[57] Another example is to make use of the mirror effect for oxytocin detection under single gold nanosphere on a metal film junction which can enhance the surface enhancement to achieve single molecule detection.[58] However, the current challenge that is impeding SERS as an efficient biomedical profiling tools arises from the lack of high-performance SERS platform with ultrasensitive detection. Therefore, it is necessary to create a highly sensitive SERS-active nanostructures surface for those without specific interaction and low-concentration metabolites in a complex biological sample. In addition, most of metabolite molecules suffer from low Raman cross-section and weak affinity with the SERS-active surfaces, resulting in SERS spectra with low signal-to-noise ratio and low reproducibility. As such, a point-of-care and universal SERS platform with high performance is much needed for metabolites detection in biological samples.

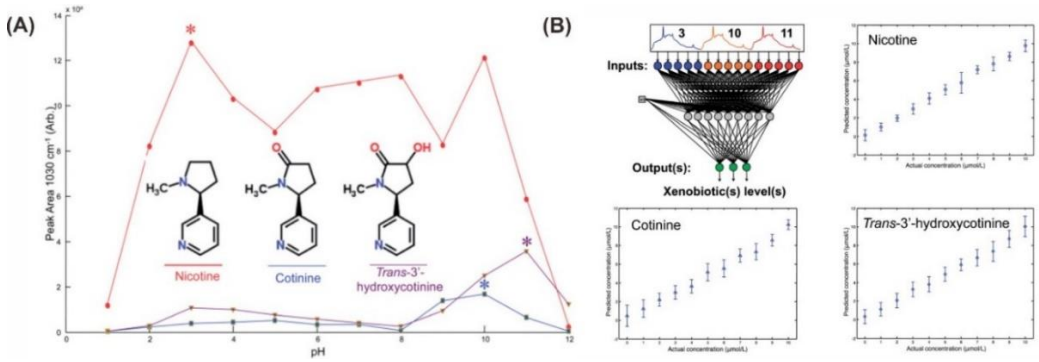

Figure 1-6. (A) pH profiling SERS results from the nicotine, cotinine and trans-30-hydroxycotinine under investigation. The peak area averages at 1030 cm^{-1} were calculated from the 15 replicate spectra at each pH for each of the analytes. (B) Schematic of the artificial neural network (ANN) predictions trained with the input SERS data from mixtures of nicotine, cotinine and trans-30 -hydroxycotinine at all three pH conditions. Points show the averages of the test data only with standard deviation error bars. Reproduced with permission ref 56. Copyright 2014 Royal Society of Chemistry.

1.4 Motivations and objectives

Therefore, the fabrication of plasmonic nanoparticles via assembly and surface functionalization has permitted significant improvement in SERS performance which has potential applications in diverse fields ranging from metabolites detection to environmental detections. Using plasmonic nanoparticles as building blocks to create 2D metacrystals generate plasmonic platforms with strong hotspots and affords trace molecule detection applications. The superhydrophobicity of the platforms also potentially overcomes the current bottleneck arising from the low analyte concentration on the SERS-active region. Moreover, the grafting of specific probe on plasmonic cube overcomes the bottleneck arising from weak analyte affinity to the particle surface. Collectively, these platforms allow SERS to be broadly employed for ultra-trace analyte sensing, multiplex sensing, and reaction monitoring.

Despite the improvements in SERS development, there are still few challenges and research gaps that need to be addressed to further translate SERS research toward applicable application such as for routine point-of-care diagnostics. Firstly, SERS detection for ultratrace small molecules detection which exhibit low Raman scattering cross-sections and do not have interaction with the plasmonic nanoparticle surfaces still remains difficult. An important thing to note is that SERS enhancement will be affected by the distance between the SERS hotspot and the target molecule. Majority of current SERS platform are predominantly designed for those molecules with specific affinity to plasmonic nanoparticles and with large Raman scattering cross-sections as a model analyte to showcase the capability to achieve high SERS enhancement factors. Therefore, surface modification of nanoparticle with different thiol-related ligands as probes can provide a suitable interaction and facilitate our molecule of interest close to nanoparticle surface. Secondly, despite the use of probe molecules to attract the metabolites close to particle

surface, performing multiplex and quantitative molecular detection from a complex matrix is still challenging. This problem is especially notable for biomolecules because the structural differences in the carbon skeleton often affects how the molecule functions in organism. However, in the context of biological molecules, the nature of hydrocarbon molecule come in many different forms, which remain a challenge for SERS analysis.

Given the advantages of superhydrophobic substrate and the use of different probe molecules, it is thus ideal to combine two strategies to achieve an ultrasensitive plasmonic platform capable of improving SERS sensitivity of biomolecules and detecting structure isomers. Moving beyond molecule sensing, we also anticipate the development of the superhydrophobic SERS substrate to create a practical detection device for clinical application.

The objective of my thesis is therefore to overcome the aforementioned limitations and translate SERS to real world applications by assembling plasmonic nanoparticles and selecting the surface probe for high SERS sensitivity. In chapter 2, we used one nanoparticle shape to achieve two types of orientationally distinct supercrystals, including plastic crystals and uniform metacrystals. Our strategy enhances supercrystal diversity for polyhedra comprising multiple nondegenerate facets by integrating multi-faceted Archimedean polyhedral with surface polymeric interaction to tune nanoparticle orientational order during self-assembly. In chapter 3 and 4, we conduct “capture-and-confine” strategy to significantly increase the SERS sensitivity for identification and quantification of two urinary metabolites. Particularly, in chapter 3, we design and fabricate optimized 2D nanoparticle array of two types of Ag nanoparticles to create highly sensitive SPHB SERS substrate with superior analyte concentrating effect toward high SERS sensitivity. We employ the nanoscale surface chemistry on SERS-active Ag nanocubes to chemically capture the target urinary metabolites. In chapter 4, we further exploit the SPHB substrate

as a detection platform and develop a diagnostic kit toward point-of-care threatened miscarriage detection. The chemometric analysis will be used to build a prediction model to distinguish high-risk pregnant patients who eventually suffer a miscarriage with a high accuracy. In chapter 5, we present a SERS fingerprinting approach with intensified specificity over structural isomers, whereby the spectral data is acquired by diversifying their chemical interaction moieties with a surface functional probe. Finally, I conclude my thesis with a summary of my research works and provide an outlook for the future progress of SERS based metabolomics. The motivation is not just to create a niche area for onsite detection, but to simultaneously reveal the molecular-level understanding between plasmonic surface-analyte interactions. The insights gained from the increased molecular understanding lay the foundation of employing SERS technique for clinical studies.

References

1. Willets, K. A.; Duyne, R. P. V. *Annu. Rev. Phys. Chem.* **2006**, 58, 297.
2. Sun, Y.; Xia, Y. *Science* **2002**, 298, 2179.
3. Ding, S.-Y.; You, E.-M.; Tian, Z.-Q.; Moskovit, M. Chem. Soc. Rev. **2017**, 46, 4076.
4. Halas, N. J.; Lal, S.; Chang, W.-S.; Link, S.; Nordlander, P. *Chem. Rev.* **2011**, 111, 3961.
5. Chumanov, G. D.; Efremov, R. G.; Nabiev, I. R., J. Raman spectrosc, **1990**, 21, 43-48.
6. Mulvaney, S. P.; Musick, M. D.; Keating, C. D.; Natan, M. J. *Langmuir* **2003**, 19, 4790.
7. Maltzahn, G. v.; Centrone, A.; Park, J.-H.; Ramanathan, R.; Sailor, M. J.; Hatton, T. A.; Bhatia, S. N. *Adv. Mater*. **2009**, 21, 3180.
8. Tian, F.; Conde, J.; Bao, C.; Chen, Y.; Curtin, J.; Cui, D. *Biomaterials* **2016**, 106, 97.
9. Bukasov, R.; Shumaker-Parry, J. S. *Nano Lett.* **2007**, 7, 1118.
10. Knoll, W. *Annu. Rev. Phys. Chem.* **1998**, 49, 638.

11. Sharma, B.; Frontiera, R. R.; Henry, A.-I.; Ringe, E.; Duyne, R. P. V. *Mater. Today* **2012**, 15, 25.
12. Li, J.-F.; Zhang, Y.-J.; Ding, S.-Y.; Panneerselvam, R.; Tian, Z.-Q. *Chem. Rev.* **2017**, 117, 5069.
13. Ru, E. C. L.; Grand, J.; Fe´lidj, N.; Aubard, J.; Le´vi, G.; Hohenau, A.; Krenn, J. R.; Blackie, E.; Etchegoin, P. G. *J. Phys. Chem. C* **2008**, 112, 8121.
14. Ru, E. C. L.; Etchegoin, P. G.; Meyer, M. *J. Chem. Phys.* **2006**, 125, 204701.
15. Cardinal, M. F., Vander Ende, Hackler, E., R. A., McAnally, M. O., Stair, P. C., Schatz, G. C., Van Duyne, R. P. *Chem. Soc. Rev.*, **2017**, 46, 3886.
16. Sharma, B., Frontiera, R. R., Henry, A.-I., Ringe, E., Van Duyne, R. P. *Mater. Today*, **2012**, 15, 16.
17. Zeman, E. J., Schatz, G. C. *J. Phys. Chem.*, **1987**, 91, 634.
18. Morton, S. M.; Jensen, L. *J. Am. Chem. Soc.* **2009**, 131, 4098.
19. Lee, H. K.; Lee, Y. H.; Koh, C. S. L.; Phan-Quang, G. C.; Han, X.; Lay, C. L.; Sim, H. Y. F.; Kao, Y.-C.; An, Q.; Ling, X. Y. *Chem. Soc. Rev.* **2019**, 48, 756.
20. Lee, H. K.; Lee, Y. H.; Phan-Quang, G. C.; Han, X.; Koh, C. S. L.; Ling, X. Y. Chem. Mater. **2017**, 29, 6577.
21. Liu, K.; Bai, Y.; Zhang, L.; Yang, Z.; Fan, Q.; Zheng, H.; Yin, Y.; Gao, C. *Nano Lett.* **2016**, 16, 3681.
22. Yang, M.; Alvarez-Puebla, R. n.; Kim, H.-S.; Aldeanueva-Potel, P.; Liz-Marza´n, L. mM.; Kotov, N. A. *Nano Lett.* **2010**, 10, 4019.
23. Liu, S.; Tang, Z. *J. Mater. Chem.* **2009**, 20, 35.
24. Zong, C.; Xu, M.; Xu, L.-J.; Wei, T.; Ma, X.; Zheng, X.-S.; Hu, R.; Ren, B. *Chem. Rev.* **2018,** *118*, 4980.

25. Tanoue, Y.; Sugawa, K.; Yamamuroa, T.; Akiyama, T. *Phys. Chem. Chem. Phys.* **2013**, 5, 15805.

26. Pincella, F.; Song, Y.; Ochiai, T.; Isozaki, K.; Sakamoto, K.; Miki, K. *Chem. Phys. Lett.* **2014**, 605, 120.

27. Lee, Y. H.; Shi, W.; Lee, H. K.; Jiang, R.; Phang, I. Y.; Cui, Y.; Isa, L.; Yang, Y.; Wang, J.; Li, S.; Ling, X. Y. *Nat. Commun.* **2015**, 6990.

28. Lu, Y.; Liu, G. L.; Lee, L. P. *Nano Lett.* **2005**, 5, 9.

29. Lee, H. K.; Lee, Y. H.; Zhang, Q.; Phang, I. Y.; Tan, J. M. R.; Cui, Y.; Ling, X. Y. *ACS Appl. Mater. Interfaces* **2013**, 21, 11418.

30. Lin, Y.; Skaff, H.; Emrick1, T.; Dinsmore, A. D.; Russell, T. P. *Science* **2003**, 299, 229.

31. Booth, S. G.; Dryfe, R. A. W. *J. Phys. Chem. C* **2015**, 119, 23309.

32. Binder, W. H. *Angew. Chem.* **2005**, 44, 5175.

33. Tao, A.; Sinsermsuksakul, P.; yang, P. *Nat. Nanotechnol.* **2007**, 2, 440.

34. Yang, Y.; Lee, Y. H.; Lay, C. L.; Ling, X. Y. *Chem. Mater.* **2017**, 29, 6144.

35. Yang, Y.; Lee, Y. H.; Phang, I. Y.; Jiang, R.; Sim, H. Y. F.; Wang, J.; Ling, X. Y. *Nano Lett.* **2016**, 16, 3878.

36. Bansil, R.; Turner, B. S. *Curr. Opin. Colloid Interface Sci.* **2006**, 6, 2.

37 Li, X.-M.; Reinhoudt, D.; Crego-Calama, M. *Chem. Soc. Rev.* **2007**, 36, 1368.

38. Huang, J.-A.; Zhang, Y.-L.; Zhao, Y.; Zhang, X.-L.; Sunb, M.-L.; Zhang, W. *Nanoscale* **2016**, 8, 11493.

39. Lee, H. K.; Lee, Y. H.; Zhang, Q.; Phang, I. Y.; Tan, J. M. R.; Cui, Y.; Ling, X. Y. *ACS Appl. Mater. Interfaces* **2013**, 5, 11418.

40. Lam, C.N.C.; Wu, R., Li, D., Hair, M.L., Neumann, A.W. *Adv. Colloid Interface Sci*. **2002**, 96, 169.

41. Lahr, R. H.; Vikesland, P. J., *ACS Sustainable Chem. Eng.* **2014**, 2, 1608.

42. Xu, H.; Li, Q.; Wang, L.; He, Y.; Shi, J.; Tang, B.; Fan, C., *Chem. Soc. Rev.* **2014,** *43*, 2661.

43. Kang, T.; Yoo, S. M.; Yoon, I.; Lee, S. Y.; Kim, B. *Nano Lett.* **2010**, 10, 1193.

44. He, Y.; Su, S.; Xu, T.; Zhong, Y.; Zapien, A.; Li, J.; Fan, C.; Lee, S.-T. *Nano Today* **2011**, 6, 130.

45. Sun, F.; Hung, H.-C.; Sinclair, A.; Zhang, P.; Bai, T.; Galvan, D. D.; Jain, P.; Li, B.; Jiang, S.; Yu, Q. *Nat. Commun.* **2016**, 7, 13437.

46. Qian, X. M.; Nie, S. M. *Chem. Soc. Rev.* **2008**, 37, 920.

47. A, R. n.; Alvarez-Puebla; Liz-Marza´n, L. M. *Small* **2010**, 6, 610.

48. Aroca, R. F.; Alvarez-Puebla, R. A.; Pieczonka, N.; Sanchez-Cortez, S.; Garcia-Ramos, J. V. *Adv. Colloid Interface Sci.* **2005**, 116, 61.

49. Walter, A.; März, A.; Schumacher, W.; Rösch, P.; Popp, J. *Lab Chip* **2011**, 11, 1021.

50. Cevallos-Cevallosa, J. M.; Reyes-De-Corcueraa, J. I.; Edgardo Etxeberriaa; Danyluka, M. D.; Rodrick, G. E. *Trends Food Sci. Technol.* **2009**, 20, 566.

51. Sabatine, M. S.; Liu, E.; Morrow, D. A.; Heller, E.; McCarroll, R.; Wiegand, R.; Berriz, G. F.; Roth, F. P.; Gerszten, R. E. *Circulation* **2005**, 112, 3875.

52. Das, K. M.; Eastwood, M. A.; McManus, J. P. A.; Sircus, W. *N. Engl. J. Med.* **1973**, 289, 495.

53. Park, J. H.; Pyun, W. Y.; Park, H. W. *Cells* **2020**, 9, 2308.

54. Lennard, M. S.; Silas, J. H.; Freestone, S.; Ramsay, L. E.; Tucker, G. T.; Woods, H. F. *N. Engl. J. Med.* **1982**, 307, 1560.

55. Bogdanov, M.; Matson, W. R.; Wang, L.; Matson, T.; Saunders-Pullman, R.; Bressman, S. S.; Beal, M. F. *Brain* **2008**, 131, 396.

56. Manchikanti, L.; Malla, Y.; Wargo, B. W.; Fellows, B., *Pain Physician* **2011**, 14, 270.

57. Alharbi, O.; Xu, Y.; Goodacr, R. *Analyst* **2014**, 139, 4827.

58. Li, L.; Hutter, T.; Steinerc, U.; Mahajan, S. *Analyst* **2013**, 138, 4578.

Chapter 2: Modulating Orientational Order to Organize Polyhedral Nanoparticles into Plastic Crystals and Uniform Metacrystals

Abstract. In nanoparticle self-assembly, the current lack of strategy to modulate orientational order creates challenges in isolating large-area plastic crystals. Here, we achieve two orientationally distinct supercrystals using one nanoparticle shape, including plastic crystals and uniform metacrystals. Our approach integrates multi-faceted Archimedean polyhedra with molecular-level surface polymeric interactions to tune nanoparticle orientational order during self-assembly. Experiments and simulations show that coiled surface polymer chains limit interparticle interactions, creating various geometrical configurations among Archimedean polyhedra to form plastic crystals. In contrast, brush-like polymer chains enable molecular interdigitation between neighboring particles, favoring consistent particle configurations and result in uniform metacrystals. Our strategy enhances supercrystal diversity for polyhedra comprising multiple nondegenerate facets.

2.1 Introduction

Gaining control over the translational and orientational order among polyhedral nanoparticles is critical to create structurally diverse supercrystals, because tailoring the precise spatial organization of these building blocks is key to achieve unique collective optical,[1-7] magnetic,[8-10] and electronic[11-14] behaviors. Polyhedral nanoparticles are particularly attractive building blocks, because the presence of different crystal facets, vertices, as well as edges enables them to pack in a variety of geometrical configurations.[15-29] Thus far, successful modulation of the translational parameters to achieve long-range periodicity has given rise to a multitude of large area supercrystals with different structures[30-41] Typically, supercrystals with long-range translational order can be broadly classified as (1) uniform metacrystals exhibiting orientational order where building blocks achieve consistent alignment in the crystal structure, or (2) plastic crystals with reduced orientational order in which the building blocks orientate randomly in their lattice positions. To date, there is no strategy to modulate orientational parameters and controllably isolate the resulting plastic crystals over large areas for further investigations on macroscopic material behaviors. Majority of reported plastic crystals are observed under tightly controlled transient experimental conditions or arise erroneously in the irreversible atomic surface attachment of neighboring particles during self-assembly.[42-45] In contrast to this scarcity of nanoparticle-based plastic crystals, molecular plastic crystals formed using imidazolium salts,[46] pyrrolidium salts,[47] and fullerenes[48-49] have already demonstrated superior ionic conductivity as well as temperature-independent thermal conductivity. Such unique properties arise from the local orientational disorder within the molecular plastic crystal structures, which further result in rapid ion transport capabilities that are otherwise unachievable in fully crystalline lattices.[50] These observations certainly create an impetus

to gain orientational control among nanoparticles, such that plastic crystals can be controllably isolated for further material investigations.

Here, we successfully modulate nanoparticle orientational order during liquid-liquid interfacial self-assembly to achieve two orientationally distinct supercrystals using a single nanoparticle morphology, including plastic crystals and uniform metacrystals. Our two-part strategy combines the use of multi-faceted Archimedean Ag polyhedra with tunable polymeric surface interactions to modulate orientational order. In the first part, we exploit the different non-identical crystal facets on the nanoparticles to form plastic crystal and uniform metacrystal: contact between non-identical facets creates orientational disorder characteristic of plastic crystals, whereas contact between identical facets establishes orientational order reminiscent of a uniform metacrystal (Scheme 2-1). The second part of our strategy introduces thiolated poly(vinylpyrrolidone) (PVP) and poly(ethylene glycol) (PEG) as model polymeric surfactants on the polyhedral nanoparticle surfaces to modulate the orientational order of these building blocks.

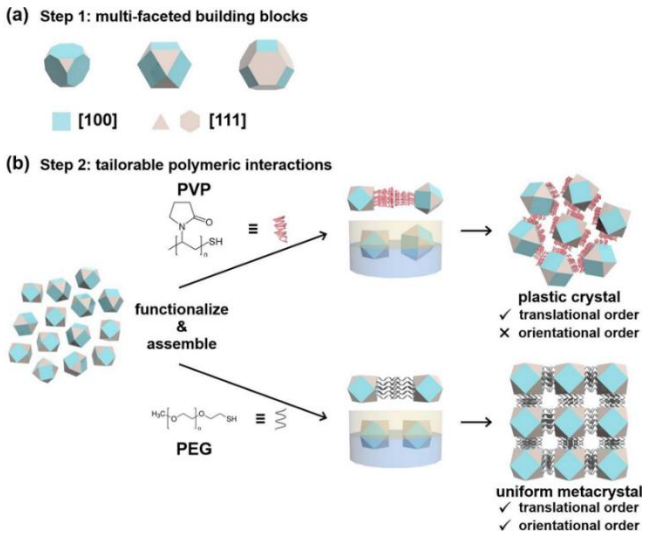

Scheme 2-1. A two-part strategy to achieve two orientationally distinct supercrystals, including plastic crystal and uniform metacrystal. (a) The first part of the strategy begins with choosing multi-faceted building blocks such as Ag truncated cubes, cuboctahedra, and truncated octahedra. [100] facets are highlighted in cyan, whereas [111] facets are

highlighted in latte colors. (b) The second part uses polymer surface functionalities to introduce tailorable molecular interactions onto the nanoparticle surfaces. Thiol-terminated poly(vinylpyrrolidone) (PVP) chains coil up on the polyhedra's surfaces during self-assembly at the oil/water interface, resulting in a lack of interparticle interactions. The particles thus rotate independently and adopt various geometrical configurations at the interface, leading to plastic crystal formation. Thiol-terminated poly(ethylene glycol) (PEG) enables molecular interdigitation which helps to lock the building blocks and achieve consistent interfacial geometrical configurations, leading to the formation of uniform metacrystals.

Our experiments and simulations collectively show that despite having similar macroscopic and nanoscopic properties, conformational differences between PVP and PEG chains on the nanoparticle surfaces lead to the formation of plastic crystals and uniform metacrystals, respectively. Simulations reveal that PVP chains adopt a coiled-up conformation on the particle surfaces and limit interparticle interactions. Consequently, PVP-functionalized polyhedra rotate independently and exhibit various interfacial geometrical configurations during self-assembly. This culminates in plastic crystals which exhibit long-range translational order but significantly reduced orientational order. In contrast, brush-like PEG conformation on the polyhedra surfaces enables molecular interdigitation between PEG chains on neighboring particles and enhances the orientation of PEG-functionalized particles to generate uniform metacrystals. These uniform metacrystals possess long-range translational and orientational order. Our approach is broadly applicable to Archimedean polyhedra, including truncated cubes, cuboctahedra, and truncated octahedra. By using two-dimensional (2D) metacrystal assembly as a proof-of-concept to uncover key factors for orientational control, our approach opens additional

possibilities in supercrystal design and facilitates subsequent studies on the material properties of these supercrystals.

2.2 Results and discussion

To implement our two-part strategy in modulating the orientational parameters of the supercrystals, we use truncated Ag nanocubes, cuboctahedra, and truncated octahedra with various non-identical crystal facets as building blocks (Scheme 2-1a). To tailor the surface interactions of the Ag polyhedra prior to self-assembly, the nanoparticles are functionalized with a self-assembled monolayer of linear thiol-terminated polymers through standard ligand exchange reactions, including poly(vinylpyrrolidone) (PVP) and poly(ethylene glycol) (PEG) with ~15 and 20 monomer units, respectively. We employ the gel-trapping technique to organize the building blocks into supercrystals at the oil/water interface (Figure 2-1). By isolating the resulting supercrystals in-situ at the interface right after nanoparticle self-assembly, this technique enables us to directly attribute the factors generating any orientational variation to our strategy.

Figure 2-1. Schematic illustration of gel-trapping self-assembly for the formation of 2D plasmonic metacrystals. The aqueous phase comprises 2 wt% Gellan Gum and we use decane as the oil phase to conduct the experiment at 80°C. The functionalized Ag polyhedra are added to the interface and the set up is allowed to equilibrate before cooling down to room temperature. The aqueous phase gels at room temperature, trapping the assembled metacrystals at the interface and enabling the oil phase to be decanted. A premixed liquid of poly(dimethylsiloxane) (PDMS) is then poured over the metacrystals and allowed to

polymerize. After polymerization, the PDMS film can be lifted off for subsequent characterization.

Using Ag cuboctahedra comprising six square [100] and 8 triangular [111] facets as a model system, we observe two orientationally distinct supercrystals using different polymeric functionalizations: plastic crystal from PVP functionalization and uniform metacrystal from PEG functionalization (Figure 2-2). PVP-functionalized Ag cuboctahedra assemble into a hexagonal lattice with reduced orientational order (Figure 2-2a, i-iii). Color coded SEM image reveals high orientational disorder within this plastic crystal: 41 % and 59 % of the cuboctahedra orient in the square [100] and triangular [111] facets facing up configurations, respectively (Figure 2-2a, ii, c).

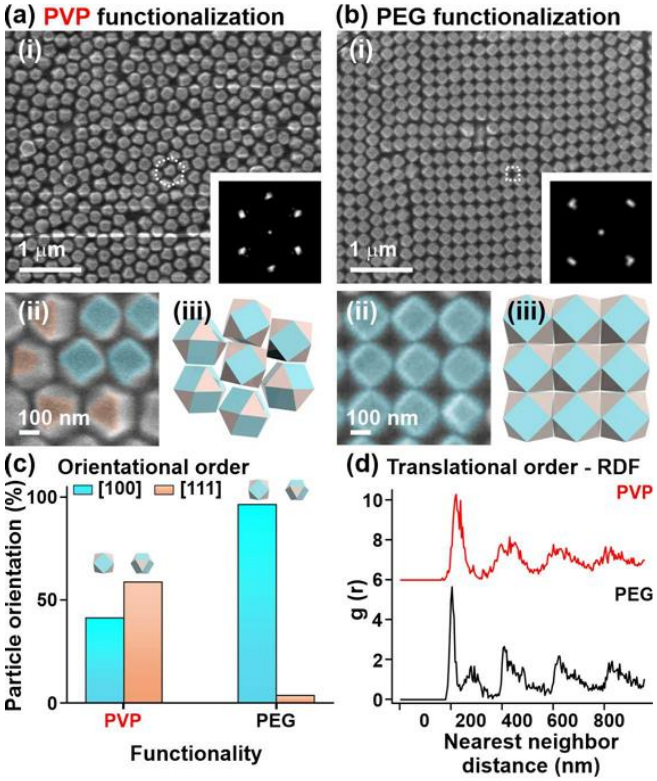

Figure 2-2. Forming two orientationally-distinct supercrystals using Ag cuboctahedra. (a) Functionalizing Ag cuboctahedra with PVP results in a plastic crystal. (i) SEM and (ii) close-up image of the plastic crystal. White dotted lines in (i) show the unit cell, and the

inset in (i) is the Fast Fourier Transform (FFT) of the plastic crystal. FFT analysis is used to provide information on the particle packing arrangements.[51] SEM image in (ii) is color coded to highlight the different particle orientations, with cyan and latte colors representing [100] and [111] facets respectively. (iii) Schematic illustration of the plastic crystal. (b) Functionalizing Ag cuboctahedra with PEG results in a uniform metacrystal. (i) SEM and (ii) close-up image of the uniform metacrystal. White dotted lines in (i) show the unit cell, and the inset in (i) is the FFT of the uniform metacrystal. SEM image in (ii) is color coded to highlight the particle orientations. (iii) Schematic illustration of the uniform metacrystal. (c) Orientational analyses of the supercrystals organized from the respectively functionalized Ag cuboctahedra. (d) Radial distribution function analyses of both supercrystals indicate long-range translational order.

In this mixture of particle orientations, neighboring particles contact each other via a combination of square-to-square and square-to-triangle facets, corresponding to [100]-[100] and [100]-[111] configurations, respectively (Figure 2-2a, iii). While the orientational order of this structure is low, radial distribution function (RDF) analyses of this supercrystal demonstrate good translational order and periodicity (Figure 2-2d). The RDF describes how the density of surrounding matter varies as a function of the distance and periodicity.[52] Multiple peaks show up in the RDF profile, which are indicative of consistent long-range nearest neighbor distances (Figure 2-2d, red line). The various facet-to-facet contacts in this plastic crystal gives rise to a relatively high estimated packing efficiency of 75 %, indicating that this structure is thermodynamically stable (Figure 2-3). On the other hand, PEG-functionalized Ag cuboctahedra form a square close-packed metacrystal (Figure 1b, i-iii). Particle orientation analyses indicate good orientational order, with ~ 95 % of the Ag cuboctahedra in this metacrystal oriented in the square [100] facet facing upwards

configuration (Figure 2-1b, ii, c). Neighboring particles predominantly contact each other via the square [100] facets (Figure 1b, iii). RDF analyses show good long-range translational order, and the packing efficiency of this metacrystal is 83 % (Figure 2-1d, black line, Figure 2-4). These observations demonstrate the successful implementation of our strategy to modulate the orientational parameter of our building blocks. More importantly, our strategy enables the formation and isolation of nanoparticle-based plastic crystals over areas of 4 cm^2 for the first time (Figure 2-5).

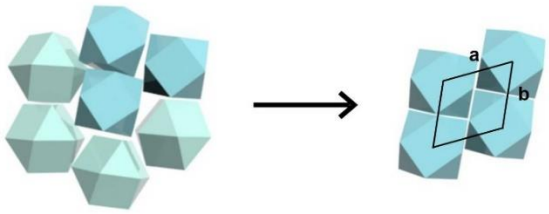

Figure 2-3. Estimating the packing efficiency of the plastic crystal formed using PVP-functionalized Ag octahedra. The packing efficiency is estimated to be 75 %. The simplest repeat unit of the open structure corresponds to a rhombic repeat unit as shown above. As with the nature of plastic crystals which exhibit reduced orientational order, the repeat unit can change from area to area. We have simplified the repeat unit to facilitate the calculations. Consequently, the estimated 75 % is likely an overestimate. See the calculation in appendix.

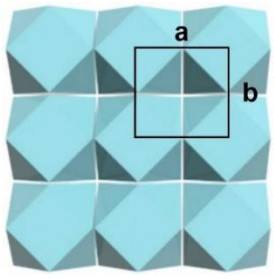

Figure 2-4. Packing efficiency of metacrystal organized using PEG-functionalized Ag cuboctahedra. The simplest repeat unit of the metacrystal is shown by the black square above.

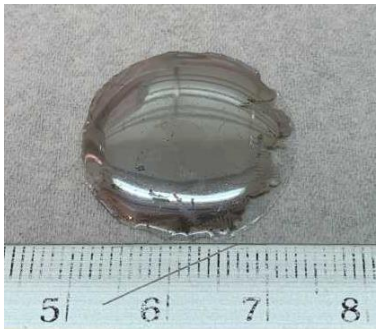

Figure 2-5. Digital image of a typical supercrystal formed using our strategy can form a large area of assembly.

The formation of two orientationally distinct supercrystals using the same building blocks but different polymeric surface functionalities indicates that PVP and PEG play critical roles in the self-assembly process. We examine their roles in our self-assembly experiments at three different levels, beginning from the macroscopic level before systematically scaling down to the nanoscopic and molecular regimes. The macroscopic level relates to the bulk surface hydrophilicity of these two polymers, which can be characterized by measuring the static contact angles of PVP- and PEG-functionalized Ag-coated substrates using water and decane. Both polymer-functionalized bulk Ag surfaces exhibit similar static water contact angles of ~ 40^{o} and static decane contact angles of ~ 25^{o}, indicating that both polymers have similar hydrophilicity and their bulk surface wettabilities do not contribute towards the difference in supercrystal structure (Figure 2-6a).

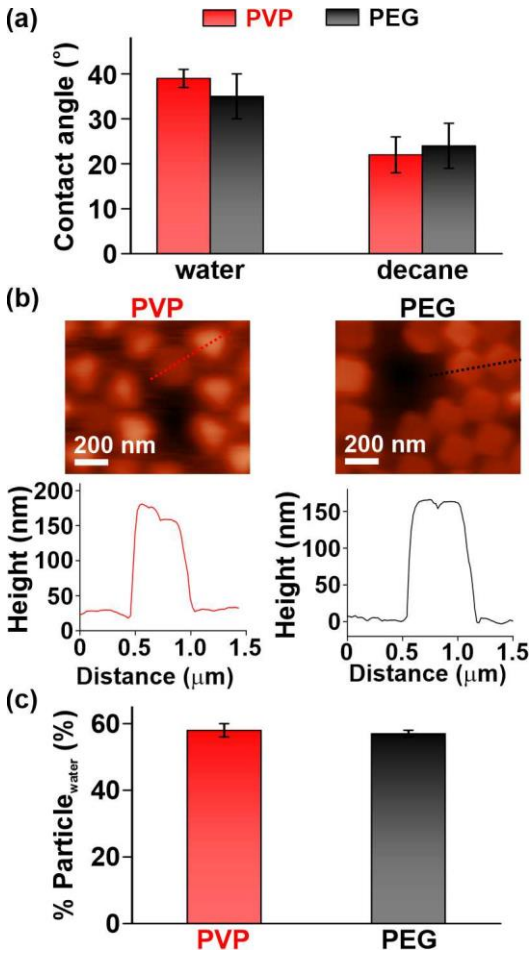

Figure 2-6. (a) Contact angle measurements of PVP- and PEG-functionalized Ag films using water and decane. (b) AFM images (top) and height profiles (below) of PVP- and PEG-functionalized Ag cuboctahedra. (c) Relative amounts of PVP- and PEG-functionalized Ag cuboctahedra in contact with the aqueous phase.

Next, we direct our focus to the nanoscopic level and characterize how PVP and PEG functionalization affects the nanoparticle orientation and position at the oil/water interface. These two parameters provide insights on how much of these nanoparticles is in contact with both liquid phases at the oil/water interface, and allows us to directly evaluate if nanoscale surface wettability is responsible for the formation of different supercrystals. During metacrystal transfer from the oil/water interface to a PDMS film, part of the Ag cuboctahedra which is in contact with the aqueous phase will be exposed on the PDMS

surface We use atomic force microscopy (AFM) to investigate the orientation and position of the functionalized Ag cuboctahedra. The particle orientation from AFM characterization remains consistent with the SEM images, with PVP-functionalized Ag cuboctahedra adopting a mixture of [100] and [111] facets facing upward orientations and PEG-functionalized ones exhibiting predominantly square [100] facet facing upward orientations (Figure 2-6b).

By using AFM to measure the height profile of the polymer-functionalized Ag cuboctahedra on the PDMS surface, we can further derive the height percentage in contact with the aqueous phase ($\%particle_{water}$) using the relation $\%particle_{water} = (H_{AFM}/H_{orientation}) * 100\ \%$. H_{AFM} relates to the measured height of the Ag cuboctahedra above the PDMS film, and $H_{orientation}$ is the full height of Ag cuboctahedra at the respective orientation. Moreover, both polymer-functionalized Ag cuboctahedra show similar interfacial positions with approximately 57 % of the particles exposed to the aqueous phase (Figure 2-6b). This similarity indicates that both PVP and PEG functionalization gives rise to similar nanoparticle wettability at the oil/water interface, and hence surface wettability at the nanoscale is not key to the formation of orientationally distinct supercrystals at the oil/water interface. Instead, a more nuanced difference between the molecular-level behaviors of these two polymers on the nanoparticle surface might give rise to the different supercrystals using the same building blocks.

At the molecular level, we employ molecular dynamics (MD) simulations to investigate how polymeric interactions between surface functionalities impact the orientational alignment of the Ag cuboctahedra at the interface (Figure 2-7). Briefly, we use all-atomic models to construct Ag cuboctahedra building blocks and the self-assembled monolayer of

PEG or PVP chains on the polyhedra surfaces. This model enables us to accurately account for the interactions between all entities in our system, including the Ag cores, the surface polymer functionalities, and the solvents used in the experiments. Two Ag cuboctahedra are placed in an oil/water interface with their [100] facets facing upwards as the initial configuration, where we define the initial orientational 2-7b).

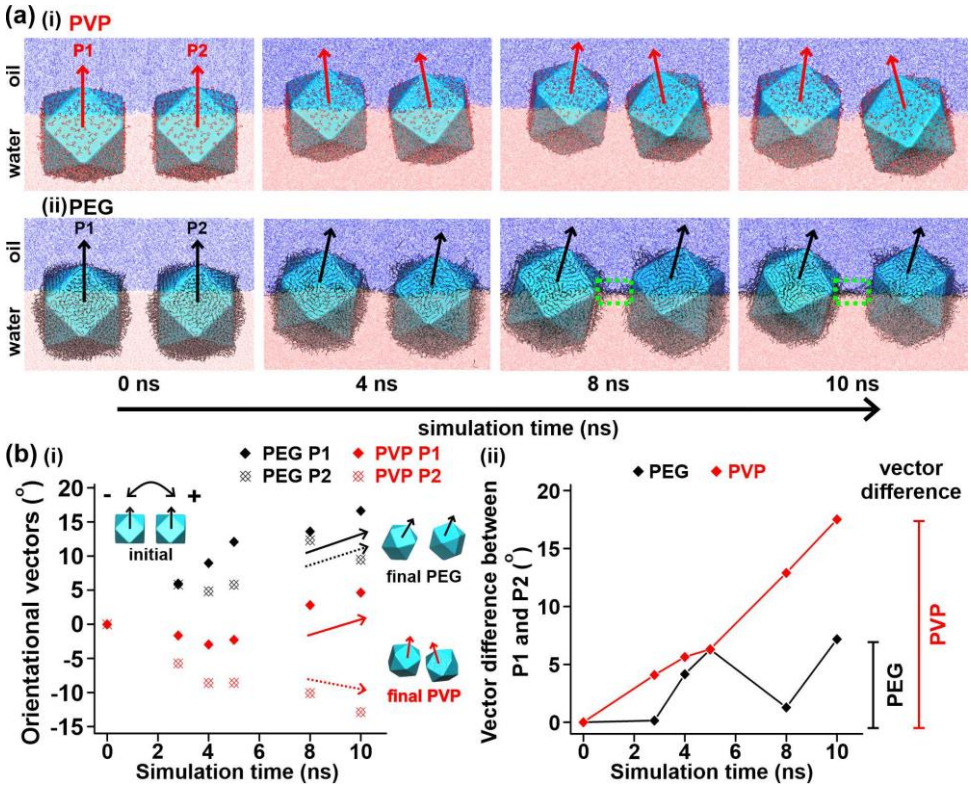

Figure 2-7. Using molecular dynamics simulations to understand the self-assembly process. (a) Simulation snapshots of the self-assembly process between two (i) PVP-functionalized and (ii) PEG-functionalized Ag cuboctahedra. Dashed boxes (green) at 8 ns and 10 ns highlight chain overlaps between PEG chains. (b, i) Changes in the orientational vectors for the Ag cuboctahedra and (ii) difference in the orientational vectors between particle 1 (P1) and particle 2 (P2) over the course of simulations.

Tracking the changes in the orientational vectors provides a quantitative analysis of the orientation variation between the particles over the course of simulation (Figure 2-7a). Orientational changes in the clockwise direction are taken as positive, whereas directional variations in the counterclockwise direction are taken as negative. We observe distinct trends in the orientation changes between the two different polymer-functionalized systems even though they begin with identical initial configurations, and these orientational variations mirror our experimental results (Figure 2-7a). Notably, the two PVP-functionalized Ag cuboctahedra quickly lose their orientational alignment within 4 ns of the simulations, and this orientational difference increases over time (Figure 2-7a, i). Such divergence in building block orientations also manifest quantitatively in the orientational vector changes over time (Figure 2-6b, i, red points). Orientational difference between the two PVP-functionalized particles changes by up to 18^{o} during simulations, highlighting that both particles tumble independently and loses orientational alignment at the oil/water interface (Figure 2-7b, ii). In contrast, the two PEG-functionalized Ag cuboctahedra largely maintain their orientational alignment relative to each other throughout the same duration of simulations (Figure 2-7a, ii). The orientational vectors between the two PEG-functionalized Ag cuboctahedra remain mostly synchronized with each other, with smaller than 7^{o} flux in their relative orientations (Figure 2-7b, i and ii, black points). The slight tilt of the PEG-functionalized Ag cuboctahedra likely arises from Brownian motion at the oil/water interface. The collective observations from these simulations corroborate well with our experimental findings, in which PVP-functionalized building blocks do not maintain orientational order at the oil/water interface and PEG-functionalized particles largely preserve their orientation over the course of simulations.

A closer examination of the simulation snapshots reveals important conformational differences between PVP and PEG chains on the Ag cuboctahedra surfaces, which holds the key to the observation of unique supercrystals. PVP chains adopt a more coiled up conformation because of the apolar backbone, and both the amide and thiol functionalities can potentially interact with the Ag surfaces (Figure 2-7a, i, Figure 2-8a). Furthermore, there is a lack of interactions between the coiled PVP chains on the neighboring particles. The nanoparticles thus behave as independent entities and rotate freely at the interface, in turn leading to a huge difference in the orientation vectors between the two particles. The sequential simulation snapshots show a progressive change from [100]-[100] contact between the two cuboctahedra to resemble that of [100]-[111] contact over the course of simulations, with the triangular [111] facet of particle 2 turning towards the square [100] facet of particle 1 (Figure 2-7a, i). This loss of orientational order between the building blocks parallels our experimental observations, which eventually culminates in large area plastic crystal formation.

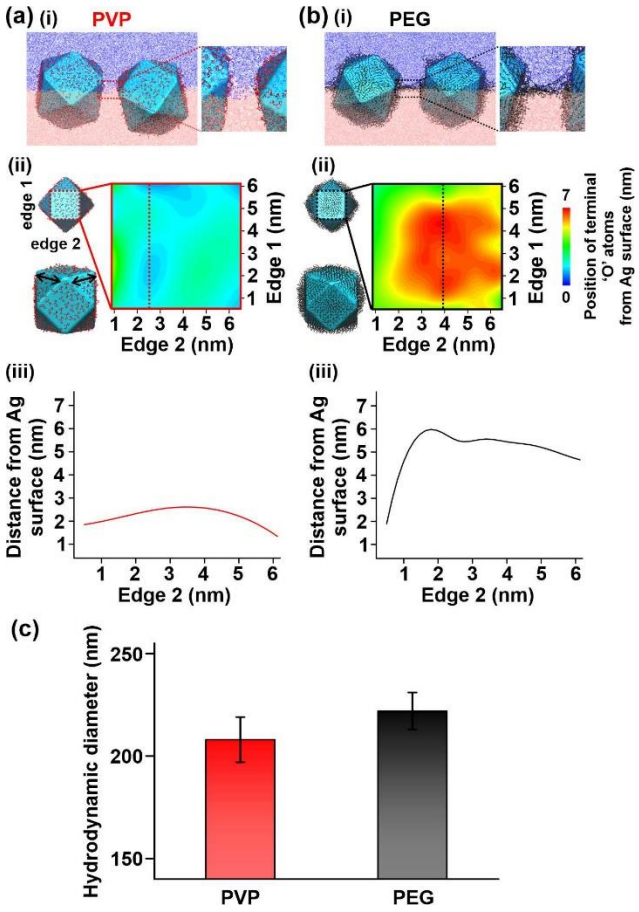

Figure 2-8. Analyzing the surface interactions and conformations for (a) PVP- and (b) PEG-functionalized Ag cuboctahedra. (i) Close-up simulation snapshots taken at simulation time = 10 ns. (ii, iii) Height profiles of PVP-functionalized Ag cuboctahedra surface derived from molecular dynamics simulations. Two-dimensional plots are shown in (ii), and (iii) representative line profile across the surface, corresponding to the dashed lines in (ii). (c) Experimental measurements for the hydrodynamic diameters of the respectively functionalized Ag cuboctahedra.

In contrast, we observe a small population of the PEG chains between the two Ag cuboctahedra beginning to overlap from 8 ns onwards, implying the occurrence of molecular interdigitation (Figure 2-7a, ii, Figure 2-8b). The linear PEG chains stretch out from the nanoparticle surfaces due to their superior water binding properties along the polymer backbone and attachment onto the Ag surface via a single thiol functionality. Such

brush-like conformation facilitates molecular interdigitation between PEG chains on the neighboring particles, which can provide orientational alignment capabilities between the Ag cuboctahedra to maintain [100]-[100] facet contact and result in uniform metacrystal formation. During supercrystal formation, these molecular-level interactions can potentially provide unique orientational alignment capabilities for PEG-functionalized Ag cuboctahedra and lead to the formation of uniform metacrystals. In addition, experimental hydrodynamic measurements further demonstrate that PVP chains are less extended than PEG chains on the Ag cuboctahedra surfaces, corroborating well with findings from our simulations which demonstrate how molecular-level interactions between the polymer chains on neighboring nanoparticles can modulate the orientational parameters of the resulting supercrystals (Figure 2-8c).

In addition to Ag cuboctahedra, our approach to modulating orientational order can also be extended to other Archimedean solids such as truncated cubes and truncated octahedra (Figure 2-9a-d). The surface area ratio between all the [100] and all the [111] facets ranges from 8.4 for truncated cubes to 1.7 for cuboctahedra, and 0.3 for truncated octahedra respectively, indicating that a slight truncation giving rise to different crystal facets is sufficient to achieve plastic crystals. PVP functionalization results in the formation of plastic crystals for both truncated cubes and truncated octahedra, whereas PEG functionalization of the same building blocks assemble into uniform metacrystals. PVP-functionalized truncated cubes form quasi-hexagonal structure with long-range translational order (Figure 2-9a, b, I, j). There is high orientational disorder among the building blocks within the array: 55 % of the building blocks are predominantly oriented with the square [100] facets facing upwards, and the remaining building blocks are oriented with the triangular [111] facets facing upwards (Figure 2-9i). As for PVP-functionalized truncated

octahedra, we observe a hexagonal close-packed plastic crystal with good translational order but low orientational order (Figure 2-9c, d, i, j). ~ 68 % of the building blocks are oriented with [111] hexagonal facet facing upwards, and 32 % of the remaining particles are split between [110] edge and [100] facet facing upwards (Figure 2-9i).

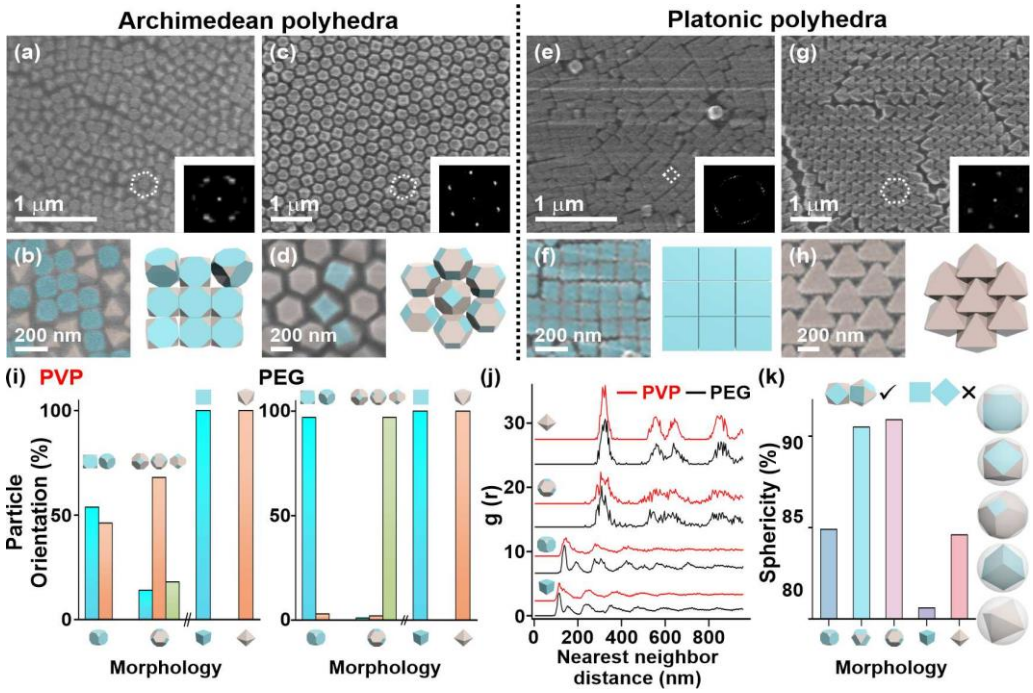

Figure 2-9. Different types of supercrystals assembled using PVP- and PEG-functionalized Ag polyhedra. (a-h) Plastic crystals are formed using PVP-functionalized Ag polyhedra, including (a, b) truncated nanocubes and (c, d) truncated octahedra, whereas uniform metacrystals are formed using (e,f) nanocubes and (g, h) octahedra. Insets are the corresponding FFT images. Unit cells are highlighted by the dashed white lines. (b, d, f, h) Close-up SEM image (left) and corresponding schematic illustration of the metacrystal (right). SEM images are color coded to highlight the different facets, with cyan and latte colors representing [100] and [111] facets respectively. (i) Orientational analysis of the metacrystals formed using (left) PVP- and (right) PEG-functionalized Ag polyhedra. (j) Radial distribution function analysis of all supercrystals indicate long-range translational order. (k) Sphericity of the various building blocks.

In contrast, PEG-functionalization results in uniform metacrystals which enable overlap between the facets of the building blocks. PEG-functionalized truncated cubes organize into a square close-packed metacrystal with long-range translational order and good orientational order with 97 % of the square [100] facets facing upwards (Figure 2-9i, j, Figure 2-10a). PEG-functionalized truncated octahedra organize into a hexagonal close-packed metacrystal exhibiting good translational and orientational order (Figure 2-9i, j, Figure 2-10b). Nearly all building blocks oriented in the [110] edge facing upwards configurations (Figure 2-9i). The [110] edge facing upward orientation allows greater overlap between the facets of neighboring particles than the structure with the [111] facets facing upward (Figure 2-10e).

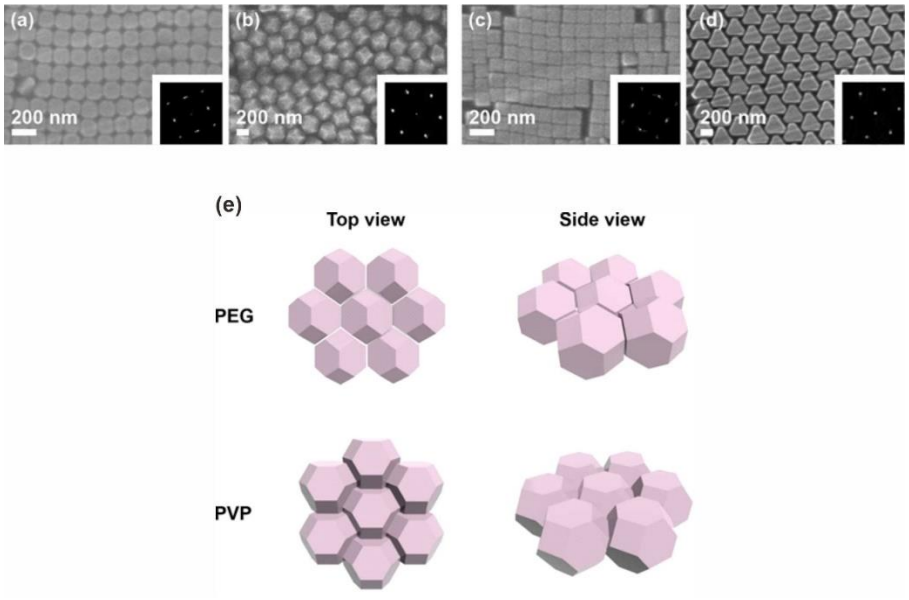

Figure 2-10. Uniform metacrystals formed by PEG-functionalized (a) truncated nanocubes, (b) truncated octahedra, (c) nanocubes, and (d) octahedra. (e)Schematic illustration depicting the different packing patterns for PEG- and PVP-functionalized truncated octahedra. Maximal facet overlap can be achieved using PEG-functionalized truncated octahedra, whereas PVP-functionalized particles only allow half the facets to overlap.

In addition to the importance of molecular-level interactions in driving plastic crystal formation, the ease of organizing plastic crystals using Archimedean polyhedra arises from their high sphericity. Sphericity is a commonly used parameter to compare how closely an anisotropic polyhedral resembles an isotropic sphere, which has a sphericity of 100 % and thus exhibits essentially unlimited orientational freedom. Archimedean building blocks exhibit sphericities with values ranging from 87 to 91%, and this resemblance to a sphere results in a higher orientational freedom (Figure 2-9k, Table 2-1). The presence of [100] and [111] facets on these nanoparticles allow them to approach each other in various facet-overlapping configurations, which gives rise to a mixture of particle orientations in the resulting plastic crystals, including square-square, square-triangle, square-hexagonal, and hexagonal-hexagonal (Figures 2-2 and Figure 2-9). To further support our argument, we show that Platonic nanoparticles such as cubes and octahedra do not form plastic crystals using our two-part strategy, because they are uniformly faceted with either [100] or [111] facets on their surfaces and have lower sphericities of 81 – 85 %. Favorable overlap between the facets of neighboring building blocks can only occur via identical square-square or triangle-triangle configurations. Consequently, both PEG- and PVP-functionalized Ag nanocubes assemble into similar uniform square close-packed metacrystals with good translational and orientational order (Figure 9e, f, i, j, Figure 2-10c). Likewise, both PEG- and PVP-functionalized Ag octahedra organize into uniform hexagonal close-packed metacrystals with long-range translational and orientational ordering (Figure 2-9g, h, i, j, Figure 2-10d). Nevertheless, we note that a slight vertex truncation such as in the case of truncated nanocubes is sufficient to drive plastic crystal formation using our approach. Coupled with the ease of using wet-chemistry synthetic protocols to tune building block

morphology, our approach to modulating orientational order can be extended to a variety of multi-faceted building blocks.

Table 2-1. Sphericity of various building blocks.

Morphology	Sphericity (%)
Sphere	100
Truncated Cube	87
Cuboctahedron	91
Truncated Octahedron	91
Cube	81
Octahedron	85

The sphericity of a building block morphology can be calculated using the equation:

$$\text{Sphericity} = \frac{\pi^{\frac{1}{3}}(6V_p)^{\frac{2}{3}}}{A_p} \times 100$$

where V_p refers to the volume of the building block and A_p refers to the surface area of the building block.

2.3 Conclusion

In conclusion, we demonstrate a two-part strategy to successfully gain control over the orientational ordering of polyhedral building blocks, which allows us to create two orientationally-distinct supercrystals for a single building block morphology at the oil/water interface. The combination of multi-faceted building blocks with tailorable polymeric surface interactions leads to the tunable formation of plastic crystals and uniform metacrystals over large areas. Functionalizing polyhedral building blocks such as Archimedean structures with PVP drives plastic crystal formation, whereas PEG functionalization results in uniform metacrystal. Coiled up PVP chains on the particle

surfaces limit molecular-level interactions between neighboring particles which lead to independent interfacial configurations, thus driving the formation of plastic crystals which exhibit long-range translational order but reduced orientational order. On the other hand, brush-like conformations of PEG chains on the nanoparticle surfaces enable molecular interdigitation between neighboring particles, resulting in the formation of uniform metacrystals with long-range translational and orientational order. Our approach to form plastic crystals can be extended to polyhedral nanoparticles with non-identical crystal facets on the nanoparticle surfaces. These nondegenerate facets give rise to high sphericity to enable the nanoparticles to adopt various configurations at the oil/water interface, thereby driving plastic crystal formation without compromising on thermodynamic stability. This ability to achieve plastic crystalline structures creates new opportunities for in-depth investigation of material properties for such plasmonic metacrystals. The use of nanoscale surface chemistry to gain orientational control can further be extended to other non-plasmonic polyhedral morphologies.

2.4 Material and methods

Materials. Silver nitrate (≥99%), 1,5-pentanediol (≥97%), poly(vinylpyrrolidone) (average MW = 55 000 g/mol), poly(ethylene glycol) methyl ether thiol (average MW = 1000 $gmol^{-1}$), isopropyl alcohol, decane (≥99%), and were purchased from Sigma Aldrich; copper(II) chloride (≥98%) was from Alfa Aesar. Ethanol (ACS, ISO, Reag. Ph Eur) was obtained from EMSURE. Poly(N-vinyl pyrrolidone), Ω-thiol-terminated (average MW = 1,700 $gmol^{-1}$) was purchased from Polymer Source, Inc. Silicon elastomer curing agent and silicone elastomer base were purchased from Dow Corning. Gellan Gum (KELKOGEL®) was kindly sponsored by CP Kelco (USA). All chemicals were used without further

purification. Milli-Q water (>18.0 MΩ·cm) was purified with a Sartorius Arium 611 UV ultrapure water system.

Synthesis & purification of shape-controlled Ag polyhedral. The synthesis of shape-controlled Ag polyhedra was carried out via the polyol reduction route,[53] starting first with the synthesis of Ag nanocubes. In a typical nanocube synthesis, 10 mL of $CuCl_2$ (8 $mgmL^{-1}$), PVP (20 $mgmL^{-1}$) and $AgNO_3$ (20 $mgmL^{-1}$) were separately dissolved in PD. 35 µL $CuCl_2$ solution was added to the $AgNO_3$ solution. 20 mL PD was then heated to 190 °C for 10 min. PVP precursor solution will be added into the solution first, then followed by the addition of $AgNO_3$ precursor solution into the round bottom flask. This process is repeated for approximately 20 min. After the synthesis of nanocubes was completed, the injection was continued using more concentrated precursor solutions. 10 mL of $CuCl_2$ (8 $mgmL^{-1}$), 30 mL of PVP (20 $mgmL^{-1}$) and $AgNO_3$ (40 $mgmL^{-1}$) were separately prepared in PD for the synthesis of truncated nanocubes, cuboctahedra, truncated octahedra, and octahedra. The reaction proceeded for 1 – 2 h, depending on the morphology required. For purification, the various Ag polyhedra solutions were separately re-dispersed in 20 mL ethanol after removing the PD via multiple centrifugation rounds, and diluted to approximately 200 mL using an aqueous PVP solution (0.2 gL^{-1}). This solution was then vacuum filtered multiple times using PVDF filter membranes (Durapore®) with pore sizes ranging from 5000 nm, 650 nm, 450 nm and 220 nm to remove impurities before finally dispersing in ethanol.

Ligand exchange reactions. The purified Ag polyhedra dispersion was generally allowed to sediment. 0.5 µL of the sediment was dispersed in ethanol and centrifuged once more before dispersing in 1.5 mL of ethanol/isopropyl alcohol (1:1). 10 µL of 0.1 – 1 mM thiol-terminated polymer solution was then added dropwise to this dispersion under stirring. Ligand exchange was allowed to take place for 4 hrs, followed by 2 rounds of centrifugation,

re-dispersal in 1.5 mL of ethanol/isopropyl alcohol (1:1), and addition of fresh thiol-terminated polymer solution under stirring. This step was continued for another 3 hrs, followed by 3 rounds of centrifugation and washing with isopropyl alcohol/water (1:1). To study the contact angle of PVP- and PEG- we functionalized PVP and PEG ligand on thermally evaporated Ag films by soaking the substrate in a 10 mM thiol solution for at least 12 hrs. This allows the self-assembled monolayers to form before rinsing with ethanol to remove the excess unbound thiols.

Interfacial gel-trapping experiments. 2 wt% gellan gum aqueous solution was used as the water phase and n-decane was used as the oil phase. The gellan gum solution was first heated to approximately 80^{o}C in an oil bath to ensure that the gel was fully hydrated. Subsequently, pre-heated n-decane was added to the top of the gellan gum solution to create the oil phase. Functionalized Ag polyhedra were then added to the oil/water interface and the entire mixture was left at 80^{o}C for approximately 15 min before being allowed to cool slowly to room temperature. Once the gel had set in the aqueous phase, the oil phase was then decanted gently. In place of n-decane, a layer of premixed PDMS precursor mixture (5:1 elastomer:curing agent) was poured over the nanoparticle monolayer and the container was left at room temperature for the PDMS to cure. After the PDMS had hardened, it was lifted off from the gel and washed in hot water. The gelling process did not affect the outcomes of the supercrystal formation.

Characterization. The samples after self-assembly were directly characterized using scanning electron microscopy (SEM) (JEOL-JSM-7600F). Order analyses of the various assembled arrays were characterized using the freeware ImageJ®. The radial distribution function profiles were analyzed by converting the SEM images into a binary format,

followed by the automatic identification of the centers of the Ag polyhedra. Atomic force microscopy (AFM) was used to characterize the topologies in the self-assembled metacrystals on the PDMS molds using a Bruker Dimension ICON® with NanoScope V controller from Bruker. Tapping mode (non-contact mode) image was acquired by using silicon probes (Tap300Al-G with 30 nm aluminium reflex coating) from BudgetSensor®. Contact angles of the functionalized 114-nm thick Ag films were measured on a Theta Lite tensiometer equipped with a Firewire digital camera. Static contact angle was measured with a 4-μL ultrapure sessile water droplet. A total of five readings were taken at different spots on the same substrate for each of the thiol-functionalized Ag film and averaged to obtain the bulk contact angles.

Molecular dynamics (MD) simulations. The GROMACS 4.67[54] simulation package and GROMOS96[55-56] force field were used for our MD simulations. Two neighboring atoms interacted with each other through van der Waals interactions, which was treated using a 12-6 Lennard - Jones (LJ) potential summed over all pairs of atoms i and j. Ag cuboctahedra with ~ 5.2 nm edge length were constructed using an all-atomic model, made up of 21774 Ag atoms and the LJ parameters for Ag atoms were used in previous work.[57] Thiol-terminated PVP and PEG molecular models employed in this study were generated from the small-molecule topology generator PRODRG.[58] PVP chains were adsorbed onto the Ag cuboctahedra surfaces with loose c(2×2) lattice, and PEG chains were adsorbed onto the Ag cuboctahedra surfaces with ($\sqrt{3} \times \sqrt{3}$)R30° structures to form self-assembled monolayers.[59] We used 4 repeat units to represent PEG and 2 repeat units to represent PVP on the Ag cuboctahedra surfaces, which is proportional to the molecular weights of both polymers used experimentally. Water was modeled using the single point charge (SPC) model, with the bond lengths and angles held constant through the SETTLE algorithm.

Bond lengths of molecules were constrained using the LINCS algorithm. The cutoff distance for short-range non-bonded interactions was chosen to be 12 Å and long-range electrostatic forces were computed using the PME method.[60-61]

2.5 Appendix

Calculation of edge length:

- For a cuboctahedron with edge length x,

Length of a $= \sqrt{5/2}\, x$

Length of b $= \sqrt{2}x$

Volume of repeat unit $= \sqrt{5/2}\, x \times (\sqrt{2}x)^2$

$= 2\sqrt{5/2}\, x^3$

Volume of one cuboctahedron $= \frac{5\sqrt{2}}{3} x^3$

Packing efficiency of metacrystal $= \frac{\frac{5\sqrt{2}}{3} x^3}{2\frac{\sqrt{5}}{\sqrt{2}} x^3}$

$= \frac{10}{6\sqrt{5}}$

$= 75\ \%$

- For a cuboctahedron with edge length x, Length of a = $\sqrt{2}x$

Volume of repeat unit $= (\sqrt{2}x)^3$

$= 2\sqrt{2}\, x^3$

Volume of one cuboctahedron $= \frac{5\sqrt{2}}{3} x^3$

Packing efficiency of metacrystal $= \frac{\frac{5\sqrt{2}}{3} x^3}{2\sqrt{2}\, x^3}$

$= \frac{5}{12}\sqrt{2}$

$= 83\ \%$

References

1. M. Juodėnas, T. Tamulevičius, J. Henzie, D. Erts, S. Tamulevičius, *ACS Nano* **2019**, *13*, 9038-9047
2. B. D. Myers, E. Palacios, D. I. Myers, S. Butun, K. Aydin, V. P. Dravid, *Nano Letters* **2019**, *19*, 4535-4542
3. Y. J. Yang, Y. H. Lee, I. Y. Phang, R. B. Jiang, H. Y. F. Sim, J. F. Wang, X. Y. Ling, *Nano Lett.* **2016**, *16*, 3872-3878;
4. Y. H. Lee, W. Shi, H. K. Lee, R. Jiang, I. Y. Phang, Y. Cui, L. Isa, Y. Yang, J. Wang, S. Li, X. Y. Ling, *Nat. Commun.* **2015**, *6*, 6990
5. M. J. Rozin, D. A. Rosen, T. J. Dill, A. R. Tao, *Nat. Commun.* **2015**, *6*, 7325
6. M. Alba, N. Pazos-Perez, B. Vaz, P. Formentin, M. Tebbe, M. A. Correa-Duarte, P. Granero, J. Ferre-Borrull, R. Alvarez, J. Pallares, A. Fery, A. R. de Lera, L. F. Marsal, R. A. Alvarez-Puebla, *Angew. Chem. Int. Ed.* **2013**, *52*, 6459-6463
7. Z. N. Zhu, H. F. Meng, W. J. Liu, X. F. Liu, J. X. Gong, X. H. Qiu, L. Jiang, D. Wang, Z. Y. Tang, *Angew. Chem. Int. Ed.* **2011**, *50*, 1593-1596.
8. P. J. Santos, R. J. Macfarlane, *J. Am. Chem. Soc.* **2020**, *142*, 1170-1174
9. M. Shuai, A. Klittnick, Y. Shen, G. P. Smith, M. R. Tuchband, C. Zhu, R. G. Petschek, A. Mertelj, D. Lisjak, M. Copic, J. E. Maclennan, M. A. Glaser, N. A. Clark, *Nat. Commun.* **2016**, *7*, 10394
10. G. Singh, H. Chan, A. Baskin, E. Gelman, N. Repnin, P. Kral, R. Klajn, *Science* **2014**, *345*, 1149-1153.
11. A. Abelson, C. Qian, T. Salk, Z. Luan, K. Fu, J.-G. Zheng, J. L. Wardini, M. Law, *Nat. Mater.* **2020**, *19*, 49-55
12. J. Zhang, J. L. Zhu, R. P. Li, J. Y. Fang, Z. W. Wang, *Nano Lett.* **2017**, *17*, 362-367

13. Y. Jiao, D. Han, Y. Ding, X. Zhang, G. Guo, J. Hu, D. Yang, A. Dong, *Nat. Commun.* **2015**, *6*, 6420
14. D. V. Talapin, C. B. Murray, *Science* **2005**, *310*, 86-89.
15. W. Shi, Z. Zhang, S. Li, *J. Phys. Chem. Lett.* **2018**, *9*, 373-382
16. Y. J. Yang, Y. H. Lee, C. L. Lay, X. Y. Ling, *Chem. Mater.* **2017**, *29*, 6137-6144
17. W. X. Shi, Y. H. Lee, X. Y. Ling, S. Z. Li, *Nanoscale* **2017**, *9*, 11239-11248
18. R. P. Li, J. Zhang, R. Tan, F. Gerdes, Z. P. Luo, H. W. Xu, J. A. Hollingsworth, C. Klinke, O. Chen, Z. W. Wang, *Nano Lett.* **2016**, *16*, 2792-2799
19. A. Klinkova, R. M. Choueiri, E. Kumacheva, *Chem. Soc. Rev.* **2014**, *43*, 3976-3991
20. C.-W. Yang, C.-Y. Chiu, M. H. Huang, *Chem. Mater.* **2014**, *26*, 4882-4888
21. D. A. Walker, E. K. Leitsch, R. J. Nap, I. Szleifer, B. A. Grzybowski, *Nat. Nanotechnol.* **2013**, *8*, 676-681
22. A. P. Gantapara, J. de Graaf, R. van Roij, M. Dijkstra, *Phys. Rev. Lett.* **2013**, *111*, 015501
23. B. Gao, G. Arya, A. R. Tao, *Nat. Nanotechnol.* **2012**, *7*, 433-437
24. J. Henzie, M. Gruenwald, A. Widmer-Cooper, P. L. Geissler, P. Yang, *Nat. Mater.* **2012**, *11*, 131-137
25. R. Ni, A. P. Gantapara, J. de Graaf, R. van Roij, M. Dijkstra, *Soft Matter* **2012**, *8*, 8826-8834
26. P. F. Damasceno, M. Engel, S. C. Glotzer, *Science* **2012**, *337*, 453-457
27. U. Agarwal, F. A. Escobedo, *Nat. Mater.* **2011**, *10*, 230-235
28. A. Sanchez-Iglesias, M. Grzelczak, J. Perez-Juste, L. M. Liz-Marzan, *Angew. Chem. Int. Ed.* **2010**, *49*, 9985-9989
29. T. Ming, X. Kou, H. Chen, T. Wang, H.-L. Tam, K.-W. Cheah, J.-Y. Chen, J. Wang, *Angew. Chem. Int. Ed.* **2008**, *47*, 9685-9690.

30. B. H.-j. Lee, G. Arya, *Nanoscale* **2019**, *11*, 15939-15957
31. Q.-Y. Lin, J. A. Mason, Z. Li, W. Zhou, M. N. O'Brien, K. A. Brown, M. R. Jones, S. Butun, B. Lee, V. P. Dravid, K. Aydin, C. A. Mirkin, *Science* **2018**, *359*, 669-672
32. J. X. Gong, R. S. Newman, M. Engel, M. Zhao, F. G. Bian, S. C. Glotzer, Z. Y. Tang, *Nat. Commun.* **2017**, *8*
33. X. Ye, J. Chen, M. Eric Irrgang, M. Engel, A. Dong, S. C. Glotzer, C. B. Murray, *Nat. Mater.* **2017**, *16*, 214-219
34. Q. Q. Shi, K. J. Si, D. Sikdar, L. W. Yap, M. Premaratne, W. L. Cheng, *ACS Nano* **2016**, *10*, 967-976
35. A. Castelli, J. de Graaf, M. Prato, L. Manna, M. P. Arciniegas, *ACS Nano* **2016**, *10*, 4345-4353
36. F. Lu, K. G. Yager, Y. G. Zhang, H. L. Xin, O. Gang, *Nat. Commun.* **2015**, *6*, 6912
37. X. Ye, C. Zhu, P. Ercius, S. N. Raja, H. Bo, M. R. Jones, M. R. Hauwiller, Y. Liu, T. Xu, A. P. Alivisatos, *Nat. Commun.* **2015**, *6*, 10052
38. M. P. Boneschanscher, W. H. Evers, J. J. Geuchies, T. Altantzis, B. Goris, F. T. Rabouw, S. A. P. van Rossum, H. S. J. van der Zant, L. D. A. Siebbeles, G. Van Tendeloo, I. Swart, J. Hilhorst, A. V. Petukhov, S. Bals, D. Vanmaekelbergh, *Science* **2014**, *344*, 1377-1380
39. E. R. Chen, D. Klotsa, M. Engel, P. F. Damasceno, S. C. Glotzer, *Phys. Rev. X* **2014**, *4*, 011024
40. X. Mao, Q. Chen, S. Granick, *Nat. Mater.* **2013**, *12*, 217-222
41. Y. H. Lee, C. K. Lee, B. R. Tan, J. M. R. Tan, I. Y. Phang, X. Y. Ling, *Nanoscale* **2013**, *5*, 6404-6412.

42. J. J. Geuchies, G. Soligno, E. Geraffy, C. P. Hendrikx, C. v. Overbeek, F. Montanarella, M. R. Slot, O. V. Konovalov, A. V. Petukhov, D. Vanmaekelbergh, *Commun. Chem.* **2020**, *3*, 28

43. A. R. C. McCray, B. H. Savitzky, K. Whitham, T. Hanrath, L. F. Kourkoutis, *ACS Nano* **2019**, *13*, 11460-11468

44. J.-M. Meijer, J. J. Crassous, *Small* **2018**, *14*, 1802049

45. B. Liu, T. H. Besseling, M. Hermes, A. F. Demirors, A. Imhof, A. van Blaaderen, *Nat. Commun.* **2014**, *5*, 3092.

46. D. R. MacFarlane, J. Huang, M. Forsyth, *Nature* **1999**, *402*, 792-794.

47. P. Wang, Q. Dai, S. M. Zakeeruddin, M. Forsyth, D. R. MacFarlane, M. Grätzel, *J. Am. Chem. Soc.* **2004**, *126*, 13590-13591.

48. E. S. O'Brien, J. C. Russell, M. Bartnof, A. D. Christodoulides, K. Lee, J. A. DeGayner, D. W. Paley, A. J. H. McGaughey, W.-L. Ong, J. A. Malen, X. Y. Zhu, X. Roy, *J. Am. Chem. Soc.* **2018**, *140*, 15601-15605

49. R. C. Yu, N. Tea, M. B. Salamon, D. Lorents, R. Malhotra, *Phys. Rev. Lett.* **1992**, *68*, 2050-2053.

50. A. Basile, M. Hilder, F. Makhlooghiazad, C. Pozo-Gonzalo, D. R. MacFarlane, P. C. Howlett, M. Forsyth, *Adv. Energy Mater.* **2018**, *8*, 1703491.

51. *C. E. Ayres, B. S. Jha, H. Meredith, J. R. Bowman,G. L. Bowlin, S.C. Henderson, D. G. Simpson J. Biomater. Sci. Polym. Ed.* **2012**, 603.

52. G. Mason, *Nature* **1968**, 217, 733.

53. A. Tao, P. Sinsermsuksakul, P. D. Yang, *Angew. Chem. Int. Ed.* **2006**, 45, 4597-4601.

54. K. A. Becraft, F. G. Moore, G. L. Richmond, *J. Phys. Chem. B* **2003**, 107, 3675-3678.

55. D. Van der Spoel, E. Lindahl, B. Hess, G. Groenhof, A. E. Mark, H. J. C. Berendsen, *J. Comp. Chem.* **2005**, 26, 1701-1718

56. C. Oostenbrink, A. Villa, A. E. Mark, W. F. Van Gunsteren, *J. Comput. Chem.* **2004**, 25, 1656-1676.

57. H. Heinz, R. A. Vaia, B. L. Farmer, R. R. Naik, *J. Phys. Chem. C* **2008**, 112, 17281-17290.

58. A. W. Schuttelkopf, D. M. F. van Aalten, *Acta Crystallogr D* **2004**, 60, 1355-1363.

59. J. C. Love, L. A. Estroff, J. K. Kriebel, R. G. Nuzzo, G. M. Whitesides, *Chem. Rev.* **2005**, 105, 1103-1170.

60. T. Darden, D. York, L. Pedersen, *J. Chem. Phys*. **1993**, 98, 10089-10092

61. U. Essmann, L. Perera, M. L. Berkowitz, T. Darden, H. Lee, L. G. Pedersen, *J. Chem. Phys*. **1995**, 103, 8577-8593

Chapter 3: Surface-Enhanced Raman Scattering for Multiplex Identification and Quantification of Biological Small Molecules via Superhydrophobic Substrate

Abstract. Surfaced-enhanced Raman scattering (SERS) technique exhibit a great potential for biomolecule component analysis as it provides specific molecular-level fingerprint information with great signal enhancements. However, SERS detection faces great challenge for small biological molecules at low concentration since small molecules have intrinsically low Raman scattering cross section and generally suffer from weak affinity with plasmonic particle surface. Herein, we demonstrate a "confine-and-capture" strategy to attain SERS-based multiplex identification and quantification of biological small molecules with assistance of chemometric analysis. In our strategy, we employ specific nanoscale surface chemistry to chemically capture the targets near SERS-active Ag nanocubes surface followed by physically confining them on a superhydrophobic SERS platform. Using two urinary metabolites as model molecules, 5β-pregnane-3α,20α-diol-3α-glucuronide (pregnane) and tetrahydrocortisone (THC), our strategy enables their identification and clear discrimination with detection limit as low as 10^{-10} M. By applying chemometric analysis, we convert the molecular fingerprint into quantified information, with near-100% accurate quantification of their contents. Our strategy is general and can be expanded to a variety of biological significant small biomolecules for disease diagnosis and relevant biological function study.

3.1 Introduction

Surface-enhanced Raman scattering (SERS) spectroscopy is an advanced analytical technique,[1-3] which arises from the inelastic light scattering between photon and target molecules in the presence of noble metal nanostructured (Ag, Au, Cu) surfaces.[4-6] SERS signals provide characteristic molecular fingerprints for unambiguous and multiplexed identification of structurally analogues. SERS shows great versatility in biological detection of DNA, cancer biomarkers, and proteins with detection limits reaching attomolar levels.[7,8,9,10] Current most commonly employed analysis methods for traces targets such as gas/liquid chromatography mass spectroscopy (GC/LC-MS) and nuclear magnetic resonance (NMR), generally require complicated sample pretreatment and analyte isolation with several days, and the instruments are expensive.[11, 12] On the other hand, SERS measurement can be performed within seconds without complicated sample purification and the entire instrument setup is highly portable. These collective advantages of SERS empower it to be one of the best candidates to be readily employed as a point-of-care detection of biological molecules for future clinical applications.[13, 14] However, one of the key challenges that impedes SERS for actual biomolecule detection is the intrinsically low Raman activities of biomolecules.[15, 16] This challenge is aggravated as most of the biomolecules exist in highly dynamic and complex fluid at low concentration, which often leads to weak signals and complicated spectra. Hence, an ideal detection strategy is highly required with the ability to enrich the analytes close to nanoparticle surface and enhance SERS sensitivity to provide a clear Raman feature for analysis.

Herein, we demonstrate a two-pronged “confine-and-capture” strategy to efficiently generate the strongest SERS signal enhancement for rapid and ultrasensitive SERS screening of small metabolites with low Raman scattering cross sections. In our strategy, we design a plasmonic-active superhydrophobic SERS platform to physically concentrate

analytes into a ~185-fold smaller area as compared to a hydrophilic substrate. Our target analytes, 5β-pregnane-3α,20α-diol-3α-glucuronide (pregnane) and tetrahydrocortisone (THC), are reported to be miscarriage-relevant urinary metabolites. To selectively capture our target analytes, we graft Ag nanocubes with a self-assembled monolayer of capturing agent that preferentially reacts with the metabolites through covalent interactions. Our strategy generates an analytical SERS enhancement factor (AEF) of 10^{12}. By integrating advanced chemometric analysis, we are capable of identifying and quantifying THC and pregnane down to as low as 10^{-10} M with near 100% accuracy. Our strategy is a universal method that our platform can provide homogeneous intensity and high SERS enhancement for trace molecular detection.

3.2 Results and discussion

3.2.1 Fabrication of SPHB SERS Platform

Compared to normal hydrophilic Au and Ag nanomaterials, a superhydrophobic substrate can overcome the random spreading of analyte on the substrate surface.[17] This can allow us to physically reduce the liquid/solid contact area and effectively concentrate analytes into a small area upon liquid evaporation (Figure 3-1). Thus, the enrichment of the target molecules directly in the SERS-active surface region is favorable for improving the limit of analyte detection by decreasing the contact area.[18]

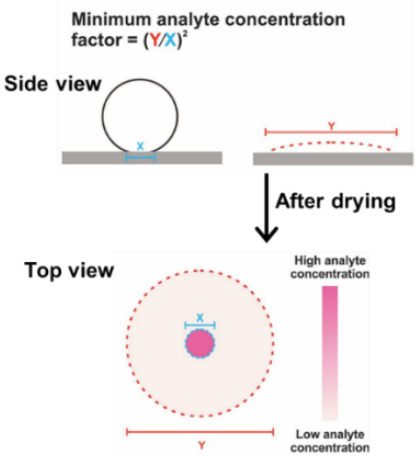

Figure 3-1. The working principle of superhydrophobic substrate over hydrophilic substrate. The X represents the diameter of contact area on superhydrophobic surface. The Y represents the diameter of the contact area on hydrophilic surface.

In the first step of our 'confine-and-capture' strategy, we fabricate a superhydrophobic (SPHB) SERS substrate by employing bottom-up electrostatic assembling technique to form 2D binary Ag nanocubes and octahedra array on a silicon wafer.[19] The Ag nanocube and Ag octahedra exhibit distinctive and strong localized surface plasmon resonances across the visible spectrum due to their excellent monodispersity. Both our synthesized nanocubes and octahedra exhibit > 95 % purity after post-purification. The well-defined tips generate intense electromagnetic field enhancements, and their size difference creates high surface roughness that is essential to achieve superhydrophobicity (edge length = 128 ± 7 and 299 ± 22 nm; Figure 3-2).

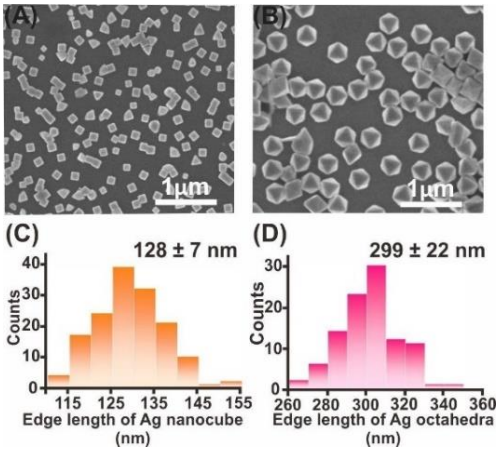

Figure 3-2. Characterization of as-synthesized Ag nanocubes and octahedra. (A) Ag nanocubes and (B) octahedra. Edge length distribution of (C) Ag nanocubes and (D) octahedra.

To perform an electrostatic assembly, we first functionalize the Ag nanoparticles with 11-mercaptoundecanoic acid (11-MUA) to create negatively-charged Ag nanoparticles. After that we modify the Si substrate with 2% v/v 3-APTES and then immerse in pH 5

solution to yield positive charge on Si surface (Figure 3-3 A-D). Subsequently, we submerged the resulting substrate into 2 mL of negatively charged aqueous Ag nanocubes and octahedral mixtures for 20 minutes. After assembly, we perform ligand exchange on the platform with perfluorodecanethiol (PFDT) (Figure 3-3E). [17]

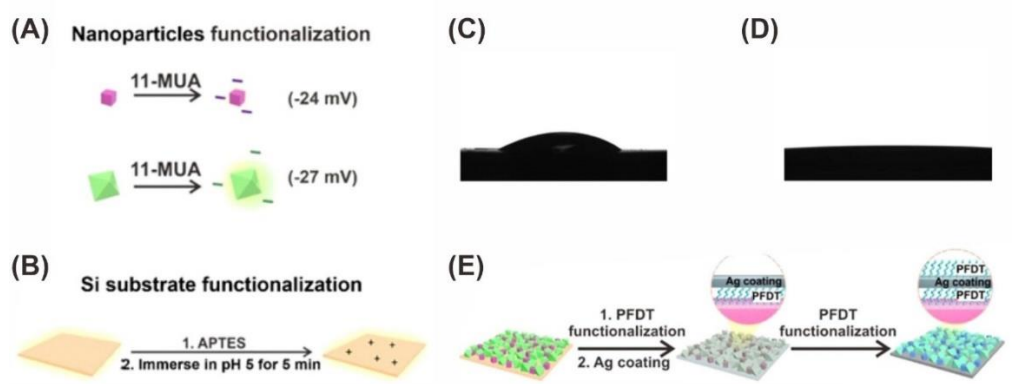

Figure 3-3. Schematic demonstration of (A) nanoparticle surface ligand exchange and (B) Si substrate functionalization. The represented microscopy image of a water droplet on 3-APTES modified Si substrate (A) before and (B) after immersion into pH 5 solution. (E) Schematic demonstrating the fabrication of SPHB SERS platform using nanocubes and octahedra.

This step can successfully remove the 11-MUA from the surface of the Ag nanoparticles to create a clean spectral background for subsequent SERS measurements (Figure 3-4A). Notably, the negatively charged surface functionality of Ag nanoparticles is essential to achieve their successful assembling on Si substrate surface (Figure 3-4B). We eventually coat the Ag nanoparticles array with Ag film (thickness, 25 nm) to maintain their position and surface roughness, followed by functionalizing the surface with perfluorodecanethiol (PFDT) to achieve superhydrophobicity for subsequent static contact angle measurements (Figure 3-4). This adhesive Ag film layer is essential to prevent particle re-dispersion from the substrate surface into the subsequent addition of liquid analyte droplets.[17]

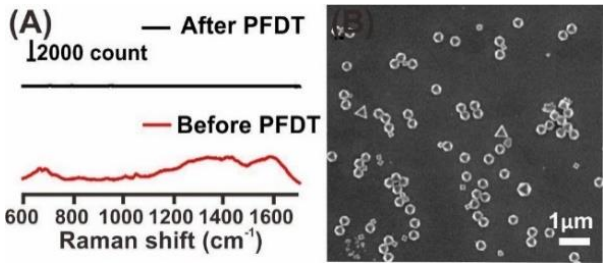

Figure 3-4. Characterization of SPHB and control. (A) SERS spectra of the assembled 2D nanoparticles array before and after ligand exchange with PFDT. PFDT does not have any SERS vibrational peak from 600 onwards. (B) SEM image of the self-assembled Ag nanoparticles in the absence of electrostatic interaction with Si substrate.

The surface hydrophobicity of our as-assembled substrate is essential to concentrate our target liquid analytes for SERS signal enhancement. To optimize the surface hydrophobicity of our platform, we adjust the ratio of the two types of Ag nanoparticles mixture and immersion time during the fabrication process. Briefly, we fabricate a series of substrates by using particle solutions containing varied octahedral-to-nanocubes particle ratio ranging from 1:2 to 4:1, with identical particle density (6×10^8 particles/mL) at different immersion times (Figure 3-5). Firstly, as we increase ratio of octahedra:nanocube from 1:2 to 4:1 at constant immersion time (20 mins), we observe an increase in the static contact angle from $(131 \pm 2)°$ to $(158 \pm 8)°$ (Figure 3-5E) with a sequential increase in particle density on the substrate surface from 2.8 ± 0.22 to 4.4 ± 0.18 particles μm^{-2} (Figure 3-5F). Such increase in particle density is mainly due to the higher octahedra population present on the substrate as the weight of octahedra is heavier than nanocubes, thus resulting the increased contact angle and surface hydrophobicity.

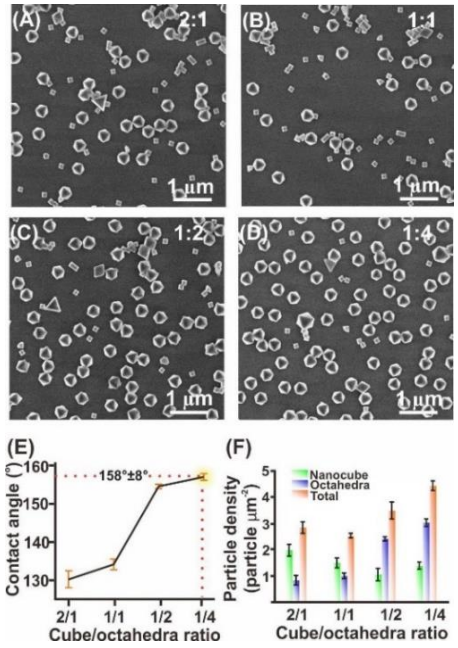

Figure 3-5. SEM images of the binary Ag nanoparticles monolayer fabricated via electrostatic assembly using mixtures of Ag nanoparticles with different Ag nanocubes-to-octahedra concentration ratio of (A) 2:1, (B) 1:1, (C) 1:2, and (D) 1:4. Comparison of (E) static contact angle and (F) particle density of substrate assembled with solely pure Ag nanocubes and Ag octahedra as well as their mixtures at different particle ratios.

Subsequently, we study the effects of immersion time of silicon wafer in Ag nanoparticles mixture on the surface hydrophobicity of assembled 2D array substrate. The immersion time affects the particle density because time is needed for sufficient electrostatic interaction between particles and substrate. We perform a series of experiments with different immersion time ranging from 20 to 100 min with an interval of 20 min at constant octahedral-to-nanocubes partcle ration 4:1 (Figure 3-5). As the immersion time increases from 20 to 60 min, we observe a slight increase in particle density from 4.4 ± 0.18 to 5.1 ± 0.25 particles μm^{-2}. This is mainly arising from the extended immersion time which enable more particles anchoring on the Si substrate via electrostatic interaction. Surprisingly, the surface static contact angle of as-prepared substrate remains almost constant and even slight

decrement as prolonging the immersion time of Si wafer in Ag nanoparticles mixture from 20 to 100 min (Figure 3-6). These results demonstrate that the surface roughness and the corresponding hydrophobicity reaches a maximum with assembling time of 20 mins and beyond 20 mins, additional assembled nanoparticles will tend to form aggregation and multilayer, which likely result in the slight loss of surface roughness (Figure 3-6 D, E).

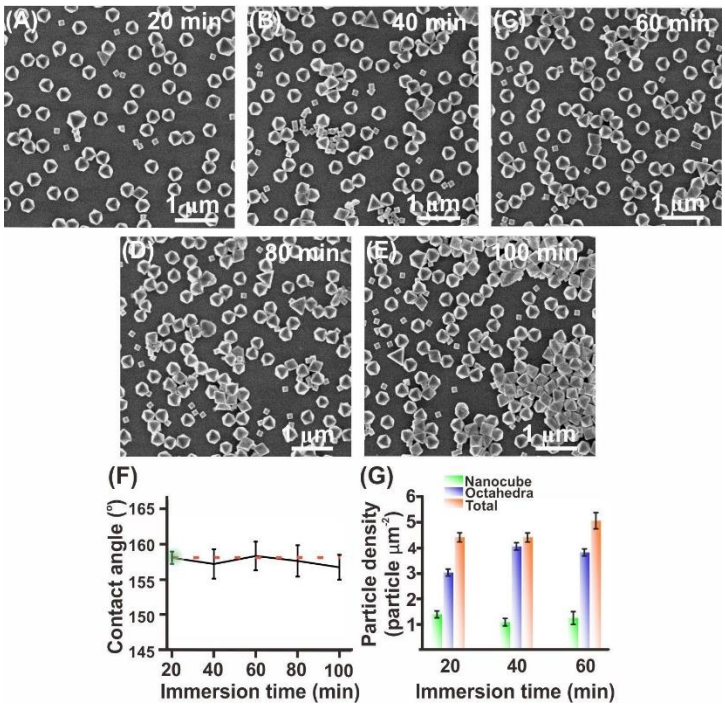

Figure 3-6. Characterization of the binary Ag nanoparticles monolayer fabricated via electrostatic assembly at different immersion times. The SEM image under different immersion time of (A) 20 min, (B) 40 min, (C) 60 min (D) 80 min and (E) 100 min at a nanocubes-to-octahedra ratio of 1:4. (F) Plot of static contact angle over immersion time. (G) Particle density of binary electrostatic assembly under different immersion time.

Thereby, we set our optimized experimental settings with 20 min of Si substrate immersion in Ag nanoparticles mixture (octahedra:nanocubes ratio at 4:1) to fabricate superhydrophobic SERS substrate. The optimized SPHB platform with a particle density of (4.4 ± 0.2) particles μm^{-2} display a static contact angle of (158 ± 8)°. Notably, the SPHB

substrate prepared using a binary mixture of Ag nanoparticles is superior to that prepared using pure Ag nanocubes and Ag octahedral, which display a static contact angle of (96 ± 2)° and (149 ± 6)°, respectively (Figure 3-7A). Correspondingly, our platform exhibits the highest surface roughness of (116 ± 6) nm, which is 1.3- and 1.2-fold higher than the surface roughness of platforms formed using uniform nanocubes or octahedra under identical experimental conditions respectively (Figure 3-7B).

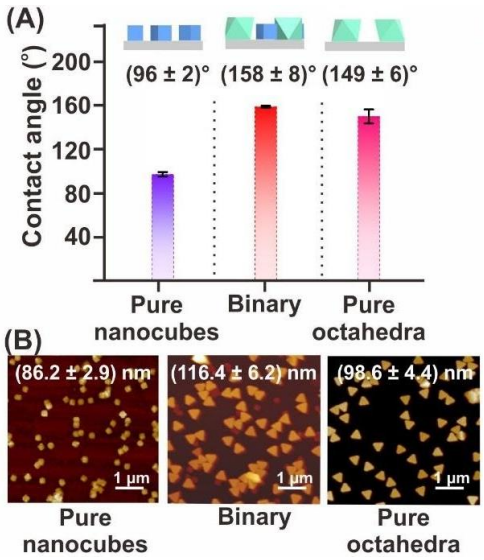

Figure 3-7. (A) Comparison of static contact angles between platform made by pure nanocubes, pure octahedra and their binary mixture. (B) AFM images and corresponding surface roughness of the as-prepared substrates assembled using pure nanocubes, pure octahedra, and their binary mixture.

3.2.2 Evaluation of physical analyte concentrating effect of optimized SPHB

We then evaluate the substrate concentrating performance of our optimized SPHB platform. Firstly, we estimate the physical concentrating factor of our optimized SPHB substrate. We compare the dried surface contact area of a 1 μL silica bead aqueous solution on our SPHB platform with that on a hydrophilic Si substrate (contact angle < 20°). The

contact area of the silica beads on the SPHB platform is estimated to be ~ 0.13 mm^2, 185-fold smaller than the 24 mm^2 spot area on the hydrophilic Si substrate (Figure 3-8).

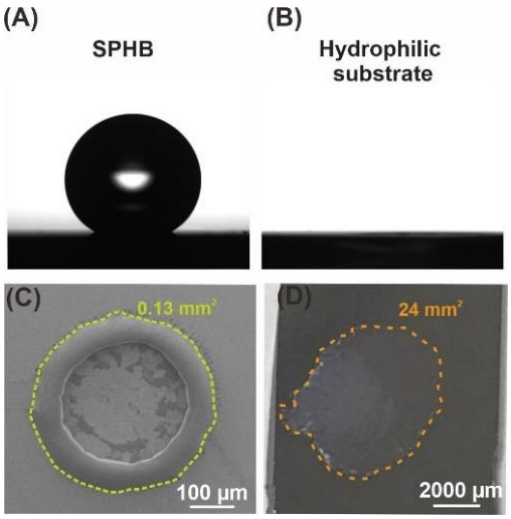

Figure 3-8. Optical images of a static water droplet on (A) superhydrophobic and (B) hydrophilic substrate. The water droplet on hydrophilic substrate will totally spread out and contact angle is close to 0°. (C) SEM image of the effective spot area (yellow circle) of a dried liquid droplet on our superhydrophobic substrate. (D) Digital image of the effective spot area (orange circle) of a dried liquid droplet on a hydrophilic substrate.

These results further indicate effective physical confinement of a liquid droplet into a small contact area on our SPHB platform, which is essential to boost sensitivity towards the subsequent SERS detection of trace metabolites. Secondly, we assess the SPHB-resulted SERS signal enhancing performance from the analyte concentrating effect by comparing the featured SERS peaks from analyte on our SPHB substrate with its hydrophilic substrate counterpart. The hydrophilic 2D Ag nanoparticles array substate in the absence of PFDT functionalization display a static contact angle of (66 ± 8)°, whereas our SPHB substrate in the presence of PFDT modification exhibit a contact angle of (158 ± 8)°. We evaluate their SERS performance by dispensing 1µL of aqueous methylene blue (10^{-4} M) onto both substrate surfaces and measure the SERS signals after the droplets have fully dried. We use the peak intensity of characteristic vibrational features of methylene blue at 1628 cm^{-1},

assigned to C=C stretching, as the benchmark to evaluate the SERS enhancement (Figure 3-9A). The SERS intensity at 1628 cm^{-1} from our SPHB substrate is 10-fold higher than its hydrophilic susbtrate counterpart (Figure 3-9B). This result demonstrates that the hydrophobicity of our SPHB can provide ~10-fold enhancement on the SERS signal, as a result of minimized solid-liquid contract area to concentrate the analyte, thus increasing the analyte-to-signal ratio to improve the detection sensitivity.

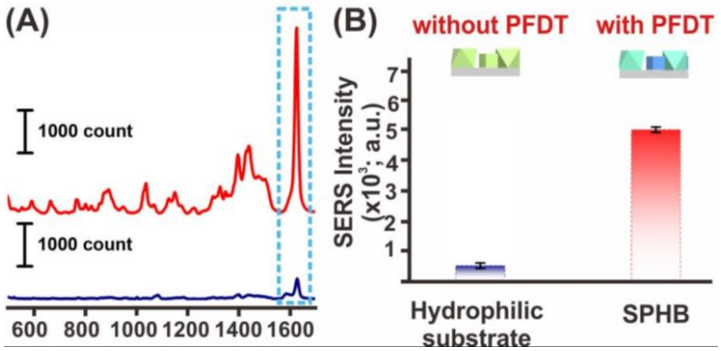

Figure 3-9. Evaluating SERS signal enhancement on superhydrophobic substrate and its hydrophilic substrate counterpart, using methylene blue as probe molecule. (A) SERS spectra of 10^{-4} M methylene blue droplet on superhydrophobic substrate (red) and hydrophilic substrate (blue). (B) SERS intensity corresponding to peak at 1628 cm^{-1} of methylene blue on superhydrophobic substrate (red) and hydrophilic substrate (blue).

3.2.3 Elucidation of SERS enhancement of Optimized SPHB SERS substrate

To further investigate the SERS enhancement and elucidate the enhancing mechanism of our SPHB platform, we systematically study the analytical SERS enhancement factor (AEF) of a series of platforms. AEFs are quantified using the equation: $AEF = [(I_{SERS})/(I_{Raman})] \times [(C_{Raman})/(C_{SERS})]$, where I_{SERS} and I_{Raman} are the signals recorded on SERS and normal Raman platforms, whereas C_{SERS} and C_{Raman} are the corresponding analyte concentrations measured using superhydrophobic platform and normal Raman platforms, respectively. The AEF evaluation of substrate is essential to compare and explore

the SERS enhancing performance of relevant platforms. Firstly, we estimate the AEF of our Ag-layer coated binary Ag particles-based SPHB SERS substrate, as compared to silica bead-based SPHB substrate (Figure 3-10A and B). Both substrates are superhydrophobic. Typically, we drop cast 10 µL of MB solution at different concentrations on both substrates surface and measure the SERS signal. For the normal Raman measurements, we drop cast 10 µL of MB solution (10^{-3} M) on the non-SERS active Si wafer substrate surface. We evaluate the signal enhancement using peak intensity from the featured C=C vibrational mode of methylene blue at 1628 cm^{-1}.[20] Notably, the AEF of our superhydrophobic binary SERS substrate is estimated to be 2.4×10^9, whereas non-plasmonic active silica beads array is only 5×10^2 (Figure 3-10D and E). We acknowledge that the SERS enhancement of the silica bead-based substrate (5×10^2) may arise from the Ag layer coating and the superhydrophobicity of the substrate to concentrate the analyte into small area. By comparing these two substrates, we minimize the potential differences arising from the concentrating effect from SPHB surface. Hence, the additional 4.8×10^6-fold enhancement in our SPHB SERS substrates is mainly attributed to the presence of hot spots on and between the Ag nanocubes and octahedra.[16, 21] This result shows the importance of the well-defined nanocube and octahedra as building block for the fabrication SPHB SERS platform.

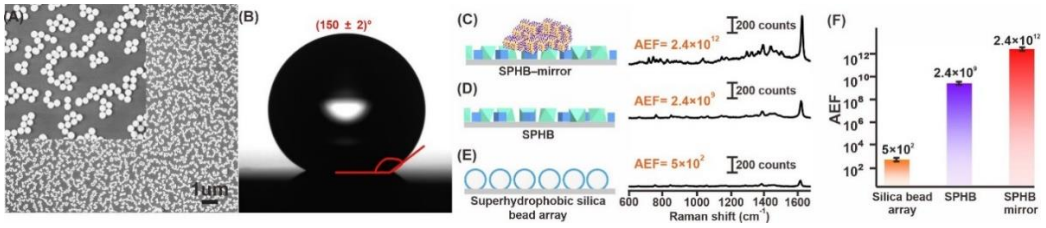

Figure 3-10. The analytical enhancement factors (AEF) study. (A) SEM image and (B) static contact angle of silica bead array. Schematic illustration and corresponding AEF of (C) binary superhydrophobic substrate-mirror (SPHB-mirror) substrate, (D) SPHB substrate, and (E) superhydrophobic silica bead array. AEF is calculated using methylene

blue as the analyte, based on the C=C vibrational mode at 1628 cm^{-1}. (F) Comparison of AEFs between SPHB-mirror, SPHB, and silica bead array, to elucidate the relative contribution of analyte concentration effects and electromagnetic field enhancements to the overall AEF on our SERS platform. Error bars in (F) are s.d. of 25 measurements.

To further boost the AEF of our platform for ultrasensitive metabolite detection, we introduce SERS-active Ag nanocubes colloidal particles into the analyte detection. Typically, we mix the analytes with a dispersion of Ag nanocubes with fixed concentration, and subsequently drop cast the mixture onto the SPHB platform. This approach greatly boosts the AEF of our SPHB substrate by 10^3-fold, with a detection limit down to 10^{-14} M and an analytical dynamic range from 10^{-4} to 10^{-14} M (Figure 3-10C and F). We attribute such distinct signal enhancement to two additional effects. Firstly, the introduction of Ag nanocubes significantly increases hotspot densities and enables more analytes trapped among adjacent Ag nanocubes upon droplet drying. Secondly, the introduction of the analyte-Ag nanocubes dispersion to the SPHB platform creates a "mirror effect" between the additional nanocubes and the SPHB SERS-active surface.[22-24] Furthermore, our platform exhibits highly consistent SERS intensities property. SERS spectra extracted across a hyperspectral SERS map of a dried droplet demonstrate similar spectral features, with good signal reproducibility and homogeneity (relative standard deviation of 4.5%; Figure 3-11A, B). As such, our subsequent experiments will be conducted using this "SPHB-mirror" modality to achieve efficient physical concentration of analyte near abundant SERS-active regions.

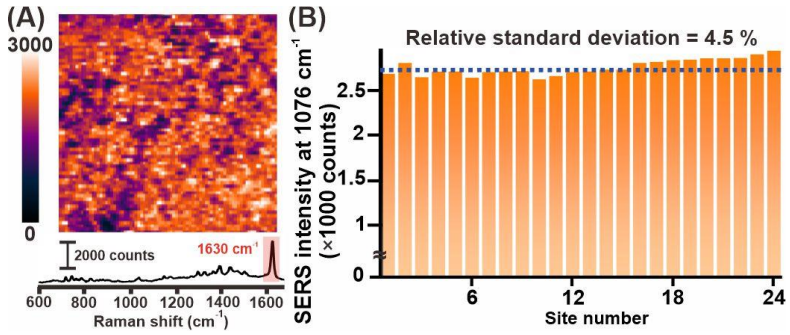

Figure 3-11. (A) Hyperspectral SERS intensity distribution map of one featured C=C vibrational mode of methylene blue (1628 cm^{-1}) using our SPHB platform, which demonstrates a good signal reproducibility and homogeneity of the platform. (B) Homogeneous intensity profile of the methylene blue peak at 1630 cm^{-1} on the SPHB substrate.

3.2.4 Specific analyte capture regulated by nanoscale surface chemical functionality

Apart from the efficient physical enrichment of analytes, specific capture of target analytes onto plasmonic Ag nanoparticle surfaces is essential to generate target-specific SERS fingerprints for their accurate identification and differentiation with other interferences. Our targets urine metabolites are pregnane and THC, which possess intrinsically low Raman cross section and weak affinity with Ag surface. Notably, they are reported to be miscarriage-relevant urinary metabolites, and can be used to predict the risk of miscarriage. To boost their SERS response, we introduce 4-mercaptophenylboronic acid (MPBA) as a capturing agent which possess two distinct chemical functionalities (Figure 3-12A). The thiol functional group allows MPBA to form a self-assembled monolayer on Ag nanocubes surfaces through specific metal-sulfur interactions, whereas the boronic acid functionality enables specific interaction with our analytes by forming boronate ester bond under alkaline conditions.[25-31] This chemical interaction localizes the metabolites near the plasmonic nanoparticle surfaces to result in maximum SERS enhancement.[32, 33] In brief, we

premix the MPBA-functionalized Ag nanocubes with aqueous pregnane or THC (10^{-4} M) for full interaction followed by drop casting 10 µL of mixture droplet onto SPHB substrate for SERS measurements. The SERS spectrum of neat MPBA-grafted nanocubes exhibit two characteristic vibrational modes at 1181 and 1328 cm^{-1} (Figure 3-12B and 3-13i).[27] In the presence of THC, the 1328 cm^{-1} band intensity decreases sharply with a concomitant blue-shift to ~1332 cm^{-1} (Figure 3-13i). Two new peaks are also observed at 1169 and 1173 cm^{-1} near the peak at 1181 cm^{-1}. Similarly, in the presence of pregnane, we note an intensity decrease and blue-shift of 1328 cm^{-1} band to ~1333 cm^{-1} and emergence of two new peaks at 1170 and 1190 cm^{-1}. These spectral changes in vibrational fingerprints before and after interaction with the metabolites are direct evidence of the interaction between the metabolites and MPBA-functionalized nanocubes.

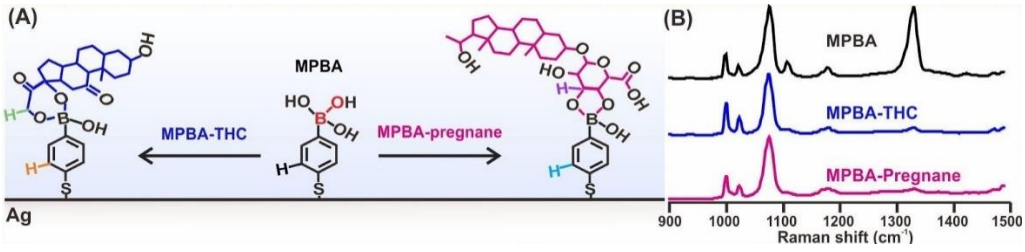

Figure 3-12. (A) Interaction of MPBA with pregnane and THC on the Ag nanocubes' surface. (B) SERS spectra of MPBA, MPBA-THC and MPBA-pregnane.

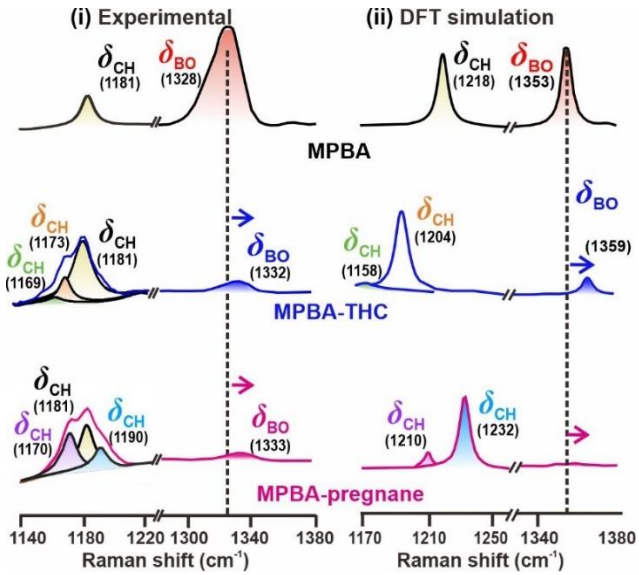

Figure 3-13. (A) Key spectral changes involving boronate ester moiety at 1140 to 1380 cm^{-1} in the presence of pregnane and THC. (i) Experimental measured SERS spectra and (ii) DFT simulated SERS spectra of MPBA, MPBA-pregnane and MPBA-THC.

To elucidate the molecular origin of the observed spectral changes, we employ density functional theory (DFT) to simulate the SERS spectra of MPBA and that of MPBA bound individually to pregnane and THC, (Figure 3-13ii), respectively. Our model comprises a MPBA molecule on the apex of a Ag6 cluster (Ag-MPBA). The distinct vibrational modes of MPBA at 1181 and 1328 cm^{-1} are indexed to C-H bending from benzene ring (δCH) and bending mode of boronic acid (δBO), respectively.[34, 35] We then place the metabolites separately near Ag-MPBA, and allow the system to relax to form the complex structure. For MBPA-THC, the C-H vibration mode shift from 1218 cm^{-1} to a lower position at 1204 cm^{-1} and 1158 cm^{-1}, whereas for MBPA-pregnane, the C-H vibration mode shift from 1218 cm^{-1} toward higher wavenumbers at 1232 cm^{-1} and another new C-H mode appear at lower position at 1210 cm^{-1}. Notably, in our experiments, the Ag surface grafted MBPA molecules are not fully reacted with the metabolites, thus the experimental spectrum is expected to arise from a mixed spectrum of unreacted MPBA and those reacted with

metabolites. In both cases, the chemical interactions of THC and pregnane with MPBA lead to a significant decrease in peak intensity of the δBO bending at ~1328 cm^{-1}, and a concomitant blue shift. The formation of the boronate ester bond restricts B-O bond vibration and reduces the bond polarizability, thereby resulting in a higher energy requirement for B-O bond vibration. In the presence of THC, the experimentally observed SERS peaks at 1169 and 1173 cm^{-1} can be indexed to C-H bending mode (δCH) in the boronate ester moiety (Table 3-1). Similarly, for pregnane-MPBA, C-H bending mode is also observed at 1170 and 1190 cm^{-1} in the experimental spectra.[27, 34] Collectively, these results affirm the strong chemical interaction of MPBA with both pregnane and THC, enabling the potential SERS quantification of these metabolites.

Table 3-1. SERS vibrational modes and band assignments of MPBA, MPBA-THC and MPBA-pregnane, respectively.

	Experimental (cm^{-1})	Simulated (cm^{-1})	Vibration mode
MPBA	1181	1218	δ_{CH}
	1328	1353	δ_{BO}
MPBA-THC	1169	1158	δ_{CH}
	1173	1024	δ_{CH}
	1332	1359	δ_{BO}
MPBA-Pregnane	1170	1210	δ_{CH}
	1190	1232	δ_{CH}
	1333	-	

δ, bending

3.2.5 Applying chemometrics for rapid multiplex identification and quantification

Speedy and accurate metabolite identification and quantification of multiplex metabolite biomarkers is significant for the development of SERS based diagnostic kits towards relevant disease diagnosis. To achieve this goal, we apply advanced chemometrics analysis to process our data to generate reliable and accurate quantified readouts, as compared to traditional manual analysis.

Firstly, we employ principal component analysis (PCA) to process our SERS fingerprint information, which allows extraction of key information across the entire spectral range measured while simultaneously eliminating noise and reducing human errors.[36] We apply standard normal variate correction and Savitzky-Golay derivative algorithm as data pretreatment to a total of 75 SERS spectra corresponding to MPBA, MPBA-THC, and MPBA-pregnane, respectively, prior to the unsupervised clustering process. These spectra are individually collected under the same experimental conditions using a laser beam with an excitation wavelength of 532 nm and laser power of 0.2 mW with spectral acquisition time of 1s. 25 SERS spectra from each group, corresponding to a total of 75 spectra, are selected randomly without any specific criteria for analysis since our platform exhibit good signal homogeneity. These 75 SERS spectra are loaded without any background correction, using a total of 6 loading vectors for PCA analysis. For PCA score plotting, PC1 and PC2 account for a respective 81.89 % and 15.18 % of the variance in the SERS spectra analysed. Hence, the sum of PC1 and PC2, *i.e.* 97.07% indicates that almost all the variances observed in the SERS spectra can be accounted for. The output data along PC1 demonstrates three distinct clusters, each corresponding to MPBA, MPBA-pregnane and MPBA-THC, indicating that they can be differentiated unambiguously (Figure 3-14A). We further demonstrate the capability to distinguish the metabolites' SERS signals from the SERS signals of common sugars such as glucose and fructose (Figure 3-14B and C). These sugars are possible interferences that could be present in various biofluids, and they interact

similarly with MPBA. Our results thus highlight how integrating PCA with our 'confine-and-capture' strategy can effectively extract relevant SERS spectral variations with high specificity.

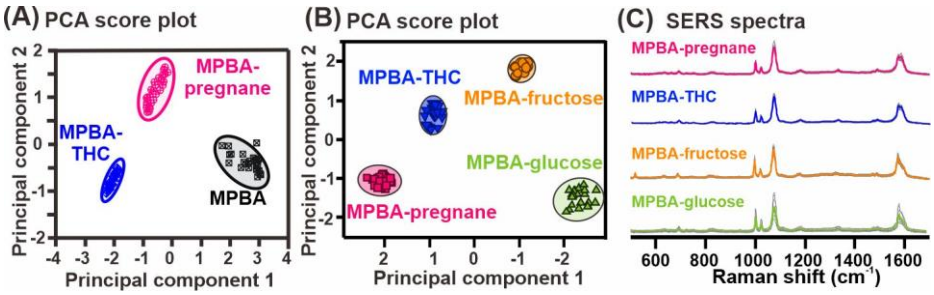

Figure 3-14. (A) PCA plot of MPBA-pregnane, MPBA-THC, and MPBA with 95% confidence ellipses. (B) Controlled experiment of 4-MPBA with pregnane, THC, fructose and glucose. The PCA result shows that 4-MPBA molecules have high specificity for pregnane and THC molecules. (C) Representative SERS spectra of MPBA bonded pregnane, THC, fructose and glucose. SERS spectrum of MPBA bonded.

Next, we employ partial least square regression (PLS) to establish a standard calibration curve for our metabolites and to predict the analyte concentrations by computing 210 SERS spectra from 10^{-4} M to 10^{-10} M (Figure 3-15).[34] PLS regression plots the experimental metabolite concentration on the x-axis and the predicted metabolite concentration on the y-axis. Our calibration curve shows a near-ideal linearity spanning 7 orders of magnitude, with linear coefficients of 0.995 and 0.994 for MPBA-pregnane and MPBA-THC, respectively (Figure 3-15C, 15D). For multiplex SERS measurements for various pregnane%, samples containing pregnane% between 90 – 100 % were first prepared by mixing pure pregnane and THC with corresponding volume ratios. This can help us to simulate the real detection scenario according to a previous study which found that the pregane:THC ratio differ for threatened miscarriage patients (<97.4%) and on-going pregnancy (>98.7%). The PLS prediction model shows a highly linear coefficient of 0.985

within 90-100%. Hence, PLS can construct a good prediction model based on concentration-dependent changes across the entire experimentally measured spectral window, notably within a very short time frame (< 5 min). This statistically robust model is certainly unachievable through manual data analyses, where the signal intensities of specific fingerprints at different concentrations are individually collated and could easily be subject to human errors.

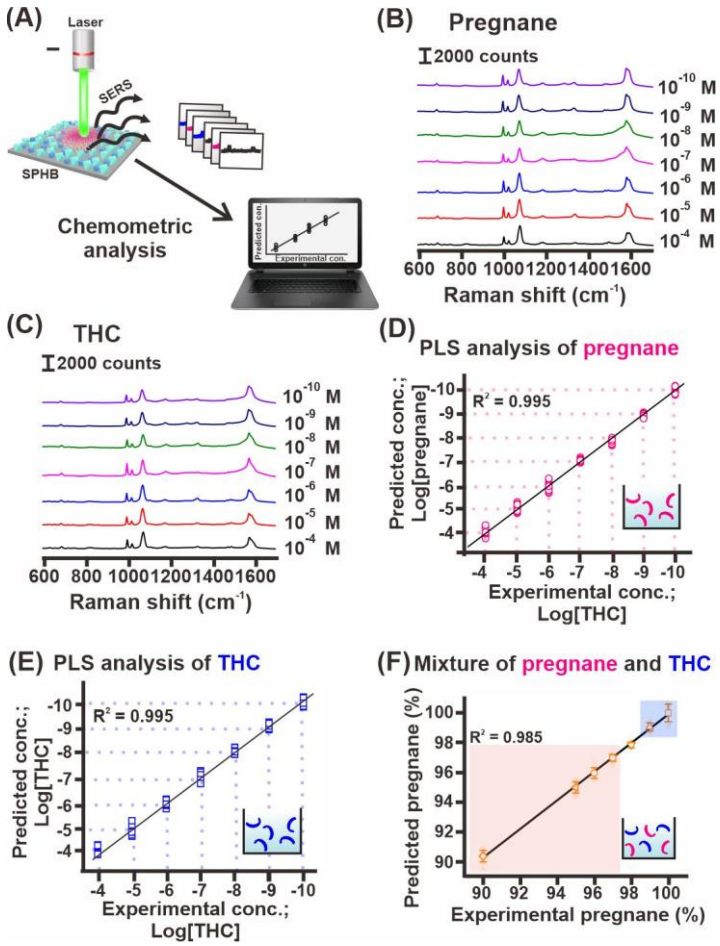

Figure 3-15. Partial least square analysis. (A) s(B) Pregnane and (C) THC at different concentrations ranging from 10^{-4} M to 10^{-10} M. (D)-(E) PLS analyses of concentration-dependent SERS spectra of pregnane and THC from 10^{-4} M to 10^{-10} M, respectively. (F) PLS analysis of a mixture comprising pregnane and THC with different pregnane%. Ongoing pregnancy and miscarriage regions are highlighted in blue and pink, respectively.

3.3 Conclusion

In conclusion, we have successfully fabricated a proof-of-concept diagnostic kit for spontaneous miscarriage based on multiplex urine metabolite detection by integrating a superhydrophobic SERS substrate with mirror effect. This integrated platform is employed to analyse pregnane and THC urinary metabolites which are found during pregnancy. PCA and PLS analysis are able to extract key vibrational information from our SERS spectra to diagnose the spontaneous miscarriage. Notably, the detection limit can reach 10^{-9} M for both of the analyte and the multiplex detection be achieved in the artificial medium which can be further extended for spontaneous miscarriage detection. Hence, together with the insights gained from our studies, we envisage to extrapolate this platform for the SERS detection from the real urine sample from patients.

3.4 Material and methods

Chemicals. Silver nitrate ($AgNO_3$, ≥ 99%), anhydrous 1,5-pentanediol (PD, ≥ 97%), poly(vinylpyrrolidone) (PVP, average MW = 55000 g/mol), toluene (99.5%), 11-mercaptoundecanoic acid (MUA, 95%), 4-mercaptoboronic acid (MPBA, 90%), ammonia (28-30%), 1H,1H,2H,2H-perfluorodecanethiol (PFDT, 97+%), sodium chloride (NaCl, 99.5%), monopotassium phosphate (KH_2PO_4, 99%), glucose ($C_6H_{12}O_6$, ≥ 99.5%), fructose ($C_6H_{12}O_6$, ≥ 99%), and sodium phosphate (Na_3PO_4, 96%), were purchased from Sigma Aldrich; copper (II) chloride ($CuCl_2$, ≥ 98%), 3-aminopropyltriethoxysilane (APTES, 98%) were from Alfa Aesar; ethanol (ACS, ISO, Reag. Ph Eur) was from EMSURE; hydrochloric acid (HCl, 37%) was purchased from Analar Normapur. Tetrahydrocortisone (THC) was purchased from Scientific Resources. 5β-pregnane-3α,20α-diol-3α-glucuronide (pregnane) was purchased from AXIL Scientific PTE LTD. All chemicals were used without further

purification. Milli-Q water (>18.0 MΩ.cm) was purified with a Sartorius Arium 611 UV ultrapure water system.

Synthesis and purification of shape-controlled Ag polyhedral. The preparation process was carried out according to the polyol reduction method,[48] starting first with the synthesis of Ag nanocubes (AgNC). 20 mL PD was added to a 100 mL round bottom flask and heated to 190 ˚C for 10 minutes. Aliquots of 250 μL PVP and 500 μL AgNO3 precursor solutions were then alternately added to the reaction flask. This process was continued until the reaction mixture turned reddish brown. For the subsequent growth of Ag octahedra (AgNO), this solution was used without further treatment, using more concentrated precursor solutions. The reaction was allowed to proceed for ~2 h. The Ag polyhedra solutions were re-dispersed in 20 mL ethanol *via* multiple centrifugations rounds and purified through vacuum-filtration.

Ligand exchange reactions for Ag polyhedral. Ag polyhedra were separately functionalized with 11-MUA and MPBA through standard ligand exchange reactions. For 11-MUA functionalized Ag nanocubes (AgNCs), 1 mL ethanol was added to AgNC in ethanol suspension (0.1 mL, 2 mg mL^{-1}) and the supernatant was discharged after centrifugation. The AgNC were then re-dispersed in 1.5 mL of mixture of isopropyl alcohol (IPA) and ethanol with volume ratio of 1:1 under stirring speed of 500 rpm at 25 ˚C. Subsequently, 0.05 mL 11-mercaptoundecanoic acid (11-MUA) in IPA solution (0.1 mM) was added into the AgNC dispersion. The reaction mixture was then left for 4 hours at ambient condition and the supernatant was removed after centrifugation at 6500 rpm for 4.5 minutes. The same ligand replacement process was repeated once more. The AgNC colloidal suspension was then washed with copious amount of IPA and ethanol to remove

excess 11-MUA. Finally, the AgNC were re-dispersed in 1.5 mL mixture of IPA and ethanol (volume ratio, 1:1) and stored under nitrogen gas protection for further use. Zeta potential measurement was then carried out to measure the surface charges of AgNC. Similarly, the ligand exchange process was performed for AgNO colloidal solutions (0.1 mL, 13.7 mg/mL), using a solution of 11-MUA (0.1 mL, 10 mM) in IPA. Zeta potential measurements were then conducted using ZETASIZER NANO with DTS1070 folded capillary cell to measure the surface charges of the MUA functionalized Ag polyhedra.

For MPBA functionalized Ag nanocubes, 1 mL ethanol was added to AgNC in ethanol suspension (0.1 mL, 2 mg/mL) and the supernatant was discharged after centrifugation. The AgNC were then re-dispersed in 1.5 mL of mixture of isopropyl alcohol (IPA) and ethanol with volume ratio of 1:1 under stirring speed of 500 rpm at 25 ^{o}C. Subsequently, 0.05 mL MPBA in IPA solution (0.1 mM) was added into the AgNC dispersion. The reaction mixture was then left for 4 hours at ambient condition and the supernatant was removed after centrifugation at 6500 rpm for 4.5 minutes. The process was repeated once more, before repeating the same ligand reaction for a further 3 hours. The resulting solution was centrifuged, and supernatant was removed. The AgNC was then dispersed in 1.5 mL of IPA/ethanol (1:1, v/v), sonicated and centrifuged. The process was repeated twice, and the resulting product will be re-dispersed in 1 mL mixture of ethanol.

Surface functionalization of silicon wafer. Si wafer (1.5 cm × 1.5 cm) was subjected to oxygen plasma treatment for 5 minutes and then submerged in an anhydrous toluene solution containing 3-aminopropyltriethoxysilane (2 % in volume) for another 5 minutes. Subsequently, the amine-terminated Si wafer was rinsed with anhydrous toluene and methanol, followed by blow drying with N2 gas to remove any unfunctionalized ligands and solvents. The functionalized Si wafer was then submerged in an acid solution (pH= 5)

for 5 minutes for further protonation of the amine-terminated wafer surface and render its surface positively-charged. The resulting platforms were kept in a nitrogen environment for further use.

Fabrication of binary superhydrophobic SERS chip. The binary superhydrophobic chip was fabricated by firstly submerging the positively charged Si substrates into 2 mL of 11-MUA functionalized Ag nanocubes and octahedra mixture solution for 20 minutes. The surface negatively charged Ag polyherdrals anchored on Si substrates surface *via* static interaction. The Ag polyhedral anchored Si substrates were then removed from the colloidal solution, rinsed with copious ethanol, and dried under nitrogen gas blowing. Such Si substrates were then coated with Ag layer (thickness of 25 nm) *via* thermal evaporation followed by functionalization with PFDT *via* immersing the Ag-layer coated Ag polyhedral anchored Si substrates in 0.05 M PFDT ethanolic solution for overnight. The substrates were removed from the PFDT solution and rinsed with copious ethanol, and dried using nitrogen gas. The as-prepared substrates were finally storied in nitrogen box for further use.

Fabrication of superhydrophobic silica bead array. The superhydrophobic silica bead array was fabricated by firstly submerging the Si wafer into silica bead (size, 103 nm) colloidal solution for 0.5hrs. The Si wafer was then removed from the colloidal solution and dried under blowing with nitrogen gas. Such silica bead deposited Si wafer were then coated with 25 nm Ag layer *via* thermal evaporation followed by functionalization with PFDT using the same method as above mentioned.

Contact angle measurements. Static contact angles were measured by drop casting a sessile droplet of 4 µL water droplet onto the platform. All contact angle measurements were repeated at least 5 times at different locations of the substrates.

Hyperspectral SERS intensity distribution map. The SERS spectra was collected by using a laser beam with an excitation wavelength of 532 nm and laser power of 0.2 mW with spectral acquisition time of 1 s. The standard deviation of the measured SERS signal in 200 µm × 200 µm (area of the SERS map) is estimated to be 4.5 %, indicating the good homogeneity and reproducibility.

Analyte concentrating effect. Silica beads were used to determine the analyte concentrating effect and were synthesized using a modified Stober process.[49] 1 µL silica beads suspension was deposited onto a superhydrophobic platform and O_2 plasma treatment (hydrophilic) platform and allowed to dry. The area of dried spots was then characterized through digital camera and SEM. The spot areas on both superhydrophobic and hydrophilic surfaces were measured using ImageJ software.

Determining analytical enhancement factors (AEFs). AEFs were quantified using $AEF = [(I_{SERS})/(I_{Raman})] \times [(C_{Raman})/(C_{SERS})]$, where I_{SERS} and I_{Raman} were the signals recorded on SERS and normal Raman platforms, whereas C_{SERS} and C_{Raman} are the corresponding analyte concentrations measured using superhydrophobic platform and normal Raman platforms, respectively. We conduct this experiment by using 10 µL of MB solution at different concentration. For the normal Raman measurements, we drop cast a 10 µL of MB solution with concentration of 10^{-3} M on the Si wafer substrate. For the superhydrophobic-mirror substrate, the lowest detectable concentration of MB is 10^{-14} M. All the SERS spectra

in current work are collected under dry conditions after the solvent in the droplet has fully evaporated, and the analytical enhancement factor was calculated on the basis of the intensities of the vibrational band of methylene blue at 1628 cm^{-1} of 25 spectra.

Density functional theory (DFT) simulation. The calculation on the interaction of MPBA-grafted Ag surface with pregnane and THC were carried out using the unrestricted B3LYP exchange-correlation functional in the Gaussian 09 computational chemistry package. The 6-31g (d p) basis set was used for C, H and O. The LANL2DZ basis set was employed for Ag. The Ag surface was modeled using a reported triangle consisting of 6 Ag atoms. First, we optimize the geometry of the triangular Ag cluster, then 4-mercaptophenylboronic acid was placed on its vertex and the whole system was then relaxed with all the Ag atoms. Pregnane/THC molecule was then forming a boric ester bond with MPBA *via* hydroxy group, and the whole system was relaxed with Ag atoms fixed again.

SERS measurements for pregnane and THC. For SERS measurements of pure analytes, 10 μL of pregnane or THC solution (10^{-4} – 10^{-9} M) were respectively mixed with MPBA-functionalized AgNC (~ 0.2 mg mL^{-1}) at pH 11 for reaction. 10 μL-mixture solution was then placed on the superhydrophobic chip surface and then dried under ambient conditions. SERS spectra were then collected on the dried spot using a laser beam with an excitation wavelength of 532 nm and laser power of 0.2 mW with spectral acquisition time of 1 s.

For SERS measurements of the mixed analytes with varied pregane% (90-100%), we firstly prepared the samples by mixing pure pregnane and THC solution (0.1 mM) with varied volumes. Typically, sample containing 90 % pregnane (10 % THC) were prepared by mixing of 90 μL-pregnane (0.1 nM) with 10 μL-THC (0.1 nM) solution. Subsequently, 10 μL of the samples that contain varied pregnane% were mixed with MPBA-functionalized

AgNC (~ 0.2 mg mL-1) at pH 11 for reaction. The 10 µL-mixture sample solution was then introduced on the superhydrophobic chip surface and then dried under ambient conditions. SERS spectra were then collected on the dried spot area using a laser beam with the same conditions as above.

Control experiments for glucose and fructose. For SERS measurements of control samples, 10 µL of glucose and fructose (10^{-4} M) were firstly mixed with MPBA-functionalized AgNC (~ 0.2 mg mL^{-1}) at pH 11 for reaction, respectively. The 10 µL-mixture was then placed on the superhydrophobic chip surface and then dried under ambient conditions. SERS spectra were then collected using a laser beam with an excitation wavelength of 532 nm and laser power of 0.2 mW with spectral acquisition time of 1 s.

Chemometric analyses. Principal component analysis (PCA) was conducted using Panorama software ((LabCognition, Analytical Software GmbH & Co. KG; minimum of 25 spectra of each sample are collected from the single droplet). PCA reduces data dimensionality and converts the original variables into a set of uncorrelated linear combination of principal components (PC); PC1 typically includes the greatest variance from the orthogonal linear transformation, and PC2 includes the second greatest variance. 25 individual raw SERS spectra from 3 groups, MPBA and those coordinated with pregnane and THC respectively (total of 75 spectra), were loaded together into the Panorama software. Standard normal variate correction and Savitzky-Golay derivative algorithm were applied to reduce spectral noise and eliminate interference from the background signals. The entire spectral range measured experimentally was selected for analysis, and a suitable number of loading vectors were employed to provide the minimum root-mean-square error for cross validation (RMSECV). In our experiment, we selected the whole spectral range with two PCs applied, which enabled spectral identification with accuracy of at least 98 %.

A similar clustering process was applied for two patient urine samples, one with spontaneous miscarriage (M1) and another with ongoing stable pregnancy (S1). Partial least square analysis (PLS) was used to establish a standard calibration curve for detection in multiple scenarios, including pure analytes, multiplexed pure analytes, and multiplexed analytes in artificial urine, as well as analytes in real patient urine samples. For detection using pure analytes, 25 spectra were input for each concentration measured. For other cases, quantification model was built up by PLS using spectra collected from 90%-100% of pregnane spiked in artificial urine and patient urine samples, respectively.

Characterization. Scanning electron microscope (SEM) imaging was performed using a JEOL-JSM-7600F microscope at an accelerating voltage of 5 kV. UV-vis spectroscopic measurements were performed with a Cary 60 UV-Vis spectrometer. Zeta potential measurements were conducted using ZETASIZER NANO with DTS1070 folded capillary cell. Thermal evaporation of Ag was performed using Syskey thermal evaporator (Taiwan). Roughness of the sample was measured using JPK Nanowizard3 BioScience atomic force microscopy (AFM) on a Zeiss inverted microscope. Contact angles were measured using a Theta Lite tensiometer equipped with a Firewire digital camera and Attention from Biolin Scientific with sessile 4 μL ultrapure water droplet. Advancing and receding contact angles were determined using drop shape analysis routine of a growing and shrinking water droplet. Each type of contact angle measurement was performed at least five times across each platform to obtain an average wetting angle. x-y SERS measurements were performed with Raman touch microspectrometer (Nanophoton Inc, Osaka, Japan) at an excitation laser wavelength of 532 nm (power = 0.2 mW). A 20 × (N.A., 0.45) objective lens with 1 s accumulation time was used for data collection with Raman shift ranging from 500 cm^{-1} to

1600 cm^{-1}. All SERS spectra were obtained by averaging at least 25 individual spectra per Raman image.

References

1. Otto, A., *J. Raman Spectrosc.* **2002,** *33*, 598.
2. Kambhampati, P.; Child, C. M.; Foster, M. C.; Campion, A., *J. Chem. Phys.* **1998,** *108*, 5026.
3. Jeanmaire, D. L.; Van Duyne, R. P. *J. Electroanal. Chem.* **1977,** *84*, 20.
4. Chan, G. H.; Zhao, J.; Hicks, E. M.; Schatz, G. C.; Van Duyne, R. P. *Nano Lett.* **2007,** *7*, 1952.
5. Gao, C.; Hu, Y.; Wang, M.; Chi, M.; Yin, Y., *J. Am. Chem. Soc.* **2014,** *136*, 7479.
6. Cortie, M. B.; McDonagh, A. M., *Chem. Rev.* **2011,** *111*, 3735.
7. Su, J.; Wang, D,; Nörbel , L.; Shen, J.; Zhao, Z.; Dou, Y.; Peng, T.; Shi, J.; Mathur, S.; Fan, C.; Song, S. *Anal. Chem.* **2017,** *89*, 2538.
8. Zong, C.; Wu, J.; Liu, M.; Yan, F.; Ju, H. *Chem. Sci.* **2015,** *6*, 2607.
9. Xu, L.; Yan, W.; Ma, W.; Kuang, H.; Wu, X.; Liu, L.; Zhao, Y.; Wang, L.; Xu, C. *Adv. Mater.* **2015,** *27*, 1711.
10. Laing, S.; Gracie, K.; Faulds, K. *Chem. Soc. Rev.* **2016,** *45*, 1918.
11. Kole, P. L.; Venkatesh, G.; Kotecha, J.; Sheshala, R. *Biomed. Chromatogr.* **2011,** *25*, 217.
12. Chang, M. S.; Ji, Q.; Zhang, J.; El-Shourbagy, T. A. *Drug Dev. Res.* **2007,** *68*, 133.
13. Price, C. P., *BMJ* **2001,** *322*, 1288.
14. Gubala, V.; Harris, L. F.; Ricco, A. J.; Tan, M. X.; Williams, D. E. *Anal. Chem.* **2012,** *84*, 515.
15. Jehlička, J.; Edwards, H. G. M.; Vítek, P. *Planet. Space Sci.* **2009,** *57*, 613.

16. Yashchenok, A.; Masic, A.; Gorin, D.; Shim, B. S.; Kotov, N. A.; Fratzl, P.; Möhwald, H.; Skirtach, A. *Small* **2013,** *9*, 356.
17. Lee, H. K.; Lee, Y. H.; Zhang, Q.; Phang, I. Y.; Tan, J. M. R.; Cui, Y.; Ling, X. Y. *ACS Appl. Mater. Interfaces* **2013,** *5*, 11418.
18. Gentile, F.; Coluccio, M. L.; Coppedè, N.; Mecarini, F.; Das, G.; Liberale, C.; Tirinato, L.; Leoncini, M.; Perozziello, G.; Candeloro, P.; De Angelis, F.; Di Fabrizio, E. *ACS Appl. Mater. Interfaces* **2012,** *4*, 3224.
19. Lee, H. K.; Lee, Y. H.; Koh, C. S. L.; Phan-Quang, G. C.; Han, X.; Lay, C. L.; Sim, H. Y. F.; Kao, Y.-C.; An, Q.; Ling, X. Y., *Chem. Soc. Rev.* **2019,** *48*, 756.
20. Le Ru, E. C.; Blackie, E.; Meyer, M.; Etchegoin, P. G. *J. Phys. Chem. C* **2007,** *111*, 13803.
21. Knoll, W., *Annu. Rev. Phys. Chem.* **1998,** *49*, 638.
22. Hu, J.; Tanabe, M.; Sato, J.; Uosaki, K.; Ikeda, K. *J. Am. Chem. Soc.* **2014,** *136*, 10307.
23. Benz, F.; Chikkaraddy, R.; Salmon, A.; Ohadi, H.; de Nijs, B.; Mertens, J.; Carnegie, C.; Bowman, R. W.; Baumberg, J. J. *J. Phys. Chem. Lett.* **2016**, *7*, 2269.
24. Liu, H.; Yang, Z.; Meng, L.; Sun, Y.; Wang, J.; Yang, L.; Liu, J.; Tian, Z., *J. Am. Chem. Soc.* **2014,** *136*, 5341.
25. Yang, D.; Afroosheh, S.; Lee, J. O.; Cho, H.; Kumar, S.; Siddique, R. H.; Narasimhan,V.; Yoon, Y.-Z.; Zayak, A. T.; Choo, H., *Anal. Chem.* **2018,** *90*, 14278.
26. Wang, Q.; Yang, L.; Yang, X.; Wang, K.; Liu, J. *Analyst* **2013,** *138*, 5150.
27. Sun, F.; Bai, T.; Zhang, L.; Ella-Menye, J.-R.; Liu, S.; Nowinski, A. K.; Jiang, S.; Yu, Q. *Anal. Chem.* **2014,** *86*, 2394.
28. Pearson, B.; Wang, P.; Mills, A.; Pang, S.; McLandsborough, L.; He, L. *Anal. Methods* **2017,** *9*, 4739.

29. Yuan, K.; Mei, Q.; Guo, X.; Xu, Y.; Yang, D.; Sánchez, B. J.; Sheng, B.; Liu, C.; Hu, Z.; Yu, G.; Ma, H.; Gao, H.; Haisch, C.; Niessner, R.; Jiang, Z.; Zhou, H. *Chem. Sci.* **2018,** *9*, 8795.
30. Wang, H.; Zhou, Y.; Jiang, X.; Sun, B.; Zhu, Y.; Wang, H.; Su, Y.; He, Y., *Angew. Chem. Int. Ed.* **2015,** *54*, 5136.
31. Ma, R.; Hu, J.; Cai, Z.; Ju, H. *Nanoscale* **2014,** *6*, 3156.
32. Haldavnekar, R.; Venkatakrishnan, K.; Tan, B. *Nat. Commun.* **2018,** *9*, 3065.
33. Moeinian, A.; Gür, F. N.; Gonzalez-Torres, J.; Zhou, L.; urugesan, V. D.; Dashtestani, A. D.; Guo, H.; Schmidt, T. L.; Strehle, S. *Nano Lett.* **2019,** *19*, 1066.
34. Szafranski, C. A.; Tanner, W.; Laibinis, P. E.; Garrell, R. L. *Langmuir* **1998,** *14*, 3589.
35. Li, S.; Zhou, Q.; Chu, W.; Zhao,W.; Zheng, J., *Phys. Chem. Chem. Phys.* **2015,** *17*, 17645.
36. Abdi, H.; Williams, L. J. *WIREs Computational Statistics* **2010,** *2*, 459.

Chapter 4: Developing Non-invasive SERS-based Diagnostic Kit for Urinary Metabolites Towards Threatened Miscarriage Diagnosis within 30 min

Abstract. Successful translation of laboratory-based surface-enhanced Raman scattering (SERS) platforms to clinical applications requires multiplex and ultratrace detection of small biomarker molecules. However, these biomarker molecules are generally present in a complex biofluid which exhibit tremendous interferences, significantly increasing the challenge of detecting them at low concentrations. Herein, we developed a SERS-based diagnostic kit for non-invasive metabolites detection from real urine samples towards threatened miscarriage diagnosis. We first employ a ZipTip to pretreat and isolate the target biomarkers from the urine samples and then integrate our developed "confine-and-capture" SERS strategy, whereby we use specific nanoscale surface chemistry to capture targeted metabolite from a complex urine matrix prior to confining them on a superhydrophobic SERS platform. We then apply chemometrics, including principal component analysis and partial least-squares regression, to convert molecular SERS fingerprint information into quantifiable readouts. The whole screening procedure requires only 30 min, including urine pretreatment, sample drying on the SERS platform, SERS measurements, and chemometric analyses. These readouts correlate well with the pregnancy outcomes in a case-control study of 40 patients presenting threatened miscarriage symptoms.

4.1 Introduction

Threatened miscarriage occurs in 15 – 20% of all pregnancies in the first trimester and is characterized by abdominal pain or vaginal bleeding[1,2]; 25% of these pregnancies progress to suffer spontaneous miscarriage. Serum progesterone has been proposed as a useful clinical biomarker to predict the risk of miscarriage[3-8]. However, the long turnover time of hours to days and invasive nature of the test limits its diagnostic utility, as a clinical management decision needs to be made on the spot, and appropriate counselling undertaken at the same time. This delay inadvertently creates additional psychological and physiological distress to patients. Despite the strong clinical impetus for rapid and non-invasive diagnosis of threatened miscarriage to achieve prompt medical intervention, there is currently no point-of-care diagnostic platform for clinicians to predict miscarriage risks among patients exhibiting symptoms of threatened miscarriage.

A recent metabolomic investigation of threatened miscarriage using urine samples revealed a panel of metabolites, which can serve as potential biomarkers for non-invasive diagnosis of spontaneous miscarriage.[9] In particular, there is a positive correlation between the risk of spontaneous miscarriage and the relative abundance of two metabolites from the progesterone and cortisol families: 5β-pregnane-3α,20α-diol-3α-glucuronide (pregnane) and tetrahydrocortisone (THC). Liquid chromatography-mass spectrometry (LC-MS) shows that pregnane% ≥ 98.7% (relative pregnane/THC ratio of 76/1) corresponds to an ongoing pregnancy; whereas pregnane% ≤ 97.4% (relative ratio of 38/1) corresponds to a spontaneous miscarriage. However, LC-MS analysis generates semi-quantitative results, requires long screening time, and has limited sensitivity, thus hindering the use of metabolomics for point-of-care risk stratification for spontaneous miscarriage.

We hypothesize that surface-enhanced Raman scattering (SERS) platforms can overcome the aforementioned limitations in metabolite analyses by providing specific

chemical fingerprint of each metabolite.[10-12] The plasmonic nanoparticles on the SERS platform generate intense electromagnetic field enhancements, significantly enhancing molecule-specific Raman vibrational fingerprints by $>10^9$-fold in molecules with large Raman scattering cross-sections and with affinity to the plasmonic nanoparticle surfaces.[13,14] Such tremendous signal enhancement enables quantitative and multiplex ultratrace detection within a short measurement time[15]. However, to successfully employ SERS for point-of-care diagnostic of spontaneous miscarriage, the following challenges must be overcome: (1) efficient extraction of dilute target urine metabolites (nanomolar levels) from a complex sample matrix, (2) ultrasensitive detection for metabolites with weak Raman scattering cross-sections and no affinity to plasmonic nanoparticles, and (3) accurate spectral analyses for miscarriage risk stratification. Most importantly, screening outcomes should be known in the shortest time frame possible.

Herein, we demonstrate the development of rapid and ultrasensitive SERS-based diagnostic kit for urinary metabolites detection towards threatened miscarriage diagnosis within 30 mins. By pre-treating and isolating the relevant metabolites using a ZipTip from patients' urine matrix, we employ the SERS platform featuring the two-pronged "confine-and-capture" strategy developed in Chapter 3 to collect relevant SERS spectra. Our approach enables efficient generation of strongest SERS signal from our target metabolites analyte. We further employ chemometric analysis to process large data sets across the entire measured spectral range, thereby enabling us to achieve quantitative multiplex screening of metabolites down to parts-per-trillion levels (Scheme 4-1). As our proof-of-concept, we perform a case-control study of 40 urine samples collected from pregnant women presented with threatened miscarriage. To quantify the relative concentrations of these two metabolites from patient samples with known pregnancy outcomes, we successfully correlate SERS readouts with miscarriage risks among the patients within 30 minutes. Our

ability to detect metabolites from patient samples at ultra-trace levels implies the potential application of our SERS platform as non-invasive point-of-care screening technology for other diseases and conditions in the broad field of metabolomics.

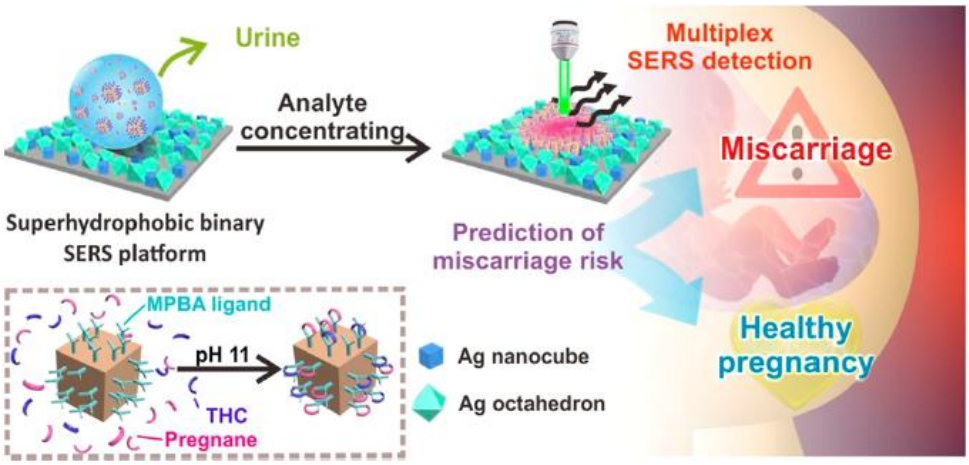

Scheme 4-1. Schematic illustration of our metabolomics-based SERS diagnostic platform to identify miscarriage risk among pregnant women presenting symptoms of threatened miscarriage. We outline a confine-and-capture strategy for ultrasensitive metabolite screening: a superhydrophobic SERS platform physically confines metabolites on the platform and a probe molecule (4-mercaptophenylboronic acid, MPBA) selectively captures target metabolites from a complex urine matrix.

4.2 Results and discussion

To assess the risk of threaten miscarriage in actual urine samples, there are several challenges such as various additional components present in urine, including urea, creatinine, and ions within the sample matrix while quantifying the THC and pregnane. Hence, we first test our system using artificial urine to provide a simpler and controlled matrix to understand the system, which can then be incorporated for actual urine analysis. Artificial urine is prepared by mixing 24.2 g urea, 10.0 g sodium chloride, 6.0 g of monopotassium phosphate, 6.4 g sodium phosphate in 100 mL of DI water. To demonstrate the SERS detection from artificial urine, a ZipTip is utilized as a sample pre-treatment

method to extract our target metabolites from artificial urine (Figure 4-1 B). In general, passing the artificial urine through the ZipTip microcolumn will allow the relatively non-polar target urine metabolites to be adsorbed on the C18 resin. Rinsing the column first with water elutes any adsorbed ions from the system. Subsequent rinsing with methanol extracts the urine metabolites from the microcolumn. Subsequently, we react the MPBA-functionalized Ag nanocubes with the metabolites at alkaline pH to facilitate the covalent bond formation and allow selective target analyte capture.

To build a quantification model to determine the relative abundance of pregnane/THC, we collect SERS spectrum of our MPBA reacted with a series of pregnane and THC mixture that have different percentage of pregnane in artificial urine. Typically, a pregnane% sample indicates that there is 90% pregnane and 10% THC in the solution. The corresponding pregnane (THC) concentrations for pregnane% of 97.4% and 98.7% are 0.0974 nM (0.0026 nM) and 0.0987 nM (0.0013 nM) respectively.[16, 17] We further treat the collected SERS spectra using PLS to study the pregnane percentage by analyzing the peak disappearance and wavelength shift within the whole spectra for MBPA after reacting with metabolites that have different percentages of pregnane (Figure 4-1C). [18] Multivariate PLS analysis will automatically resolve the minor changes in the SERS spectra arising due to the different metabolite concentrations in a multiplex setup comprising biofluids and construct a prediction model for miscarriage risk determination. As a result, PLS model is build up from 90% - 100% of pregnane and correlation coefficient is 0.971 (Figure 4-1D).

To further validate our PLS regression model, we collect SERS spectrum from a simulated high-risk and low-risk sample which are spiked with pregnane:THC ratio at 97.4% and 98.7%, respectively. Both simulated high-risk and low-risk samples will undergo the same pretreatment and detection process. The PLS prediction results show that the high-risk sample is predicted to be (97.2 ± 0.8)% and while the low-risk sample is predicted as

(98.9 ± 0.3)%, which are well in line with the spiked amount (Figure 4-1E). The further PCA analysis further demonstrate the clear discrimination among these two high-risk (miscarriage) and low-risk (ongoing pregnancy) groups. Hence, these results show that the ZipTip allows successful extraction of our target analytes from the artificial urine sample and that the PLS prediction model can predict unknown samples fairly accurately. Therefore, our entire method enables PLS prediction of the pregnane contents from artificial urine with a high accuracy.

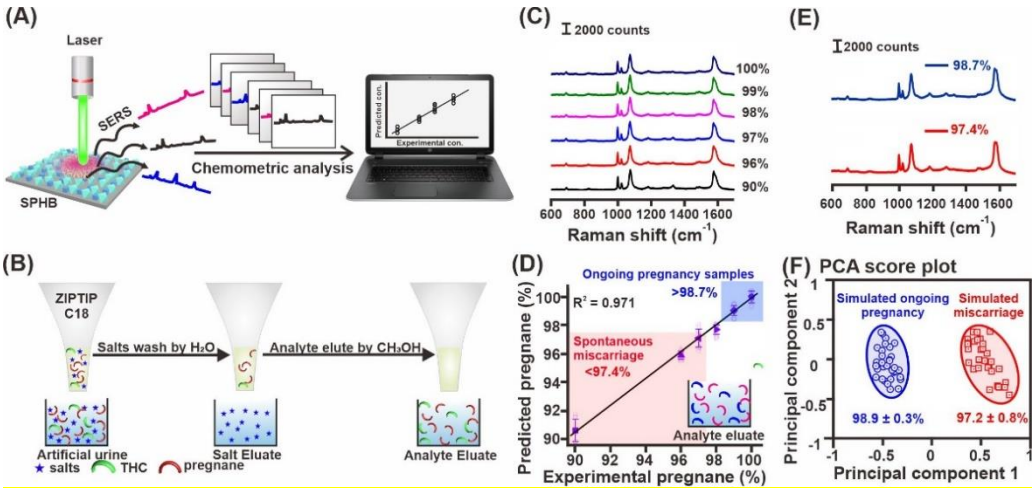

Figure 4-1. Chemometric study of SERS spectra. (A) Schematic illustration of the process of Raman spectra collection, followed by spectral analyses using PCA and PLS. (B) Schematic illustration of sample pre-treatment procedures of urine prior to SERS measurements. (C) PLS prediction model is prepared by spiking artificial urine with various pregnane% (10^{-4} M). The correlation coefficient is 0.971. (D) PCA result of simulated ongoing pregnancy urine sample (pregnane% = 98.7%) and simulated miscarriage urine sample (pregnane% = 97.4%) with 95% confidence ellipses. The prediction results are 98.9 ±0.3 % and 97.2 ±0.8 %, respectively. (E) SERS spectra of artificial urine at different pregnane% after sample pre-treatment. (F) SERS spectra of artificial urine spiked with pregnane% of 98.7% and 97.4% to represent ongoing pregnancy and spontaneous miscarriage, respectively.

To evaluate the applicability of our SERS platform for threatened miscarriage diagnosis, we conduct a case-control study of 40 women presenting threatened miscarriage symptoms between 5 and 10 weeks of gestation at the emergency department of KK Women's and Children's Hospital (CIRB ref: 2013/320/D). Urine specimens are collected at presentation. We classify women who subsequently had spontaneous miscarriages as cases (n = 20) and those with ongoing pregnancy at 16 weeks gestation as controls (n = 20). Differences in SERS spectral signatures are observed from these two patient groups (Figure 4-2B). To establish a calibration model for metabolite level quantification, we use urine specimens from nonpregnant women. We spike the urine samples from nonpregnant women with various pregnane% contents to build up the prediction model (Figure 4-2C and 4-3). The linear coefficients of this PLS prediction model are higher than 0.99, signifying reliability of our method even among patient urine samples.

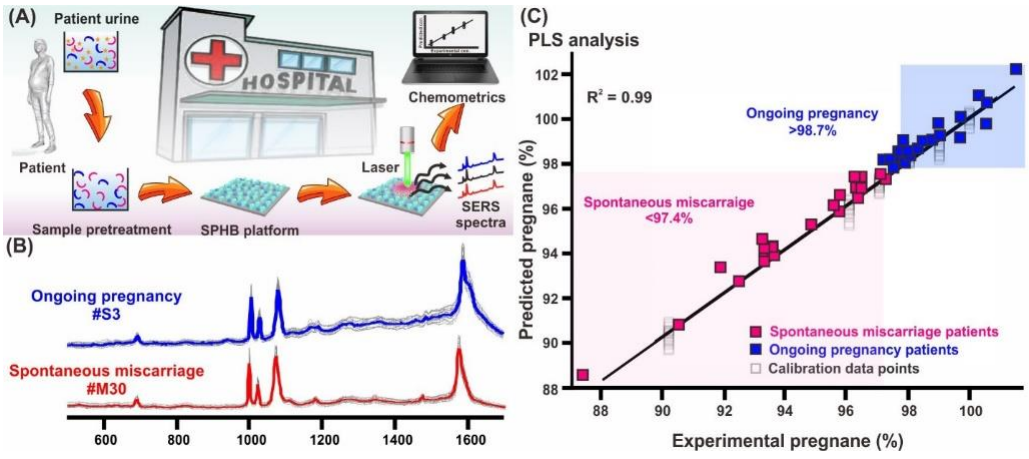

Figure 4-2. (A) Process of patient sample preparation, SERS screening and chemometric analysis. (B) Representative SERS spectra of urine samples collected from miscarriage patient number 30 and ongoing pregnancy patient number 3. (C) Building up PLS prediction model by mixing various pregnane% (10^{-10} M) with non-pregnant urine samples.

Pregnane% from 20 ongoing pregnancy urine samples (blue squares) and 20 spontaneous miscarriage urine samples (pink squares).

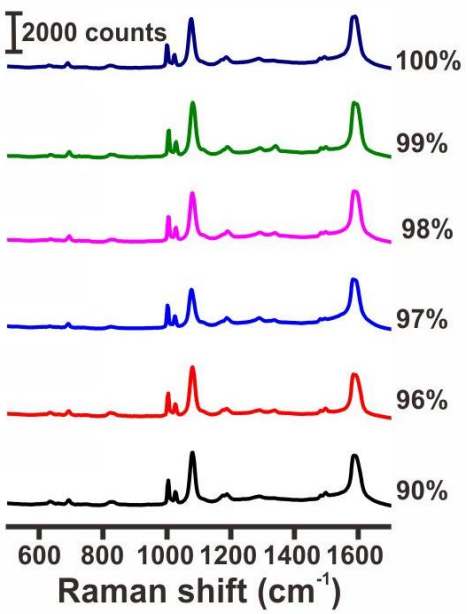

Figure 4-3. SERS spectra for spiked urine sample. SERS spectra of urine collected from non-pregnant women spiked with different pregnane%.

For the 40 patient samples presenting threatened miscarriage symptoms, we extract a minimum of 25 spectra for each patient sample for analysis. The SERS spectra are loaded into the prediction model for quantification of metabolite levels. The metabolite levels obtained from our SPHB-mirror SERS platform show excellent correlation with those obtained via LC-MS analyses (Table 4-1). The absolute difference between SERS-predicted pregnane% and LC-MS is 0.0−3.1%. This slight deviation may arise from the use of single measurements in the LC-MS analyses. Hence, we successfully employ our SPHB-mirror platform to perform quantitative and multiplex metabolite detection in patient samples, notably at ultratrace sub-nanomolar levels using just 10 μL of urine. In our detection system, the whole screening procedure requires only 30 min, including urine pretreatment, sample drying on the SPHB-mirror platform, SERS measurements, and chemometric analyses. This

detection method is faster than conventional LC-MS analyses, which can take several hours to days for urine metabolite profiling.[19, 20] This finding thus establishes our SERS detection approach as a promising point-of-care tool for triaging the risk of spontaneous miscarriage in patients presenting with threatened miscarriage in a clinical setting.

No.	LC-MS results (%)	SERS predicted results (%)	Absolute difference (%)	Outcome
S1	98.6	100.1 ± 0.3	1.5	Ongoing pregnancy
S2	98.8	99.2 ± 0.2	0.4	Ongoing pregnancy
S3	99.1	98.7 ± 0.4	0.4	Ongoing pregnancy
S4	99.0	102.3 ± 0.5	3.3	Ongoing pregnancy
S5	98.7	98.6 ± 0.4	0.1	Ongoing pregnancy
S6	99.3	101.1 ± 0.6	1.8	Ongoing pregnancy
S7	98.2	98.5 ± 0.2	0.3	Ongoing pregnancy
S8	98.7	99.1 ± 0.4	0.4	Ongoing pregnancy
S9	98.7	98.0 ± 0.3	0.7	Ongoing pregnancy
S10	99.0	99.0 ± 0.6	0.0	Ongoing pregnancy
S11	98.1	98.0 ± 0.2	0.1	Ongoing pregnancy
S12	98.7	97.9 ± 2.2	0.8	Ongoing pregnancy
S13	99.3	99.2 ± 0.2	0.1	Ongoing pregnancy
S14	99.4	98.3 ± 0.6	1.1	Ongoing pregnancy
S15	99.6	98.5 ± 0.7	1.1	Ongoing pregnancy
S16	98.2	98.0 ± 0.9	0.2	Ongoing pregnancy
S17	99.4	99.3 ± 0.1	0.1	Ongoing pregnancy
S18	99.6	100.7 ± 0.2	1.1	Ongoing pregnancy
S19	98.9	99.8 ± 0.6	0.9	Ongoing pregnancy
S20	98.9	99.1 ± 0.1	0.2	Ongoing pregnancy
M21	87.7	88.6 ± 0.7	0.9	Miscarriage
M22	96.7	97.5 ± 0.2	0.8	Miscarriage
M23	97.2	96.0 ± 0.2	1.2	Miscarriage
M24	97.9	97.6 ± 0.2	0.3	Miscarriage
M25	98.2	97.4 ± 0.5	0.8	Miscarriage
M26	94.7	93.7 ± 0.2	1.0	Miscarriage
M27	97.2	95.3 ± 0.3	1.9	Miscarriage
M28	94.1	96.8 ± 0.4	2.4	Miscarriage
M29	93.1	92.4 ± 1.1	0.7	Miscarriage
M30	96.7	96.9 ± 0.4	0.2	Miscarriage
M31	98.8	97.3 ± 0.5	1.5	Miscarriage
M32	91.9	90.7 ± 0.3	1.2	Miscarriage
M33	95.1	94.1 ± 0.3	1.0	Miscarriage
M34	95.5	94.7 ± 0.8	0.8	Miscarriage
M35	92.7	93.4 ± 0.9	0.7	Miscarriage
M36	95.7	92.8 ± 0.3	2.9	Miscarriage
M37	96.7	96.6 ± 0.2	0.1	Miscarriage
M38	95.5	94.0 ± 0.4	1.5	Miscarriage
M39	95.8	96.7 ± 0.3	0.9	Miscarriage
M40	98.4	96.6 ± 0.6	1.8	Miscarriage

Table 4-1. Relative pregnane% measured from our SERS platform compared against LC-MS analyses for ongoing pregnancy samples (S1-S20) and miscarriage samples (M1-M20).

4.3 Conclusion

In conclusion, we have developed a SERS-based diagnostic kit towards threatened miscarriage diagnosis, which is capable of performing multiplex and ultrasensitive metabolite screening within 30 minutes. Pretreatment using ZipTip enables successful isolation of our target metabolite from urinary sample for SERS analysis. By employing our developed unique SPHB substrate with a confine-and-capture strategy, our SERS-based diagnostic kit is capable of metabolite-specific fingerprints. Further PLS analyses successfully convert all molecular fingerprints across the entire spectral window into quantifiable SERS readouts, generating a linearity range spanning 7 orders of concentration

changes. More importantly, PLS analyses can also pick up minor changes in metabolite concentrations at 0.1 nM levels in a multiplex setup comprising biofluids, thereby enabling us to apply our platform to quantitatively screen patient samples for key metabolites rapidly. Our SERS platform thus resolves various technical challenges that plague SERS substrates and restrict their translation into practical screening tools.

Using our platform, we can quantify both pregnane and tetrahydrocortisone levels among 40 pregnant women presenting symptoms of threatened miscarriage in a case-control study. Threatened miscarriage is one of the most common gynecological emergencies worldwide and there is currently no point-of-care screening tests to identify miscarriage risks. Clinicians typically adopt a 'watch-and-wait' strategy or administer routine treatment with oral progestogens which may not be beneficial for all patients. Our non-invasive detection approach will significantly reduce undue distress among patients and enable clinicians to administer prompt medical intervention. From a broader perspective, this unprecedented combination of our SERS platform with metabolomics present multiple advantages over existing analytical platforms, including highly specific molecular fingerprinting for unambiguous metabolite identification, label-free multiplexing capabilities, ultralow sub-nanomolar detection limits (parts-per-trillion levels), straightforward sample treatment, low sample volume requirements, and non-invasive rapid quantification. Our approach can potentially be applied to screen for various diseases in numerous clinical settings and is particularly useful where only small sample volumes are available for screening, such as tears or sputum.

4.4 Material and methods

Preparation of calibration curve. We prepared a series of urine sample with various percentage of pregnane in the range of 90-100 % by mixing pregnane and THC solution of same concentration with calculated respect volume. For instance, we prepared the urine

samples which containing 90% pregnane and 10% THC by mixing 90 µL-pregnane (0.1 mM) with 10 µL-THC (0.1 mM) solution. The control samples we will replace the pregnane and THC with 10 µL of pure H_2O.

Patient recruitment. Patients presenting at the KK Women's and Children's Hospital (KKH) Singapore, 24-h Women's Clinic were recruited. Inclusion criteria were (i) patients with a single intrauterine pregnancy between 6 and 10 weeks of gestation (confirmed and dated by ultrasonography) and (ii) patients presenting with pregnancy-related per vaginam bleeding. Women with previous episodes of per vaginam bleeding or women treated with progesterone for previous per vaginam bleeding in the current pregnancy, or women diagnosed with inevitable miscarriage, missed miscarriage, blighted ovum or women who are planning to terminate the pregnancy were excluded. Urine samples were collected at presentation for metabolite analysis.

Sample pre-treatment for artificial urine and patient urine samples. The calibration curve is using urine collected from non-pregnant patients to establish the baseline for pregnane and THC levels. A non-pregnant patient urine was spiked with different pregnane% to establish our calibration curve. Prior to reaction with MPBA-functionalized Ag nanocubes, the spiked non-pregnant patient urine was desalted and purified with ZIPTIP. After reaction with the functionalized nanocubes, the mixture was further treated and purified prior to drop casting on the superhydrophobic chip for SERS measurements. A minimum of three individual samples was drop casted on the chip to obtain an average reading. A total of 40 patient samples were measured, where 25 measurements were done in each patient sample.

Time breakdown of detection process. The whole screening procedure significantly decreases the time required to 30 minutes, including 3 minutes for urine pretreatment, 25 minutes for drying the sample on our SPHB-mirror platform, and 2 minutes for measurement and chemometric analysis.

References

1 Wahabi, H. A., Fayed, A. A., Esmaeil, S. A. & Bahkali, K. H. *Cochrane Database Syst. Rev.* **2011**, 3, CD005943.

2 Jouppila, P. *J. Clin. Ultrasound* **1985**. 13, 111.

3 DAYA, S. *Br. J. Obstet. Gynaecol.* ***1989***, 96, 280.

4 Sotiriadis, A., Papatheodorou, S. & Makrydimas, G. *BMJ* **2004**, 329, 155.

5 Arck, P.; Hansen, P. J.; Mulac Jericevic, B.; Piccinni, M.-P.; Szekeres-Bartho, J. *Am. J. Reprod. Immunol.* **2007**, 58, 279.

6 Lek, S. M.; Ku, C. W.; Allen Jr, J. C.; Malhotra, R.; Tan, N. S.; Østbye, T.; Tan, T. C. *BMC Pregnancy Childbirth* **2017**, 17, 78.

7 Ku, C. W.; Allen Jr, J. C.; Malhotra, R.; Chong, H. C.; Tan, N. S.; Østbye, T.; Lek, S. M.; Lie, D.; Tan, T. C. *Gynecol. Endocrinol.* **2015**, 31, 651.

8 Ku, C. W.; Allen Jr, J. C.; Lek, S. M.; Chia, M. L.; Tan N. S.; Tan, T. C. *BMC Pregnancy Childbirth* **2018**, 18, 360.

9 Ku, C. W.; Tan, Z. W.; Lim, M. K.; Tam, Z. Y.; Lin, C.-H.; Ng, S. P.; Allen, J. C.; Lek, S. M.; Tan, T. C.; Tan, N. S. *BBA Clin* **2017**, 8, 55.

10 Alvarez-Puebla, R. A.; Liz-Marzán, L. M. *Small* **2010**, 6, 610.

11 Jarvis, R. M.; Goodacre, R. *Chem. Soc. Rev.* **2008**, 37, 936.

12 Ru, L. E. C.; Blackie, E.; Meyer, M.; Etchegoin, P. G. *J. Phys. Chem. C* **2007**, 111, 13803.

13 Knoll, W. *Annu. Rev. Phys. Chem.* **1998**, 49, 638.

14 Ko, H.; Singamaneni, S.; Tsukruk, V. V. *Small* **2008**, 4, 1599.

15 Tran, V.; Walkenfort, B.; König, M.; Salehi, M.; Schlücker, S. *Angew. Chem. Int. Ed.* **2019**, 58, 446.

16 Ku, C. W.; Allen, J. C. Jr; Malhotra, R.; Chong, H. C.; Tan, N. S.; Østbye, T.; Lek, S. M.; Lie, D. **2015**, 31, 651.

17 Ku, C. W.; Tan, Z. W.; Lim, M. K.; Tam, Z. Y.; Lin, C. H.; Ng, S. P.; Allen, J. C.; Lek, S. M.; Tan, T. C.; Tan, N. S. *BBA Clin* **2017**, 8, 55.

18 Wold, S.; Geladi, P.; Esbensen, K.; Öhman, J. *J. Chemom.* **1987**, 1, 56

19 Chubatyi, N. D.; Pagnotti, V. S.; Bentzley, C. M.; McEwen, C. N. *Rapid Commun. Mass Spectrom.* **2012**, 26, 892.

20 Pluskal, M. G. *Nat. Biotechnol.* **2000**, 18, 104.

Chapter 5: Intensifying Specific Surface-enhanced Raman Scattering Fingerprinting for Machine Learning-Assisted Accurate Profiling of Structural Isomers

Abstract. Surface-enhanced Raman scattering enables fast interrogation of a mixture by fingerprinting their chemical components and unique structures. However, in biological systems, accurate sample identification faces great challenge due to the weakened signal specificity arising from overlapping signals from multiple components. Here, we present a SERS fingerprinting approach with intensified specificity over structural isomers, whereby the spectral data is acquired by diversifying their chemical interaction moieties with a surface functional probe. Supported by experimental and theoretical simulation, we show that multiple analyte and probe molecular states influence the configurations and intermolecular strength in which analytes interact with the probe, intensifying the specificity of the resulting SERS fingerprints and boosting their identification. Incorporating our method with machine learning algorithms, we successfully distinguish 6 chondroitin sulfates (CS) disaccharides structural complex and 3 potential structural interferences with reliable discriminatory accuracy of 100 %. Quantification of multiplex CS structure isomers is also achieved with remarkable sensitivity down to 10^{-11} mole. Our SERS fingerprinting approach combined with advanced machine learning data analysis thus demonstrate great potential for fast and accurate profiling of wide biological structure complexes.

5.1 Introduction

Identification of structurally analogous isomers is crucial for biomedical diagnostics because the relative levels of multiple molecular species provide important biochemical clues to the health and disease status of an individual.[1, 2] Although liquid chromatography-mass spectrometry (LC-MS) is principally employed for molecular characterization, it is not feasible to directly resolve structural analogues due to the highly similar fragmentation patterns generated. In this aspect, surface-enhanced Raman scattering (SERS) spectroscopy is well-suited for rapid and unambiguous discrimination of structural analogues even at trace level by providing molecule-specific vibrational fingerprint with single-molecule sensitivity.[3-5] However, current SERS differentiation of structural isomers is usually limited to large Raman cross sections molecules, such as molecules, or dyes with strong surface affinity, such as thiol-based nitrophenols, limiting their practicality for real-life applications.[6-8] Another key issue is that analyte identification and quantification typically involve manual spectral inspection, which cannot accurately process the complex and subtle spectral changes generated by multiplex structural analogues.[9-11] This challenge is further aggravated by the ultralow concentrations of most biologically significant target analytes. Thus, it remains a huge challenge to achieve rapid SERS identification and relative quantification of diverse structurally analogous isomers with high accuracy and reliability.

Herein, I demonstrate a machine learning-assisted identification and quantification of multiplex trace structurally analogous isomers by intensifying the isomer-specific SERS fingerprints upon interactions with a SERS probe, using chondroitin sulfate (CS) disaccharide isomers as a model. CS isomers have resembled skeleton structure with diverse structural variations in terms of the number and position of sulfate groups (Scheme 5-1A), and are responsible for directing cell division, neuronal development and cancer cell growth.[12-14] As such, sensitive recognition of the CS sulfation pattern is important to

elucidate the exact structure-function relationships, so as to advance understanding on key physio-pathological processes for various diseases including cancer.[15, 16] Our strategy features three parts: 1) use of superhydrophobic SERS sensing platform to physically enrich both plasmonic nanoparticles and analytes, 2) inducing multiple molecular states of SERS probe 4-mercaptopyridine (MPY) and CS isomers to diversify their chemical interaction configurations and 3) employment of machine learning tools to decipher the complex spectral changes for accurate and rapid quantification (Scheme 5-1B). Notably, our method achieves near 100 % discriminatory accuracy for 6 CS structural analogues. By using machine learning algorithms, including PLS, we can analyze and process large datasets for whole measured spectral range efficiently to perform ultra-sensitive, quantitative multiplex screening of diverse CS mixtures reach to 10^{-11} mole. We further achieve relative compositional analysis of 4 CS disaccharides (CS-A, CS-C, CS-E, and CS-D) from their complex mixtures, which is important to monitor the progression of breast cancer.[15-17] It is noteworthy that our strategy only requires 2 μL for analysis. Such small-volume analysis will be highly useful for future real-life application in which samples are scarce or limited. Our strategy is thus a powerful tool which is capable of recognizing multiple CS isomers with different sulfation patterns at trace levels, with the potential of being extended to other biological compounds. The insights will be highly useful to empower the discovery of specific biomarkers and reveal their structure-activity relationship, and advance SERS towards practical multiplex isomer differentiation for a wide number of isomers, even at low concentrations.

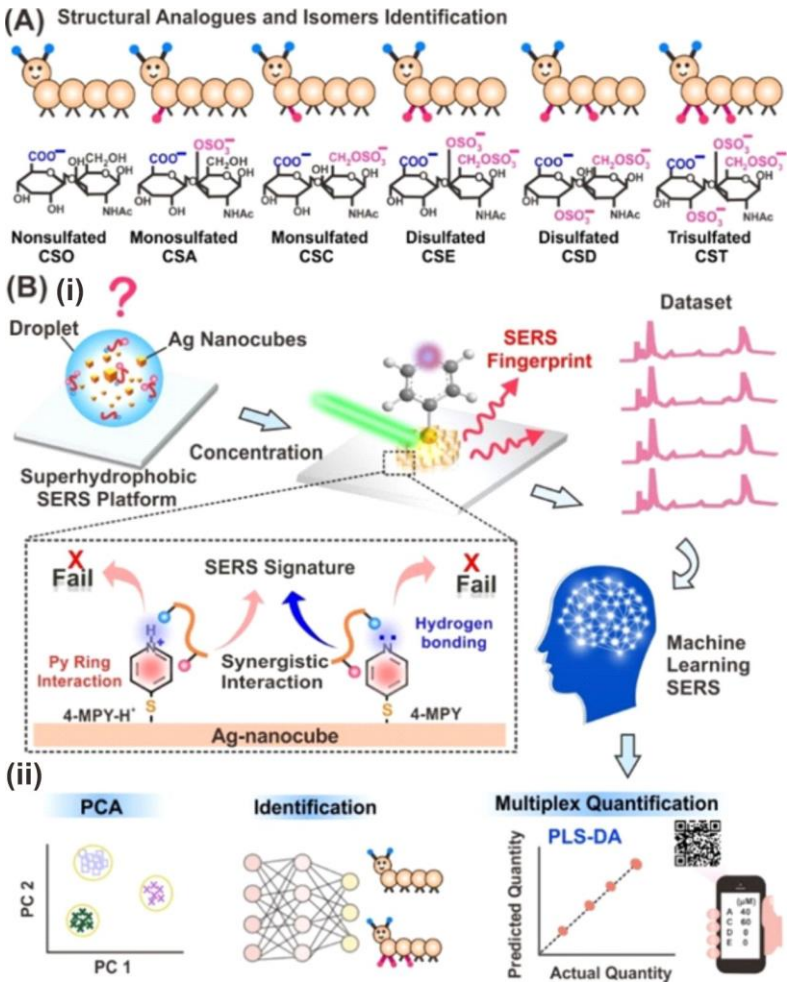

Scheme 5-1. (A) Schematic representation of the structural diversity of chondroitin sulfate disaccharide analogy and their relevant molecular structures, which share the same skeleton with slight variations in the number and position of sulfate groups. (B) Schematic demonstration of machine learning assisted structural isomers profiling, based on molecular level fingerprinting from synergistic probe/analyte interaction, to capture the target's structural information in a holistic way.

5.2 Results and discussion

In our work, we first mix MPY-functionalized plasmonic nanocubes with the target analytes, dropcast the aqueous droplet onto a superhydrophobic (SPHB) SERS substrate and measure the SERS signal after the droplet has fully dried (Figure 5-2A). Such platform combines a unique two-step strategy of "confine and capture" in one chip to achieve greatly

amplified and homogenous spectral signal, enhancing its identification capability of varied analytes (Figure 5-2B, C).[18] Notably, we employ MPY (pKa, 5.3) as a highly sensitive SERS functional probe because it exhibits multiple deprotonated and protonated molecular structural states that result in distinctive SERS fingerprint spectra (Figure 5-3).[19-21] Structurally, our target analytes share the same galactosamine and glucuronic acid that are joined via a glycosidic bond, and differ only in their sulfonation extent and positions. In general, CS disaccharides, are negatively charged due to sulfate groups (pKa, 0.5-1.5) and the carboxylic group (pKa, 3-5.7) enables CS to exhibit either protonated (-COOH), deprotonated states (-COO-) or both states.[22] Thus, we hypothesize that the various MPY and CS molecular states will enable diversified configurations in which the analytes can interact with the probe, empowering the analyte-specific SERS fingerprinting for their discrimination.

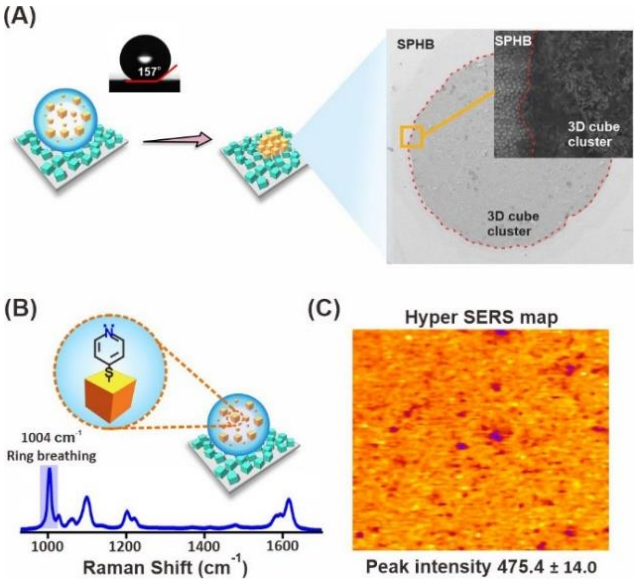

Figure 5-2. (A) Schematic illustration of the SERS sensing platform, a water droplet containing SERS-active Ag nanocubes placing on superhydrophobic SERS substrate and the SERS signal is collected upon fully drying the droplet. The inset is the SEM image of

the region with dried droplet. (B) SERS spectrum collected with MPY-functionalized Ag nanocubes. (C) Hyper SERS map over the pyridine ring breathing mode at 1004 cm^{-1}.

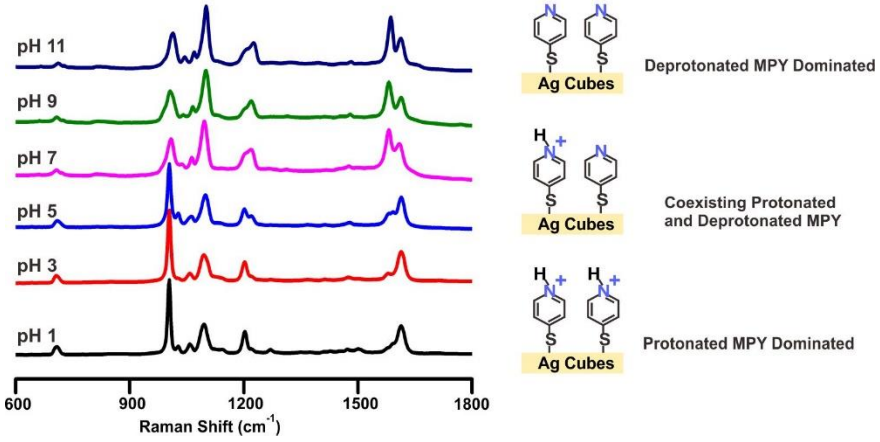

Figure 5-3. SERS spectrum of MPY acquired upon fully drying water droplet containing MPY-functionalized Ag nanocubes at different pH on SPHB SERS substrate. The right scheme shows the different molecular states of MPY on Ag nanocubes's surface.

We highlight that CS resemble an extreme set of structural isomers and they cannot be easily discriminated and quantified by using conventional LC-MS technique, therefore serving as an excellent model benchmark to assess our method. We first investigate the capability of our SERS method to identify diverse CS structural analogues with different sulfation extent, non-sulfated (CSO), mono-sulfated (CSA), di-sulfated (CSE), or tri-sulfated CS (CST) (Figure 5-4A).[17] Typically, we acquire SERS spectra upon after drying a 2 µL-water droplet (pH 5) containing mixed MPY-Ag nanocubes with aqueous (2mg/mL) CS analytes on SPHB substrate, respectively. In the absence of CS, the MPY SERS spectra exhibit many vibrational modes from 600 to 1800 cm^{-1}, whereby the strong modes are observed at 1004 and 1098 cm^{-1} and are indexed to the breathing mode of pyridine ring and stretching mode of C-S, respectively (Figure 5-4B). Another two pronounced peaks that show up at 1585 and 1613 cm^{-1} are attributed to the pyridine ring structure C=C stretching

mode with deprotonated and protonated N, respectively, which coexist on Ag surface at pH 5. Notably, in presence of CS disaccharides, the pyridine ring breathing vibration of MPY consistently undergo decrement and become broadened with emergence of several peaks in its fingerprint region, indicating their partial interaction with CS (Figure 5-4B and 5-4Ci). In addition, the relative peak intensity of the two C=C stretching modes at 1613 (protonated N) and 1585 cm^{-1} (deprotonated N) shows great differences depending on the interacted CS structures (Figure 5-4C ii). These spectral changes collectively indicate the molecular interactions of CS structural variants with MPY.

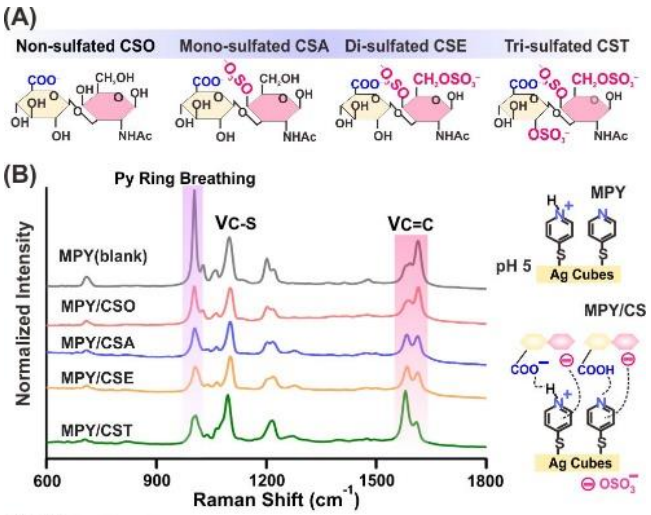

(D)

	(i) Py Ring Breathing Region			(ii) C=C Stretching
	Peak Decrease @1004 cm^{-1}	Peak Shift @1004 cm^{-1}	Singature Peaks (cm^{-1})	Peak Ratio $I_{C=C,N-H}$ / $I_{C=C,N}$
MPY	–	0	–	2.06
MPY/CSO	Yes	11	994 V_{C-O-C}	1.73
MPY/CSA	Yes	9	992 V_{S-O}	1
MPY/CSE	Yes	-9	995 V_{S-O} 1020 V_{C-O-S}	0.71
MPY/CST	Yes	-13, -6	999, 1013 V_{S-O}	0.39

Figure 5-4. (A) Molecular structure of CS disaccharides analogues with varied sulfate extent, nonsulfated CSO, monosulfated CSA, disulfated CSE, and trisulfated CST, respectively. (B) SERS spectra of MPY in the absence (denoted as blank) and presence of 4 different CS disaccharides. The scheme indicates the two MPY molecular structures on Ag surface at pH 5 and their proposed interaction with diversified CS. (C) Magnified SERS spectra of MPY (i) ring breathing mode and (ii) C=C stretching mode region in the presence of CS and their respective deconvoluted peaks. The spectra of MPY in the absence of CS (i) has been overlaid (black) in each case for comparison. (D) Table summarizing the spectral changes of MPY in the presence of CS including decrease of peaks intensity, peak shift, and appearance of new peaks, as well as changes of peak ratio.

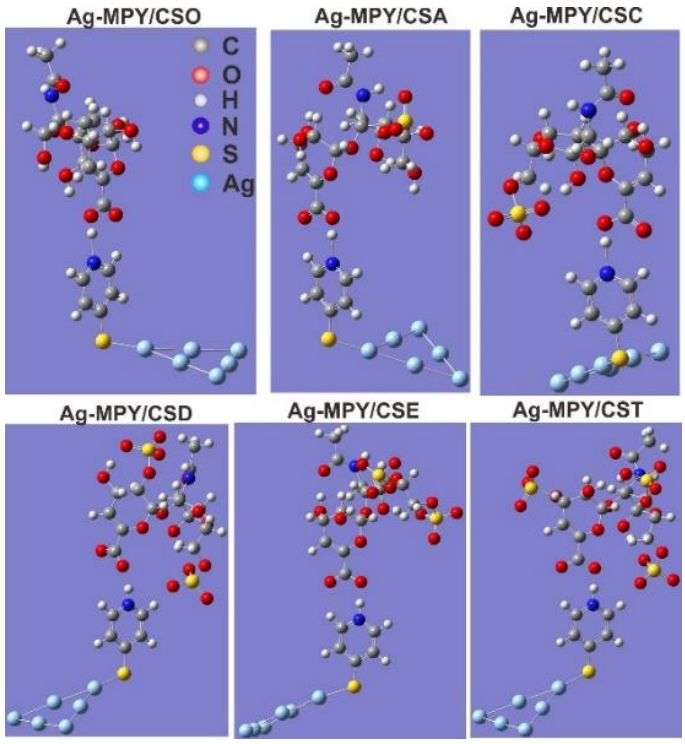

Figure 5-5. Complex structure of MPY with different CS structural variants for SERS spectrum calculation.

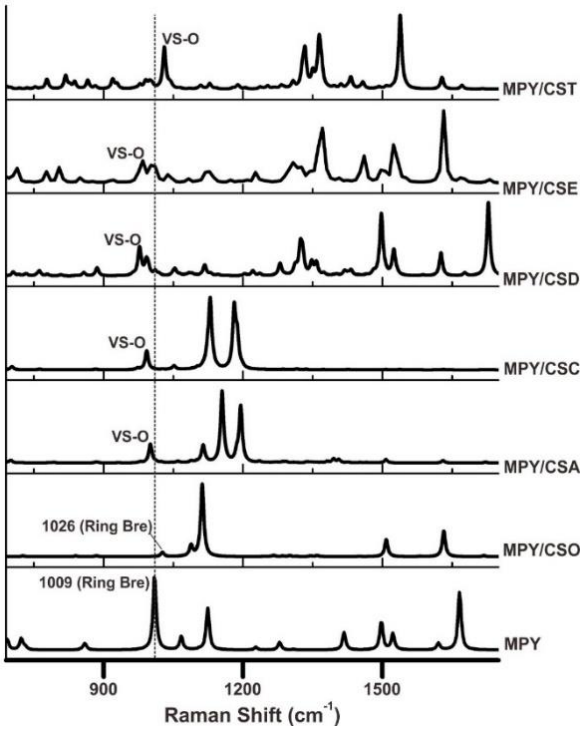

Figure 5-6. DFT simulated SERS spectrum from MPY and their complex structures with varied CS.

To corroborate the molecular origin and resolve the analyte specific spectral changes, density functional theory is performed to calculate the SERS spectrum of MPY and MPY coupled with CS, CSO, CSA, CSE, and CST respectively (Figure 5-5). MPY can complex with CS via forming hydrogen bond between N atom in pyridine ring and the carboxylic group from CS, resulting in higher energy required for pyridine ring breathing. Correspondingly, we observe a blue shift of the pyridine ring breathing mode of ~ 15 cm^{-1} from DFT simulated spectrum of MPY bonded non-sulfated CSO and mono-sulfated CSA (Figure 5-6). Nevertheless, a red shift of MPY's breathing mode and their overlap with S-O stretching mode of SO_3 group is observed as MPY is coupled with di-sulfated CSE and tri-sulfated CST. We attribute such changes to the increased negative sulfate group in CSE and CST which can form strong interactions with the π electron from pyridine ring, lowering the energy for breathing mode. Our experimental spectra thus match well with the DFT

simulation, whereby blue and red shift of MPY ring breathing mode is observed in MPY/CSO or CSA, and MPY/CSE or CST, respectively (Figure 5-4Ci). Meanwhile, the emerged SERS peaks at 994 and 992 cm^{-1} in MPY/CSO and MPY/CSA are indexed to the stretching mode of C-O-C and S-O from respective CSO and CSA. For MPY/CSE and MPY/CST, the relevant SERS peak at 995 and 999 cm^{-1} is due to the co-vibration of S-O stretching and pyridine breathing, whereas the peak at 1020 and 1013 cm^{-1} are specifically indexed to C-O-S stretching of CSE and S-O stretching of CST, respectively. Aside from these fingerprint changes, the relative peak intensity ratio of two experimental C=C stretching at 1613 (protonated N) and 1585 cm^{-1} (deprotonated N) shows a decreased trend as MPY is complexed with CSO, CSA, CSE, and CST. This result affirms the increasing negative sulfate extent affect the interaction of CS with MPY, resulting in varied SERS fingerprinting. These spectral changes, including peak intensity changes, peak position shift, and assignment of emerged new peaks, as well as changes of relative peak intensity ratio, collectively serve as sensitive and specific features which can be used to distinguish between the various CS structures (Figure 5-4D). Manual analysis of these spectra, however, suffer from lower efficiency and accuracy for targets identification, especially in case of massive spectra from multiple sample measurements.

To reduce manual visual inspection which can result in human error and tedious identification of the subtle spectral differences, I employ machine-learning algorithms to assist massive spectra analysis from multiple targets with improved efficiency and accuracy. Principal component analysis (PCA) is a clustering method that can be employed to reinforce the variance of different datasets from massive data across the entire spectral region and thus greatly enhance the discrimination of multiple targets (Figure 5-7A).[23, 24] We load a total 125 of SERS spectra and 76250 variables (wavenumbers) corresponding to MPY (blank), MPY/CSO, MPY/CSA, MPY/CSE, and MPY/CST (25 spectra for each

species, 610 variables for each spectra, all spectra collected under identical condition), respectively (Figure 5-8).

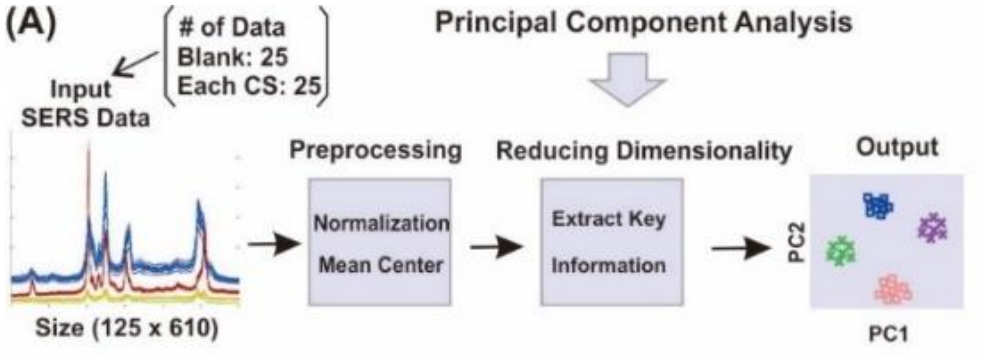

Figure 5-7. (A) Scheme illustrating principal component analysis algorithms (PCA), to reinforce discrimination of structural variants with high accuracy among high dimensional SERS dataset.

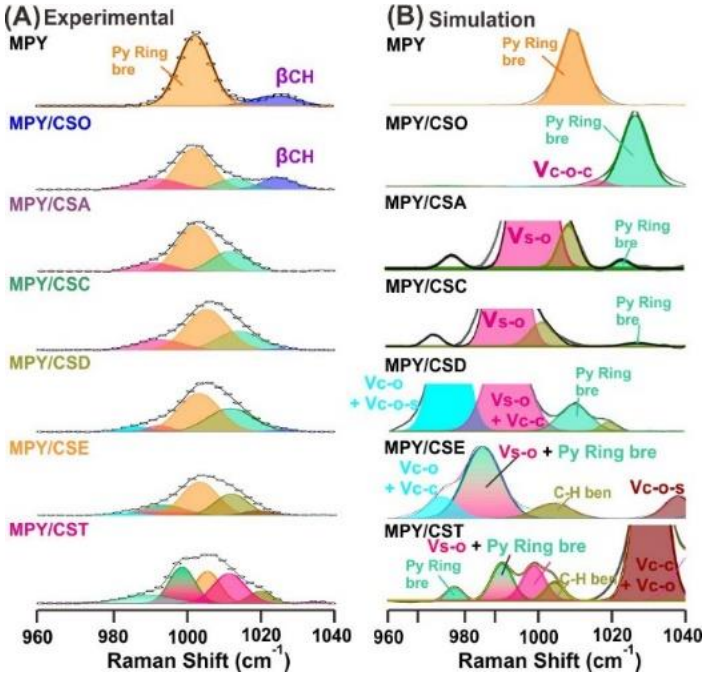

Figure 5-8. Experimental SERS spectra of pyridine ring breathing mode of MPY and that in the presence of multiple CS structural variants, as compared to the DFT simulated SERS spectra from varied MPY/CS complex structures, for peak assignment.

The preprocessing methods used are standard normal variate and mean center before the unsupervised clustering. We use a total of 3 principal components for PCA analysis, whereby PC1 account for a 69.3 % of the variance in the original SERS spectra, meaning it captures the maximum amount of information. The output PCA score plot reveals 5 distinct clusters along PC1, corresponding to 4MPY in the absence (blank) and presence of CSO, CSA, CSE, and CST, respectively, indicating that CS with different sulfation extent can be differentiated unambiguously (Figure 5-9A). The further analysis on the loadings/variables scores analysis reveals PC1 is strongly influenced by two spectral regions, 1004-1010 and 1570-1620 cm^{-1}, which is due to the pyridine ring breathing and C=C stretching mode, respectively (Figure 5-9B). In the first region, MPY demonstrates a strong and sharp band at 1004 cm^{-1}, and decrease in its intensity and broadens in the presence of CS. Hence, clusters related to MPY (blank) is unitarily distributed in the second quadrant of the PCA score plot. The formation of hydrogen bonding between nonsulfated CSO with MPY increase the intensity of C=C stretching with N-H at 1610-1620 cm^{-1}, thus driving clear discrimination of CSO from other sulfated CS.[25] The further co-interaction of negative sulfate anion with pyridine ring regulates the peak intensity of C=C stretching mode at 1570-1583 cm^{-1}, resulting in specific fingerprints that enable distinguishing the remaining sulfated CS, CSA, CSE, and CST. These results agree well with and surpass our previous manual analysis, with rapid and accurate extraction key variance from massive SERS spectrum for effective discrimination of structural variants.

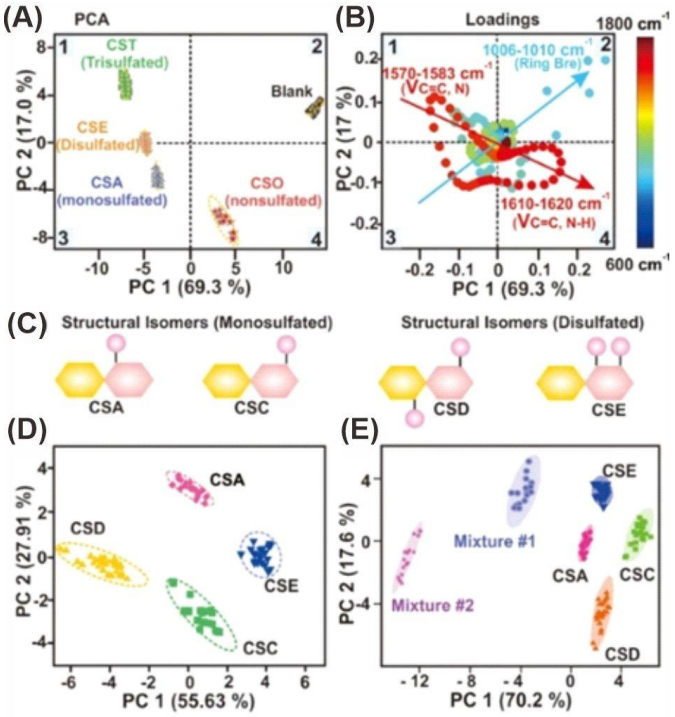

Figure 5-9 (A) PCA score plot of 125 SERS spectra from MPY interacted with CSO, CSA, CSE, and CST as well as MPY in the absence of CS (blank). (B) Corresponding loading (variables) plot to reveal the underlying variables accounting for principal components 1 and 2. (C) Schematic illustration of CS positional isomers, mono-sulfated CS (CSA and CSC) and di-sulfated CS (CSD and CSE). (D) PCA results of MPY interacted with 4 CS positional isomers, respectively. (E) PCA results of SERS spectra from MPY interacted with 4 CS positional isomers and their mixtures with different compositions (#1, CSA/CSC/CSD/CSE = 34/60/1/5; #2 CSA/CSC/CSD/CSE = 61/32/14/3).

	Predicted Analyte						
Actual Analyte	Blank	CSO	CSA	CSC	CSD	CSE	CST
Blank	100%	0%	0%	0%	0%	0%	0%
CSO	0%	100%	0%	0%	0%	0%	0%
CSA	0%	0%	100%	0%	0%	0%	0%
CSC	0%	0%	0%	100%	0%	0%	0%
CSD	0%	0%	0%	0%	100%	0%	0%
CSE	0%	0%	0%	0%	0%	100%	0%
CST	0%	0%	0%	0%	0%	0%	100%

Table 5-1 Machine learning predicted accuracy of multiple structural variants of CS using logistic regression model.

Next, we highlight that our method is capable of distinguishing CS positional isomers with same sulfation extent but at different sulfate positions (Figure 5-9C). Particularly, we apply unsupervised PCA over SERS spectra obtained from 4-MPY in the presence of two mono-sulfated CS positional isomer, CSA and CSC (C4- and C6- sulfated, respectively), and other two di-sulfated CS isomer (CSE and CSD) (Figure 5-10). The resulting PCA score plot demonstrates distinct clusters related to each CS, indicating that our SERS strategy is capable of differentiating positional isomers (Figure 5-9D). Further loading/variables scores analysis reveal the spectral region of 1600-1620 cm^{-1} that is indexed to the C=C stretching mode mainly drives the differentiation of mono-sulfated CSA and CSC. Simultaneously, the region of 1020-1026 cm^{-1}, which is indexed to the C-O-S vibration mode, determines the discrimination between di-sulfated CSD and CSE.[25] These results are further affirmed by DFT simulation of SERS spectrum from the CS coupled MPY (Figure 5-6). Remarkably, our approach also successfully discriminates mixtures of 4 CS complex structures from their neat CS components (Figure 5-9E). Upon applying supervised machine learning algorithm using logistic regression, a discrimination accuracy as high as 100% is achieved for prediction of 6 different CS structural variants and blank samples (Table 5-1). These results collectively illustrate that our SERS fingerprint readout are highly specific over multiple CS disaccharide variants, and machine learning algorithms can enable their rapid and accurate identification, greatly surpassing traditional LC/MS method.[17]

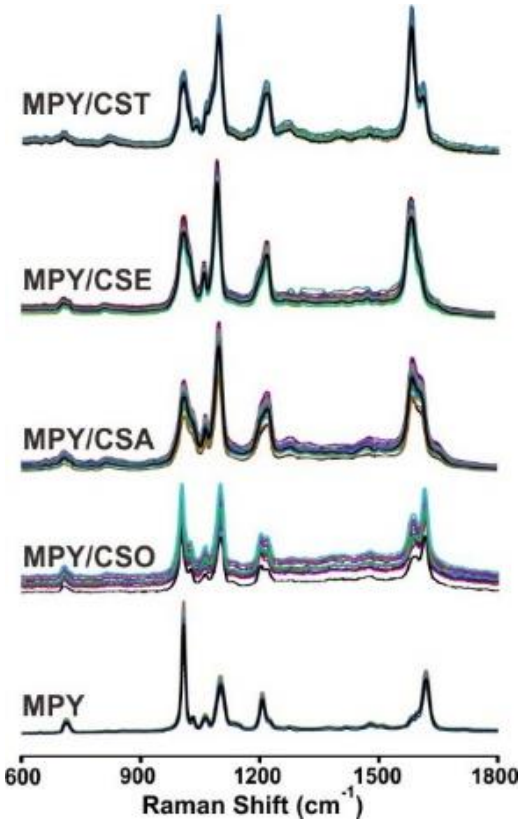

Figure 5-10. Experimental SERS spectrum from MPY (pH 5) in the presence of varied CS with different sulfonation extent, non-sulfated CSO, mono-sulfated CSA, di-sulfated CSE, and tri-sulfated CST. Total 125 spectrum, with 25 spectra for each sample.

To elucidate the intensive specificity of the resulting SERS fingerprinting, we investigate the molecular interaction in terms of both probe and analyte at molecular level. First, we mediate the molecular states of MPY probe by adjusting environmental pH to be from 1 to 11 for MPY-CS interaction, whereby the surface is mainly dominated by protonated and deprotonated MPY, respectively, as compared to their coexistence at pH 5. SERS spectrum were collected under identical experimental condition and PCA is employed to cluster the SERS spectra obtained from MPY interaction with CSA, CSC, CSD and CSE, at pH 1 and pH 11, respectively (Figure 5-11).

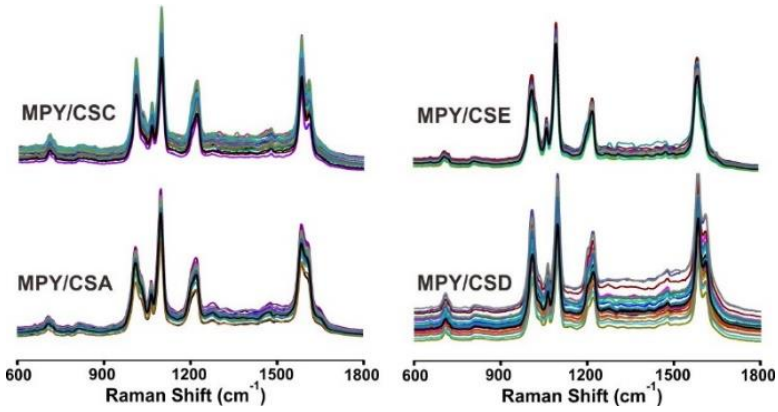

Figure 5-11. Experimental SERS spectrum from MPY (pH 5) in the presence of varied CS with same sulfonation extent but different sulfate group position, mono-sulfated CSA and CSC C, di-sulfated CSD and CSE.

Notably, the PCA plot failed to show clearly segmented clusters from different CS structures in case of interaction with MPY at pH 1 and 11, whereby clusters from mono-sulfated CSA and CSC partially overlap (Figure 5-12A and B, 5-13). These results demonstrate that it is challenging to differentiate CS structural isomers under conditions at both pH 1 and 11, despite applying advanced machine learning algorithm. This is likely arising from the weaken specificity of the relevant SERS fingerprinting. As compared to SERS spectra obtained at pH 1 and 11, we attain unambiguous identification of 4 CS isomers as CS interacting with MPY at pH 5. These results illustrate that the SERS fingerprinting of the MPY/CS complex formed at pH 5 are more specific as compared to that forming at pH 1 and 11, thus greatly boosting discrimination efficiency of CS structures even with slight variations. We attributed such intensified CS-specific SERS spectrum to the multiple molecular states of MPY (pKa 5.3) at pH 5, with coexistence of deprotonated and protonated MPY. Correspondingly, at pH 5, the carboxylic group of CS (pKa, 3-5.7) exhibit two molecular forms, protonated (-COOH) and deprotonated states (-COO-), and sulfate group (pKa, 0.5-1.5) remains deprotonated states. These multiple probe and analyte molecular states facilitate formation of diversified MPY/CS complexes via hydrogen

bonding and anion-pi interaction, intensifying the specificity of the resulting SERS fingerprint (Figure 5-12C). In contrast, for MPY/CS complex forming at pH 1 and pH 11, their interaction exhibits limited configuration, thus the resulting SERS spectrum exhibit similar features across the different CS isomers. The simulation of interaction of MPY and CS under multiple molecular states further affirms the formation of MPY/CS complex with diversified configuration (Figure 5-14). Our results thereby affirm our preliminary hypothesis that the coexistence of multiple molecular states favors the formation of diversified configurations of molecular complex, intensifying the specificity of SERS fingerprinting.

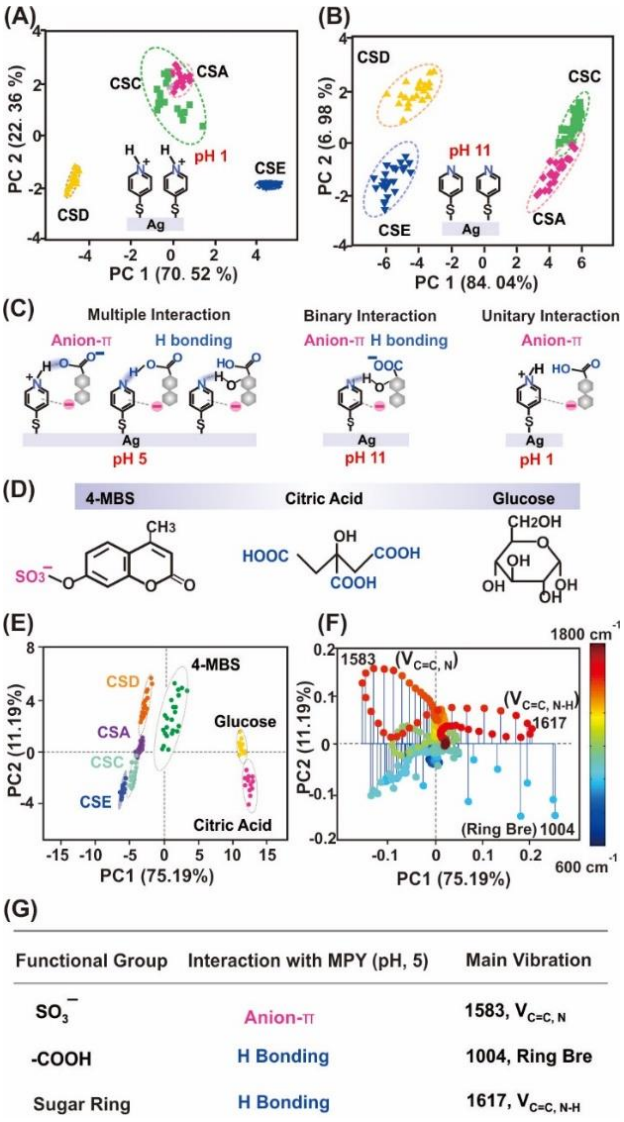

Figure 5-12. PCA score plot of SERS spectra from 4 CS positional isomers upon interacted with regulated MPY on Ag surface by adjusting pH at (A) 1 and (B) 11. The inset indicates the MPY molecular state under each condition. (C) Schematic illustration of the synergetic multiple interactions between MPY and CS disaccharide moiety at pH 5 for clear discrimination among diverse CS, which is superior to the binary interaction at pH 11 and unitary interaction at pH 1. (D) Molecular structure of 4-MBS, citric acid, and glucose, with resembled sulfate and carboxylic group, as well as monosaccharide sugar skeleton. (E) PCA analysis of MPY reacted with 4 CS isomers, 4-MBS, citric acid, and glucose, respectively, as well as (F) the corresponding variables (600-1800 cm^{-1}) plot. (G) Table summarizing the 3 reactive moiety of CS structures with MPY and the corresponding interaction as well as the key Raman vibration variables contributing to their discrimination.

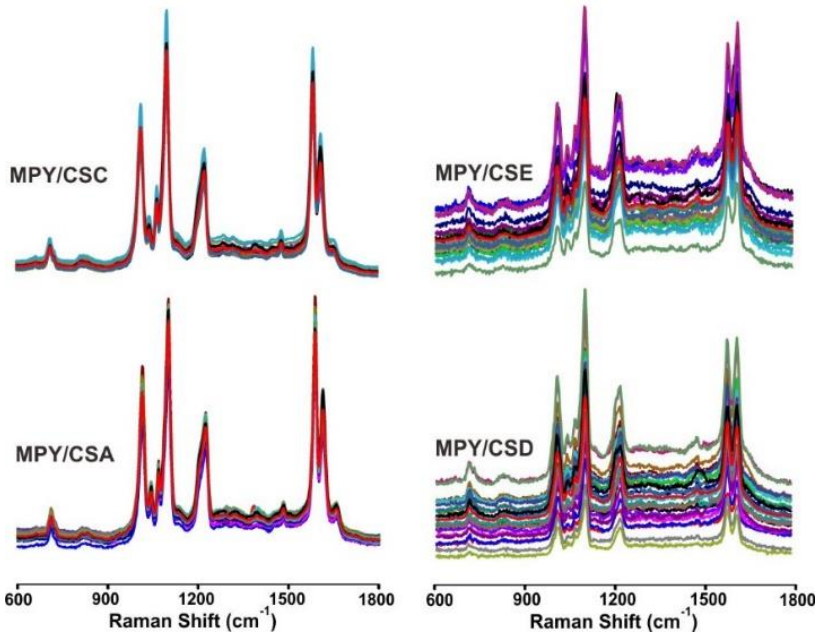

Figure 5-13. Experimental SERS spectrum from MPY (pH 11) in the presence of varied CS with same sulfonation extent but different sulfate group position, mono-sulfated CSA and CSC C, di-sulfated CSD and CSE.

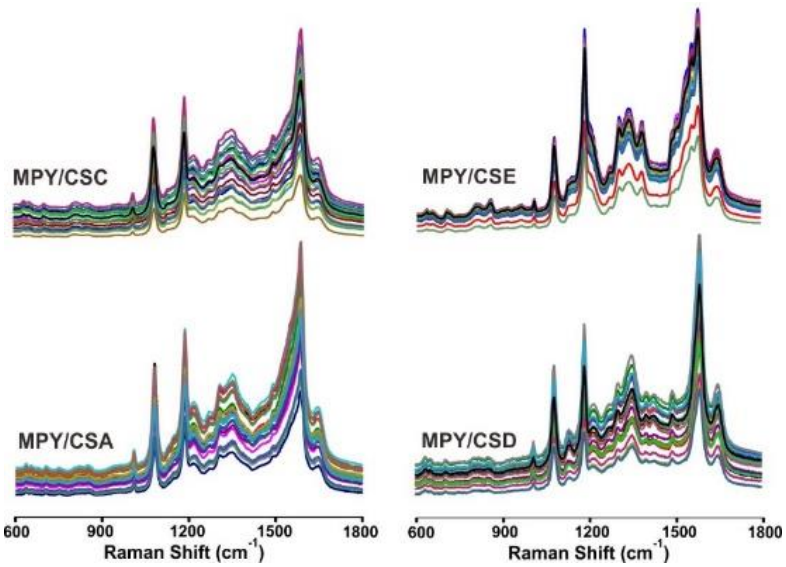

Figure 5-14. Experimental SERS spectrum from MPY (pH 1) in the presence of varied CS with same sulfonation extent but different sulfate group position, mono-sulfated CSA and CSC C, di-sulfated CSD and CSE.

Next, we investigate the separate response of relevant active structural regions, sulfate group, carboxylic group, and the sugar ring on the SERS fingerprinting of MPY. We study the SERS response of 4MPY (pH 5) in the presence of 4-methylumbelliferyl sulfate, citric acid, and glucose, which have the partially resembled functional group as CS structures (Figure 5-12D). We apply the same PCA to the SERS spectrum collected under identical condition with that of CS (Figure 5-15). Notably, the 2D PCA plot demonstrates well-distinguished clusters among each species and four different CS isomers, CSA, CSC, CSD, and CSE (Figure 5-12E). Further loadings plot analysis indicates that the ring breathing mode region near 1004 cm^{-1} and C=C stretching mode around 1617 cm^{-1} drives the unambiguous discrimination of citric acid (-COOH) and glucose, respectively, from other analytes, 4MBS and 4 CS (Figure 5-12F and 12G). Notably, 4MBS and all 4 CS structures have similar sulfate (-SO_3-) group, which enables interaction with MPY via anion-π, whereby their differentiation rely on both the C=C stretching mode at both 1583 and 1617

cm^{-1} and ring breathing mode region (Figure 5-10F and 10G). These results further affirm the intensified SERS fingerprinting over different structures and that the integration of machine learning is key to extract the key spectral variance for structural analysis. We further highlight that our strategy enables ready differentiation of target CS analytes from potential interfering compounds, which is significant for real world analysis with coexistence of multiple molecules.

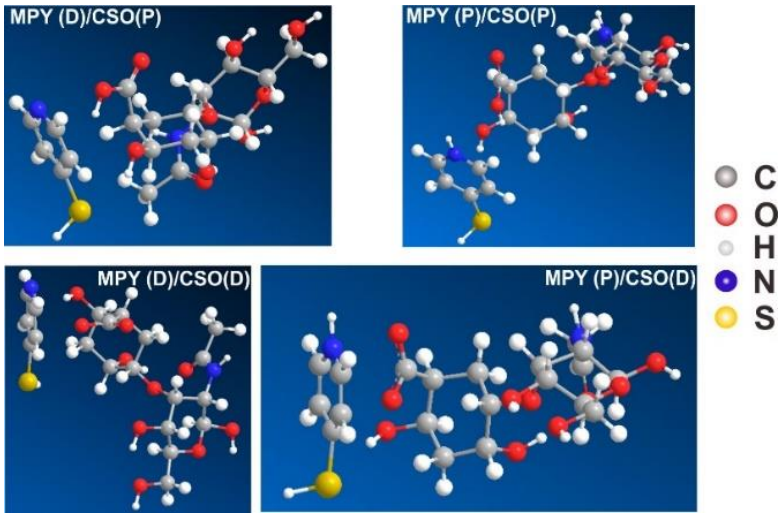

Figure 5-15. Optimized multiple molecular geometry of MPY complex with non-sulfated CSO using MM2 calculation. The deprotonated MPY and protonated MPY are represented as MPY (D) and MPY (P), respectively, while the CSO with carboxylic group (-COOH) and carboxylate anions (-COO-) are denoted as CSO (P) and CSO (D), respectively. The calculated minimized total steric energy for MPY(D)/CSO(P), MPY(P)/CSO(P), MPY(D)/CSO(D), and MPY (P)/CSO(D) are 16.86, 11.80, -2.62, and -133.35 kcal/mol, respectively.

Effective and fast multiplex quantification of structural isomers from complicated biological matrices, such as medicine, cell matrix, urine, is crucial for future development of point-of-care diagnosis. This is significant for biological studies because their concentrations can be used as health indicator. For instance, a compositional analysis

indicates an elevation of CSA and CSE along with decrement of CSC and CSD in the progression of breast cancer. Integrated with machine learning algorithms, we test the capability of our SERS fingerprinting technique to quantify the levels of 4 CS, CSA, CSC, CSD and CSE, from their mixtures (Figure 5-16A). Among multiple algorithms, multivariate partial least square regression (PLS) analysis is capable of resolving minor spectral changes after reacting with different analyte concentrations in a multiplex setup and build the quantification model for each component. We employ PLS over SERS spectra of MPY in the presence of multiple CSA, CSC, CSE, and CSD mixtures. The resultant prediction models display high linear coefficients of 0.96 – 0.98 for all of the four CS components, indicating that our method attains a good prediction accuracy for multiplex detection of diverse CS (Figures 5-16 B-E). As proof-of-concept, we employ the PLS calibration model to predict the abundance of relevant CS units in five different mixtures, which can be further transformed to machine readable QR codes (Figure 5-16F). Our method enables accurate and faster prediction of the relevant CS composition, which is advantageous over conventional LC-MS analysis. Notably, our method can detect down to a low concentration of 10 μM using an ultralow-volume μL droplet, highlighting that our method is highly promising for screening of complex structure and their variants.

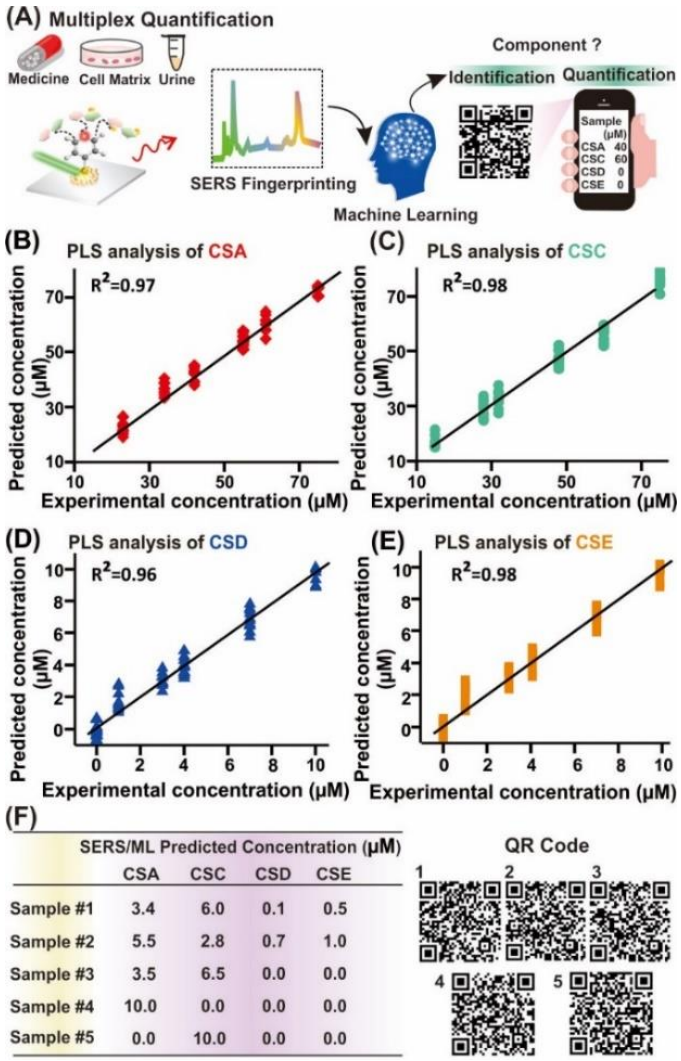

Figure 5-16. (A) Scheme illustrating machine learning multivariate PLS analysis enabled quantification and identification of multiplex CS structural variants with mobile readable QR code as output component information, which is applicable for relevant analysis in medicine, complex cell matrix, and urine. (B-E) PLS calibration curves of respective CS isomer (CSA, CSC, CSD and CSE respectively). (F) Table of our machine learning-SERS predicted component analysis from 5 samples and the generated 5 QR codes.

5.3 Conclusion

In summary, we present an accurate identification and quantification of multiplex structural variants, by using an intensified specificity of SERS fingerprint combined with

machine learning techniques. The various analyte and probe molecular states due to the multiple charged functional groups can allow the formation of diversified molecular complex with different configuration, thus intensifying the analyte-specific SERS fingerprints over varied analytes. As proof of concept, we showcase an unambiguous discrimination of a series of chondroitin sulfate disaccharide structures in the absence and presence of substitution of sulfate groups, as well as structures with different sulfonation extent and their substitution position. Such discrimination is rapid and accurate, with a reliable discrimination accuracy of 100 %, greatly superior to manual and tedious SERS spectral analysis and traditional LC/MS techniques. Integration with machine learning algorithms permits an accurate quantification of the CS levels from their complex mixtures, with prominent accuracy near 100 %. Our method collectively demonstrates the great potential for decoding CS sulfate patterns and serve as a rapid profiling method for multiple biological structural analogues and isomers, providing significant biomedical clues for biomedical diagnostics.

5.4 Material and methods

Chemicals. Silver nitrate (≥ 99%), anhydrous 1,5-pentanediol (≥ 97%), 4-Mercaptopyridine (95 %), toluene (99.5%), poly(vinylpyrrolidone) (PVP, average MW = 55000 g/mol), and 1H,1H,2H,2H-perfluorodecanethiol (PFDT, 97+%) were purchased from Sigma Aldrich; 3-aminopropyltriethoxysilane (98%), copper (II) chloride (≥98%) were from Alfa Aesar; ethanol (ACS, ISO, Reag. Ph Eur) was from EMSURE; hydrochloric acid (HCl, 37%) was purchased from Analar Normapur. CSA, CSC, CSD, CSE were purchased from Scientific Resources. All chemicals were used without further purification. Milli-Q water (>18.0 MΩ.cm) was purified with a Sartorius Arium 611 UV ultrapure water system.

Synthesis silver nanocubes. The preparation of silver nanocubes (AgNC) was followed the polyol method described is previous studied. 10 mL of CuCl2 at 8 mg/mL and PVP at 20 mg/mL were dissolved in to 1,5-pentanediol solution via vortexed and sonicated repeatedly. A 35 μL of CuCl2 solution was then added to AgNO3 solution (20 mg/mL) and vortexed and sonicated repeatedly till fully dissolved. A 100 mL round bottom flask was filled in 20 mL of 1,5-pentanediol, cleaned with aqua regia (3 HCl: 1 HNO3), and 10 minutes pre-heated of 1,5-pentanediol solution at 190 ºC. Then 250 μL PVP precursor was added dropwise to the round bottom flask every 30s while 500 μL AgNO3 precursor was added quickly every minute. This process was repeated until the color of reaction mixture turned reddish brown. For the subsequent growth of Ag octahedra, this solution was used without further treatment.

Purification of silver nanocubes. To purify the nanocubes for further self-assembly experiments, acetone was added to the AgNC solution and centrifuged to remove excess 1,5-pentanediol. The supernatant was then dispersed in ethanol to remove excess acetone. The resulting suspension was dispersed in 10 mL ethanol and subsequently diluted with 100 mL of aqueous PVP solution (0.2 g/L). The mixture was then vacuum filtered using PVDF filter membranes with pore sizes 5000, 650, 450 and 220 nm for some times on each pore size. UV-vis and SEM imaging were performed to analyse the edge length of AgNC. Edge length of 128±7 nm AgNC were measured and analysed using ImageJ software. The synthesized AgNC had an approximate concentration of 2 mg/mL.

Synthesis and purification of silver octahedra. The synthesis of AgNO proceeded from the nanocube solution in 1,5-pentanediol. For precursor preparation, 10 mL of CuCl2 at 8 mg/mL and PVP at 20 mg/mL were fully dissolved separately in 10 mL 1,5-pentanediol via

the vortexed and sonicated repeatedly till. A 40 μL of CuCl2 solution was then added to AgNO3 solution (40 mg/mL) and vortexed and sonicated repeatedly till fully dissolved. The round bottom flask containing the Ag NC solution in 1,5-pentanediol was heated to 190 °C for 10 minutes. A 250 μL PVP precursor was added dropwise to the round bottom flask every 30s while 500 μL AgNO3 precursor was added every minute. This process was continued for approximately an hour, and the reaction mixture became greyish brown.

To purify Ag NO, acetone was added to the AgNO solution and centrifuged at 8000 rpm for 10 minutes to remove excess 1,5-pentanediol and dispersed in 10 mL of ethanol to remove excess acetone. The resulting suspension was then redispersed in 10 mL of AR ethanol and then diluted with 100 mL of aqueous PVP solution (0.2 g/L). The mixture was then vacuumed filtered using PVDF filter membranes with pore sizes 5000 and 650 nm on each pore size for several times. UV-vis and SEM imaging were performed to analyse the length of AgNO. Edge length of 299±22 nm AgNO were measured and analysed using ImageJ software. The synthesized AgNO had an approximate concentration of 4 mg/mL.

Preparation of negatively-charged AgNC and AgNO. AgNC solution (0.1 mL, 0.18 mM) was added topup 1 mL of ethanol and discharge the supernatant after centrifuged. Then the 1.5 mL of solvent (50% IPA: 50% ethanol) were used to redispersed AgNC and left stirring at 500 rpm at 25 ºC. 50 μL of 11-mercaptoundecanoic acid IPA solution (0.1 mM) was added to the stirring solution of AgNC solution dropwise. The reaction mixture was then left to stir at room temperature for 4 hours. The mixture solution was then removed from stirring and centrifuged at 6500 rpm for 4.5 minutes. The resulting solution was undergo centrifuged step and removed the supernatant. The1.5 mL of IPA/Ehtnaol mixture (50% IPA: 50% ethanol) will add in and dispersed the AgNC, sonicated and centrifuged. The process was repeated twice, and the resulting product was stored in a nitrogen environment

to prevent oxidation. Zeta potential measurement of AgNC is about -24 mV to ensure particles were negatively charged. This ligand functionalization step was repeated for four separate AgNO solutions (100 µL, 0.11mM), using 11-mercaptoundecanoic acid IPA solution (0.1 mL, 10 mM).

Functionalization of Ag NC with 4-mercaptopyridine (4-MPY). 1 mL of ethanol was added to AgNC solution (0.1 mL, 0.18 mM) and the supernatant was discard after centrifuged. The AgNC were then redispersed in 1.5 mL of ethanol and left stirring at 500 rpm at 25 oC. A solution of 4-MPY (0.05 mL, 0.1 mM) in ethanol was added dropwise to the stirring solution of AgNC solution. The reaction mixture was then left to stir at room temperature for 4 hours. The reaction mixture was then removed from stirring and centrifuged at 6500 rpm for 4.5 minutes to remove the supernatant. The process was repeated once more, before repeating the same ligand reaction for a further 3 hours. The AgNC was then dispersed in 1.5 mL of ethanol, sonicated and centrifuged. The process was repeated twice, and the resulting product was stored in nitrogen box to prevent oxidation.

SERS measurements for CSs. Individual SERS experiments were first conducted for 4 pure CSs. 2 µL of CS solution (10^{-5} – 10^{-9} M) were mixed with the dried MPY-functionalized Ag NC (~0.2 mg/mL) at various pH value. The mixture was then drop-casted on the superhydrophobic chip and then allowed to dry under ambient conditions. Raman spectra were collected using a laser excitation wavelength of 532 nm, at 0.2 mW and 1s acquisition time.

Principal component analysis (PCA). In the PCA study, we input 24 untreated spectra each for 4-MPY-functionalized Ag NC (at pH5), 4-MPY-functionalized Ag NC-CSA, 4-

MPY-functionalized Ag NC-CSC, 4-MPY-functionalized Ag NC-CSD and 4-MPY-functionalized Ag NC-CSE, respectively into the software (total of 96 spectra). Standard normal variate correction, Savitzky-Golay derivative algorithm and mean center were applied to reduce spectral noise and eliminate interference from the background signals. During PCA analysis, the whole spectral range measured experimentally was selected, and two PCs were applied.

Partial least square analysis (PLS). PLS analysis was used to establish a standard calibration curve for the pure analytes, multiplexed detection of pure analytes. For pure analytes, PLS model was built up from 10^{-5}-10^{-9} M for every CS molecule. 24 spectra were input for each concentration measured, resulting in the use of 120 spectra. Baseline, standard normal variate correction and mean center were applied to reduce spectral noise and eliminate interference. During the analysis, the entire spectral range measured experimentally was selected, and a suitable number of loading vectors were employed to provide the minimum root-mean-square error for cross validation (RMSECV).

Confusion matrix. The SVM-DA function have been used to demonstrate the confusion matric. We apply a standardized set of pre-processing methods which include baseline correction using the automatic weighted least squares method, extended multiplicative scatter correction, normalization, and median centering. The cross-validated using venetian blinds, with 10 splits and a blind thickness of 1.

Characterization. SEM imaging was performed using a JEOL-JSM-7600F microscope at an accelerating voltage of 5 kV. Zeta potential measurements were conducted using ZETASIZER NANO with DTS1070 folded capillary cell. Thermal evaporation of Ag film

was performed using Syskey thermal evaporator (Taiwan). x-y SERS measurements were performed with Ramantouch microspectrometer (Nanophoton Inc, Osaka, Japan) at an excitation wavelength of 532 nm (power = 0.2 mW). A 20 x (N.A. 0.45) objective lens with 1 s accumulation time was used for data collection between 500 cm^{-1} to 1600 cm^{-1}. All SERS spectra were obtained by averaging at least 10 individual spectra per Raman image. ZIPTIPs (Merck Millipore) packed with a C18 column were used for sample pre-treatment. PCA, PLS analysis, and HCA were studied by solo (Eigenvector Research, Inc.).

Reference

1. Lopes, J. F.; Gaspar, E. M. S. M. *J. Chromatogr. A* **2008**, 1188, 42.
2. Armstrong, D. W.; DeMond, W. *J. Chromatogr. Sci.* **1984**, 22, 415.
3. Zachhuber, B.; Carrillo-Carrión, C.; Simonet Suau, B. M.; Lendl, B., *J. Raman Spectrosc.* **2012**, 43, 998-1002.
4. Burr, D. S.; Fatigante, W. L.; Lartey, J. A.; Jang, W.; Stelmack, A. R.; McClurg, N. W.; Standard, J. M.; Wieland, J. R.; Kim, J.-H.; Mulligan, C. C.; Driskell, J. D., *Anal. Chem.* 2020, 92, 6683.
5. Fleger, Y.; Mastai, Y.; Rosenbluh, M.; Dressler, D. H., SERS as a probe for adsorbate orientation on silver nanoclusters. *J. Raman Spectrosc.* **2009**, 40, 1577.
6. Phan-Quang, G. C.; Wee, E. H. Z.; Yang, F.; Lee, H. K.; YeePhang, I.; Feng, X.; RamónA.Alvarez-Puebla; Ling, X. Y. *Angew. Chem.* **2017**, 129, 5661.
7. Han, X.; Lee, H. K.; Lee, Y. H.; Ling, X. Y. *J. Phys. Chem. Lett.* **2017**, 8, 249.
8. Li, X.; Lee, H. K.; Phang, I. Y.; Lee, C. K.; Ling, X. Y. *Anal. Chem.* **2014**, 86, 10444.
9. Goodacre, R.; Graham, D.; Faulds, K., *Trends Anal. Chem.* **2018**, 102, 368.
10. Zhu, J.; Agyekum, A. A.; Kutsanedzie, F. Y. H.; Li, H.; Chen, Q.; Ouyang, Q.; Jiang, H. *LWT* **2018**, 97, 769.

11. Hong, K. Y.; de Albuquerque, C. D. L.; Poppi, R. J.; Brolo, A. G. *Anal. Chim. Acta* **2017**, 982, 155.
12. Theocharis, A. D.; Tsara, M. E.; Papageorgacopoulou, N.; Karavias, D. D.; Theocharis, D. A. *Biochim Biophys Acta. Mol. Basis. Dis. BBA-MOL BASIS DIS* **2000**, 1502, 206.
13. Theocharis, A. D.; Vynios, D. H.; Papageorgakopoulou, N.; Skandalis, S. S.; Theocharis, D. A. *Int. J. Biochem. Cell Biol.* **2003**, 35, 390.
14. Soares da Costa, D.; Reis, R. L.; Pashkuleva, I. *Annu. Rev. Biomed. Eng.* **2017**, 19, 26.
15. Monzavi-Karbassi, B.; Stanley, J. S.; Hennings, L.; Jousheghany, F.; Artaud, C.; Shaaf, S.; Kieber-Emmons, T. *Int. J. Cancer* **2007**, 120, 1191.
16. Suwiwat, S.; Ricciardelli, C.; Tammi, R.; Tammi, M.; Auvinen, P.; Kosma, V.-M.; LeBaron, R. G.; Raymond, W. A.; Tilley, W. D.; Horsfall, D. J. *Clin. Cancer Res.* **2004**, 10, 2498.
17. Wei Poh, Z.; Heng Gan, C.; Lee, E. J.; Guo, S.; Yip, G. W.; Lam, Y. *Sci. Rep.* **2015**, 5, 14355.
18. Kao, Y.-C.; Han, X.; Lee, Y. H.; Lee, H. K.; Phan-Quang, G. C.; Lay, C. L.; Sim, H. Y. F.; Phua, V. J. X.; Ng, L. S.; Ku, C. W.; Tan, T. C.; Phang, I. Y.; Tan, N. S.; Ling, X. Y., *ACS Nano* **2020**, 14, 2552.
19. Shen, Y.; Liang, L.; Zhang, S.; Huang, D.; Zhang, J.; Xu, S.; Liang, C.; Xu, W. *Nanoscale* **2018**, 10, 1630.
20. Wang, Y.; Song, W.; Ruan, W.; Yang, J.; Zhao, B.; Lombardi, J. R., *J. Phys. Chem. C* **2009**, 113, 8069.
21. Yu, H.-Z.; Xia, N.; Liu, Z.-F. *Anal. Chem.* **1999**, 71, 1358.
22. Wang, H. M.; Loganathan, D.; Linhardt, R. J. *Biochem. J.* **1991**, 278, 695.
23. Patel, I. S.; Premasiri, W. R.; Moir, D. T.; Ziegler, L. D. *J. Raman Spectrosc.* **2008**, 39, 1672.

24. Shin, H.; Jeong, H.; Park, J.; Hong, S.; Choi, Y. *ACS Sens.* **2018**, 3, 2643.

25. Profant, V.; Johannessen, C.; Blanch, E. W.; Bouř, P.; Baumruk, V. *Phys. Chem. Chem. Phys.* **2019**, 21, 7377.

6: Conclusion and Future Work

6.1 Summary

The continuous development and improvement of plasmonic platforms via nanoparticle assembly has dramatically enhanced the SERS signals and broaden the application fields especially for practical metabolomic applications. However, we observe two challenges and research gaps for biomolecule detection that are impeding the progress of SERS in real life application. Firstly, in terms of small molecule detection, due to the poor surface affinity and low Raman cross section of most small molecules, the low SERS sensitivity largely limits the applicability. Secondly, the multiplex detection and quantitative molecule detection from complex matrix is still challenging. In this thesis, we overcome these two challenges by designing SERS platforms with high SERS enhancements, and creating surface affinities for our target analyte. We showcase the ability for SERS multiplex detection and quantification by using chemometrics and machine learning algorithms such as PCA and PLS analysis.

In chapter 2, we demonstrate a two-part strategy at the oil/water interface to control the single building block morphology over the orientational ordering of supercrystals. The plastic crystals and uniform metacrystals are fabricated by the tailorable polymeric surface interactions and multi-faceted building blocks. The PVP chains exhibit long-range translational order but reduced orientational order driving the formation of plastic crystal. This is due to the limited molecular-level interactions between neighboring particles. On the contrary, molecular interaction between neighboring particles is due to the brush-like conformations of PEG chains, creating a translational and orientational order metacrystals. Our approach to form plastic crystals can be extended to polyhedral nanoparticles with non-identical crystal facets on the nanoparticle surfaces.

We further design a superhydrophobic SERS substrate in chapter 3, where we utilize two types of Ag nanoparticle for assembly as a proof-of-concept SERS detection platform for small molecule via capture-and confine strategy. We achieved high SERS enhancement by identifying two key factors. Firstly, the SPHB and mirror effect is crucial because it can physically concentrate the analyte in a small contact area effectively, enhancing SERS signals by 10^{12}-fold. Secondly, employing a probe molecule can provide a specific bonding to attract our target analytes to our particle surface which can further enhance SERS sensitivity. Notably, the use of PCA and PLS to extract key vibrational information from our SERS spectra enables differentiation of pregnane and THC. The multiplex analysis also can be achieved at 10^{-9} M which shows excellent detection ability of our strategy. Our confine-and-capture approach thus offers a breakthrough solution to achieve the detections for small molecules.

In chapter 4, we further extend our confine-and-capture strategy and develop a diagnostic kit toward real-life application for threatened miscarriage detection. In this chapter, we first conduct multiplex detection of pregnane and THC in artificial urine using ZipTip as pretreatment, after our platform has been proved to successfully facilitate pregnane and THC close to particle surface for SERS analysis in chapter 3. The PLS analyses results show that molecular fingerprints across the entire spectral window can be converted into quantifiable SERS readouts and observed the minor changes in metabolite concentrations at 0.1 nM levels from artificial urine sample within 30 minutes. Furthermore, we performed a case-control study by quantifying pregnane/THC ratio in real urine samples from 40 patients who are presenting symptoms of threatened miscarriage. Our strategy can potentially be used for different kind of diseases analysis in many clinical settings and is especially useful for small volume samples such tears or sputum.

Lastly, in chapter 5, we further exploit the confine-and-capture strategy for different structural variants analysis. The multiple analytes and probe molecular states enables the formation of diversified molecular complexes with different configurations, thus intensifying the specific SERS fingerprints over varied analytes. Importantly, the combination of SERS and chemometric analysis demonstrate a clear discrimination of a series of chondroitin sulfate disaccharide with different sulfate substitution position. Such discrimination is rapid and accurate, and is greatly superior to conventional detection techniques. Thus, these results show that the purpose of each chapter is linked back to the aim and objective, whereby through strategic platform design and selection of different probes, we have overcome the challenges of using SERS in biomolecules detection.

6.2 Future work

In this thesis, we have demonstrated an efficient detection strategy to significantly boost the SERS performance and applicability via confine-and-capture for small molecule detection through the specific probe molecule. However, research efforts should be continued and maintained to further explore and drive the development of our SERS detection technique toward real life sensing applications such as on-site detection for clinic diagnosis.[1-3] While several probe molecules have been incorporated with various types of plasmonic platforms to achieve high sensitivity, many of these sensors are in their infancy stage and are still performed under controlled laboratory conditions. Therefore, we identify two directions of SERS substrate design which show promising potential and discuss possible future works.

Firstly, SERS detection for small molecules with low Raman scattering cross sections usually using direct or indirect using probe molecule. The vibrational fingerprints from the direct detection are usually insignificant and difficult in achieving low detection limit. On the contrary, the indirect detection method enables delivery of the analytes information

through the probe vibrational band changes and achieves detection of analytes with very low detection limit.[4-8] Even though we demonstrate the possibility of SERS as a detection technique for small and significant molecules, the unitary probe molecule is insufficient to provide a comprehensive and specific fingerprinting information from the targets, especially in a complex biofluid for multiplex detection.[6-8] This will result in non-clear discrimination between multiple analytes, especially for structural analogues, in complex biological context.

In this aspect, to achieve multiplex detection with high accuracy, we anticipate the incorporation of increased surface sensing probe molecules into our detection system which is able to perform a fully deconvolution of our biofluid.[9] One of the key challenges in this detection strategy is that current probe selection for SERS is limited to a few molecules only (MPBA, MPY, MBA etc.). To select suitable probe molecules, we must look into the biofluid to study the structure of our interest. For example, in chapter 3, MPBA-based SERS reporter have been comprehensively studied that phenylboronic acid molecule can form boronic easter bond with hydroxy group which shows highly sensitivity and selectivity. However, there are numerous hydroxy containing molecules presented in our urine sample which may also create interference and exhibit competition between each of molecule that may further affect the sensitivity and selectivity. In addition, using a single probe molecule only can provide the interactions with single analyte functional group which can merely describe partial profile of the analyte chemical structure. To achieve high SERS sensitivity and accuracy for the bioanalysis, we will explore various types of probe molecules for sample analyte to create multiple types of vibrational changes. Furthermore, principal component analysis (PCA), partial least squares discriminant analysis (PLSDA), and machine-learning models such as support vector regression (SVR), will be used to extract useful data from the massive multivariate data in a fast and accurate manner.[10-13] Moreover,

the chemometric analysis can aid the analysis once we include different types of probe molecules to construct a prediction model according to the purpose of each detection. We will construct a SERS superprofile by combination the SERS spectra horizontally, whereby it will include all spectral variations arising from each of analyte with individual probe for data analysis.[9] This method can provide us high dimensionality of input data which can allow us to achieve comprehensive study. This strategy allows us to leverage the useful vibrational information from the whole spectra, resulting in high selectivity and accuracy.

Another future direction to improve our detection system is the substrate design and fabrication. To achieve the real-life application, the fabrication cost and how robust our device is may affect the practical application. Silicon wafer or glass slides are usually used in lab for detection application due to the versatility and resistance to organic solvents. However, silicon wafer is difficult to handle owing to its brittleness and toxic substances are produced during the manufacturing which doesn't make it easy to use as a detection kit for real life application. In addition, the cost of silicon wafer is much higher than other materials which make it become unattractive for real-life application. On the other hand, plastic, polystyrene, or poly-methyl methacrylate (PMMA), are the materials that have been used for fabricating the detection kit, since they are inert, biocompatible and they can adapt mass manufacturing process.[14-16] In addition, by translating our detection technique onto plastic substrates, we can potentially integrate our sensor into a wearable device which can expand the opportunities for noninvasive monitoring of physiological status, the status of disease and pathogen detection etc.[17-19]

References

1. Gubala, V.; Harris, L. F.; Ricco, A. J.; Tan, M. X.; Williams, D. E. *Anal. Chem.* **2012**, 84,515.
2. Granger, J. H.; Schlotter, N. E.; Crawford, A. C.; Porter, M. D. *Chem. Soc. Rev.* **2016**, 45, 3882.
3. Xu, K.; Zhou, R.; Takei, K.; Hong, M. *Adv. Sci.* **2019**, 6, 1900925.
4. Cardinal, M. F.; Vander Ende, E.; Hackler, R. A.; McAnally, M. O.; Stair, P. C.; Schatz, G. C.; Van Duyne, R. P., *Chem. Soc. Rev.* **2017**, 46, 3903.
5. Fan, W.; Yang, S.; Zhang, Y.; Huang, B.; Gong, Z.; Wang, D.; Fan, M. *ACS Sens.* **2020**, 5, 3606.
6. Fabris, L. *ChemNanoMat* 2**016**, 2, 258.
7. Kneipp, J.; Kneipp, H.; Kneipp, K. *Chem. Soc. Rev.* **2008**, 37, 1060.
8. Harpster, M. H.; Zhang, H.; Sankara-Warrier, A. K.; Ray, B. H.; Ward, T. R.; Kollmar, J. P.; Carron, K. T.; Mecham, J. O.; Corcoran, R. C.; Wilson, W. C.; Johnson, P. A. *Biosens. Bioelectron.* **2009**, 25, 681.
9. Leong, Y. X.; Lee, Y. H.; Koh, C. S. L.; Phan-Quang, G. C.; Han, X.; Phang, I. Y.; Ling, X. Y. *Nano Lett.* **2021**, 21, 2649.
10. Shin, H.; Oh, S.; Hong, S.; Kang, M.; Kang, D.; Ji, Y.-g.; Choi, B. H.; Kang, K.-W.; Jeong, H.; Park, Y.; Hong, S.; Kim, H. K.; Choi, Y. *ACS Nano* **2020**, 14, 5444.
11. Leong, S. X.; Koh, L. K.; Koh, C. S. L.; Phan-Quang, G. C.; Lee, H. K.; Ling, X. Y. *ACS Appl. Mater. Interfaces* **2020**, 12, 33427.
12. Ho, C.-S.; Jean, N.; Hogan, C. A.; Blackmon, L.; Jeffrey, S. S.; Holodniy, M.; Banaei, N.; Saleh, A. A. E.; Ermon, S.; Dionne, J. *Nat. Commun.* **2019**, 10, 4927.
13. Lussier, F.; Missirlis, D.; Spatz, J. P.; Masson, J.-F. *ACS Nano* **2019**, 13, 1411.
14. Rajapandiyan, P.; Yang, J. *Anal. Chem.* **2012**, 84, 10282.

15. Zhong, L.-B.; Yin, J.; Zheng, Y.-M.; Liu, Q.; Cheng, X.-X.; Luo, F.-H. *Anal. Chem.* **2014**, 86, 6267.
16. Yi, Z.; Niu, G.; Luo, J.; Kang, X.; Yao, W.; Zhang, W.; Yi, Y.; Yi, Y.; Ye, X.; Duan, T.; Tang, Y. *Sci. Rep.* **2016**, 6, 32314.
17. K, J.; S, B.; Ganiga, M.; R, D.; S, A.; Cyriac, J.; George, B. K. *Anal. Methods* **2017**, 9, 4003.
18. Xin, W.; Yang, J.-M.; Li, C.; Goorsky, M. S.; Carlson, L.; De Rosa, I. M. *ACS Appl. Mater. Interfaces* **2017**, 9, 6254.
19. Robinson, A. M.; Zhao, L.; Shah Alam, M. Y.; Bhandari, P.; Harroun, S. G.; Dendukuri, D.; Blackburn, J.; Brosseau, C. L. *Analyst* **2015**, 140, 785.